# Flow characterization for in-stream energy sites

Maricarmen Guerra Paris

A dissertation
submitted in partial fulfillment of the
requirements for the degree of

Doctor of Philosophy

University of Washington

2018

Reading Committee:

Jim Thomson, Chair

Alex Horner-Devine

Levi Kilcher

Program Authorized to Offer Degree:
Civil and Environmental Engineering

University of Washington

## Abstract

Flow characterization for in-stream energy sites

Maricarmen Guerra Paris

Chair of the Supervisory Committee:
Associate Professor Jim Thomson
Civil and Environmental Engineering

A successful in-stream energy project requires an accurate description of the flow characteristics. Numerical models are commonly used to detect feasible locations for energy extraction, but such models have limitations in resolution and accuracy, thus field measurements are crucial for their calibration and validation. In combination with numerical models, high-resolution observations of flow velocities in both time and space are needed to specify the location of turbines, estimate turbine design loads, and to evaluate their interaction with the environment. Promising sites for in-stream energy extraction have strong currents (greater than 1 $ms^{-1}$), and field measurements in such conditions are challenging. Hence, most field measurements are sparse and of limited duration. Efficient measurement techniques that can accurately map turbulent flows in space for long periods of time are critical as the in-stream energy industry reaches a commercial stage. In this thesis, traditional and novel methods are applied to the characterization of turbulent flows at several locations already selected for in-stream energy extraction. In addition, a new technique is developed to capture the wake of a full-scale hydrokinetic turbine under steady state conditions.

First, new five-beam acoustic current Doppler profilers (ADCPs) are demonstrated to measure turbulence parameters through the water column at two locations within Puget Sound, WA. The low Doppler noise and high-sampling frequency of these new profilers allow for the observation of the turbulent inertial subrange (typically obscured in previous

generations of ADCPs), and the addition of the $5^{\text{th}}$ beam allows for a direct estimation of the Reynolds stresses from along-beam velocity fluctuations. These results are then used to assess a turbulent kinetic energy budget, in which depth profiles of the turbulent kinetic energy dissipation and production rates are compared.

Long-term measurements of tidal currents across Admiralty Inlet, WA, are performed using ADCPs mounted onboard ferries. This cost-effective method results in a new map of tidal currents harmonics across and through the depth of the inlet. Obtained results agree well with those from stationary measurements, significantly expanding the available data here. Applications to residual flows are explored.

Finally, a new method is developed for detailed flow field mapping prior to and during the operation of a full-scale hydrokinetic turbine. A drifting five-beam ADCP, the Nortek Signature 1000, is used to evaluate the spatial extent of the turbine's wake and its evolution in terms of mean flow velocities and turbulence parameters. These results are valuable for numerical modelers, turbine designers, and stakeholders, as they quantify the environmental effects of in-stream energy extraction under real conditions.

# TABLE OF CONTENTS

# LIST OF FIGURES

# LIST OF TABLES

# ACKNOWLEDGMENTS

First of all I would like to thank Jim Thomson, it's been an honor being his student and to have him as a mentor. I cannot be more grateful for his continuous guidance, trust, support, and patience. I also thank him for always encourage me to do great work and for always being enthusiastic and optimistic about it. I am tremendously fortunate and happy to have come to the University of Washington to work with him and our group.

Additionally, I would like to thank the members of my committee, Andrea Ogston, Alex Horner-Devine, Brian Polagye, and Levi Kilcher. Their advice and guidance through these years encouraged me to be a better student and greatly contributed to the success of this thesis. I also thank all the help of Joe Talbert and Alex de Klerk. Since I first met them in Chile, I was impressed by their broad set of skills and knowledge, thank you for making my fieldwork feasible.

To the smart and fun UW-EFM group, a million thanks. Special thanks to my friend Raul; it has been very nice to share these years of hard work and studies with a fellow Chilean. A big thank you to my fantastic friends and office mates from Ben Hall 211, Maddie, Roxanne, Seth, and Mike, thank you for all the great conversations, laughs, and hugs.

An infinite thank you to my wonderful husband Francisco, who joined me without hesitation in this PhD journey. His love, encouragement, cheerfulness, hard work, and good cooking got me here. I could not have asked for a better partner and friend, and I hope we can go on many more adventures like this one again. I deeply thank my family back in Chile, for believing in me, for always having my back, and for always helping me to achieve my dreams and goals.

I also want to thank all my friends and family here in Seattle, specially those from Chile and Mexico. We have had such a great time together, filled with laughs and unforgettable memories. I particularly thank my dears friends Maria Vignau, Camila Tobar, and Daniela Diaz, for inspiring me in many ways. Their friendships have been very enriching, and one of the best things about my pass through graduate school. A big thank you to John Carter and Anna Racksany, who encourage us to come to Seattle and have always welcomed us in their home. I must also thank all my friends who have supported me from afar, and I thank even more to those who where lucky enough to visited us here in Seattle.

I must also thank my sponsor Fulbright. Through them I travelled around the US, and met extraordinary people from all over the world. I am also grateful for the funding provided by the Conicyt Becas Chile doctorate program. Finally, I would like to thank the support and funding provided by the Ocean Renewable Power Company (ORPC), the village of Igiugig in Alaska, the Naval Facilities Engineering Command (NAVFAC), and the US Department of Energy.

# DEDICATION

to Fran and my family, for their endless support

# Chapter 1

# INTRODUCTION

## *1.1 Motivation*

In-stream energy refers to the kinetic energy available in natural flows such as rivers and tidal channels. Favorable sites for in-stream energy extraction usually present fast water velocities above 1 $ms^{-1}$. As the need to exploit renewable sources of energy grows around the globe, and the development of hydrokinetic turbines for extracting this energy reaches a commercial stage, it is essential for in-stream energy projects to have detailed information about the hydrodynamics of these natural systems.

Detailed flow field characterization across a wide range of time and spatial scales is necessary for resource assessment, to define the best sites to deploy the turbines (Lewis et al., 2015), and to adequately design and evaluate the performance of hydrokinetic turbines (Blackmore et al., 2016; Chamorro et al., 2013a; Hill et al., 2014; Cavagnaro, 2014). In addition, responsible development of in-stream energy requires understanding and evaluation of the potential environmental impacts caused by both energy extraction and the underwater presence of turbines (Cada et al., 2007; Boehlert and Gill, 2010; Polagye et al., 2011).

In my home country of Chile, the state has set as a goal to produce 70% of its electricity from renewable sources by 2050 (Ministerio de Energía de Chile, 2015). In this context, in-stream energy poses an attractive source of renewable energy. However, most of the favorable areas remain practically not surveyed (especially tidal channels in Patagonia), probably due to their remote location. Efficient and cost-effective field measurement methods are critical for the development of the in-stream energy industry.

Although traditional methods exist for in-stream energy resource characterization, there is a continuing need for developing and testing new methodologies that evaluate mean flow

and turbulence characteristics at high-resolutions in both time and space. Existing instruments are accurate, but their continuous use and/or repeated deployment to map mean flow currents and turbulence over large areas can become financially prohibitive for both resource characterization and environmental monitoring once turbines are installed and operational.

In this thesis, besides using traditional instruments and platforms for characterizing energetic flows, new instruments and techniques are tested to accurately obtain these measurements. Furthermore, new field measurement methods are applied to the study of full-scale turbine wakes, providing new insights about the hydrodynamic impacts of in-stream energy extraction in a riverine setting.

The overall objective of this thesis is to characterize turbulent flows and their interaction with hydrokinetic turbines in time and space. The specific objectives are:

a. Test and develop data analysis techniques to measure turbulent flows using 5-Beam Acoustic Doppler Current Profilers

b. Efficiently provide large-scale characterization of tidal currents from vessel mounted instruments

c. Understand and quantify flow modifications in the presence of a full-scale hydrokinetic turbine

d. Advance the knowledge about the hydrodynamics of highly-energetic flows

### *1.2 In-stream Energy*

Moving bodies of water, such as rivers and the ocean, carry kinetic energy that can be harnessed for electricity production. With analogy to wind energy, water currents can be used to rotate relatively small scale underwater turbines, converting the available kinetic energy into electricity. There is no need for a large head (elevation difference) or impounded water as in conventional hydropower (Fraenkel, 2002; Yuce and Muratoglu, 2015; Segura

et al., 2018). The available (not necessarily extractable) kinetic energy flux is typically quantified by the power density, which depends on the water density $\rho$ and water velocity $\mathbf{u}$ such that:

$$P = \frac{1}{2}\rho \mathbf{u}^3 \tag{1.1}$$

The power relation with the cubed velocity reinforces the idea that detailed information about the currents is needed for resource assessment, because a small increase in velocity leads to a large increase in available power. The power available for extraction will also depend on the physical characteristics of the natural system (such as cross-section shape and bottom friction), on how the currents change in time and in space, and on how the turbines are distributed within the channel. For the specific case of a tidal channel, Garrett and Cummins (2005) found the extractable power to be less than the average kinetic energy flux.

In the open ocean, currents are small ($\mathcal{O}(0.1)$ ms$^{-1}$). Closer to the coast, tides interact with the local bathymetry and this can result in much stronger currents. In areas with spatial variability in tidal elevation and where the flows are constricted, tidal currents increase to be $\mathcal{O}(1)$ ms$^{-1}$ (Garrett and Cummins, 2005). These tidal currents are accurately predictable in time, because tidal forcing depend on the periodic motion of the earth, moon, and sun, and their gravitational pull over the ocean. Currents in large rivers are of the same order of magnitude as strong tidal currents. Hydrologic models predict discharge with reasonable accuracy, which can be used in combination specific local hydraulic models to predict flow velocities.

Total power available from rivers and tidal currents in the continental United States are available through the National Renewable Energy Laboratory (NREL) Marine and Hydrokinetic Energy Atlas. The total in-stream power available within the continental US rivers is estimated to be 1,381 TWh per year. The actual recoverable amount for electricity production is estimated to be about one-tenth that total at 119.9 TWh per year (EPRI, 2012). For tidal currents, it is reported that the maximum power available for extraction within the continental US is 438 TWh per year (Haas et al., 2011). This value corresponds to the

maximum extractable power at the maximum flow rates within tidal channels.

The power output from an hydrokinetic turbine of swept area $A$ is defined as:

$$P_T = \frac{1}{2}\rho\eta A\mathbf{u}^3 \tag{1.2}$$

where $\eta$ represents the total efficiency of the turbine system. The theoretical maximum efficiency that a turbine might reach is found from a simple actuator disk model (Burton et al., 2001). This model applies mass, momentum, and energy balances to a non-rotating porous actuator disk in an unconfined flow. The turbine maximum efficiency in an unconfined flow, know as Betz's Limit, is found to be $\frac{16}{27}$ (59.3 %) (Burton et al., 2001). However, in confined flows, such as a river or a tidal channel, this limit is found to be substantially exceeded (Garrett and Cummins, 2007). The theoretical maximum efficiency of a turbine in an unconfined flow is found to increase as the turbine's blockage ratio (defined as the ratio between the turbine cross-sectional area and the channel cross-sectional area) increases (Garrett and Cummins, 2007).

Once the turbines are underwater and extracting power, they interact with their surrounding flow creating a wake, which is typically characterized by slower velocities (less energy) and higher turbulence. The characteristic wake extension and recovery is key in designing turbine arrays and to evaluate the environmental effects of energy extraction. The wake extension is related to the blockage ratio. High-blockage ratios will result in persistent turbine wakes, with less opportunities for the wake to recover due to the proximity of the turbines to the channel boundaries (Garrett and Cummins, 2007).

Full-scale hydrokinetic turbines are currently designed to perform with currents between $\sim$0.5 ms$^{-1}$ and $\sim$2.5 ms$^{-1}$, and are rated for outputs between $\sim$25 kW and $\sim$1 MW (Lewis et al., 2015; Yuce and Muratoglu, 2015). Some technologies have reached a pre-commercial stage, and are (or have been) deployed in natural turbulent conditions supplying energy to local electricity grids. SeaGen turbine was the first full-scale tidal turbine, it was deployed in Strangford Lough and grid connected between 2008 and 2016 (Tethys, 2016). Through the MeyGen Tidal Project, three Andritz Hammerfest Hydro turbines and one Atlantis

Resource Turbine, rated at 1.5 MW each, were deployed and grid connected at the northern coast of Scotland in March 2018. This unique array has generated 8GWh to date and exported 1.4GWh to the local electricity grid (Atlantis Energy, 2018). Multiple other systems have been tested in the European Marine Energy Centre (EMEC) in the United Kingdom. Scotrenewables tidal turbine, installed at EMEC, has generated more than 2 GWh since 2017 (Scotrenewables, 2018). OpenHydro turbines have been successfully deployed at EMEC (first in 2006), at Bay of Fundy in Canada (in 2010, 2016, and 2018), and in the north of France (in 2016), however OpenHydro was unexpectedly terminated by its head corporation Naval Energies in July 2018 (OpenHydro, 2018). In the United States, Ocean Renewable Power Company (ORPC) installed and connected to the local grid its RivGen turbine model in the Kvichak river (Alaska) during the 2014 and 2015 summers (Ocean Renewable Power Company, 2015), and Verdant Power installed six hydrokinetic turbines in the East River, NY in 2006 (Verdant Power, 2012).

### *1.3 Study Sites*

Four study sites are included in this investigation. All sites are well-suited for in-stream energy extraction, sustaining strong water currents at depths adequate for the installation of hydrokinetic turbines. Figure 1.1 shows the location of each sites and a brief description is presented below.

a. Admiralty Inlet, located in the northern part of Puget Sound, WA, USA (48.14°N, 122.71° W), is $\sim$ 6 km wide and $\sim$ 150 m deep at mid channel. Previously observed maximum velocities at Admiralty Inlet are greater than 3 m/s (Polagye and Thomson, 2013; Thomson et al., 2012). A tidal energy demonstration project was a proposed by Snohomish County Public Utility District at the north-east part of Admiralty Inlet, which considered the installation of two OpenHydro turbines. Although all the necessary permits were obtained, the utility district decided to discontinue the project in 2014 due to funding challenges.

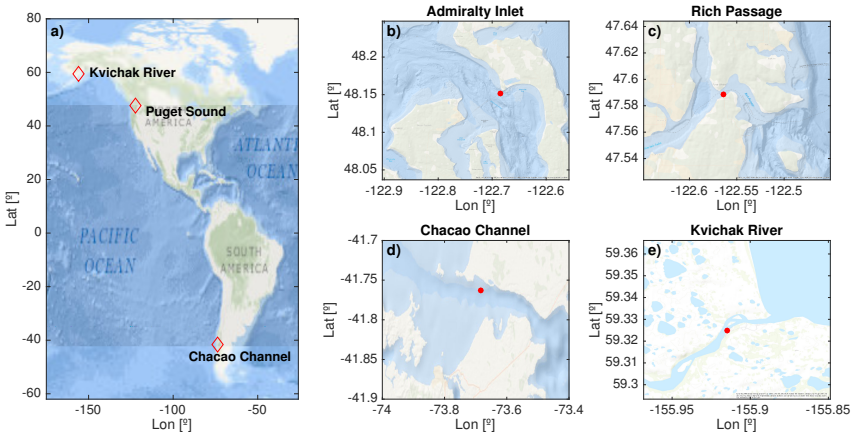


Figure 1.1: Study sites: a) Location within the Americas, b) Admiralty Inlet, c) Rich Passage, d) Chacao Channel, e) Kvichak River. Red dots show measurements locations

b. Rich Passage, located south of Bainbridge island in Puget Sound, WA, USA (47.59° N, 122.56° W). At the study area, at its west end, the channel is $\sim$ 28 m deep and $\sim$ 550 m wide. Maximum observed currents in Rich Passage are approximately 2.5 m/s. Despite the strong tidal energy resource, no tidal energy developments are planned for this channel.

c. Chacao Channel is located in the north Chilean Patagonia fjord region (S 41°; W 73°). The channel is approximately 40 km long and about 2.5 km wide in its narrowest part. Previously observed tidal currents in Chacao Channel are of the order of 4 m/s during spring tide (Cáceres et al., 2003; Aiken, 2008). This site was selected as the best site for extracting tidal energy in Chile by an International Development Bank study presented in Cruz et al. (2009). This study marked the beginning for tidal energy resource assessment in Chile, however all in-stream developments are at the research level and no turbine deployments are planned there.

d. The Kvichak River (N 59.32°; W 155.91°) flows southwest from the Iliamna Lake to Bristol Bay in southwest Alaska. At the study site, just downstream of the village of

Igiugig, the river is approximately 5 m deep and 150 m wide. The flow is a maximum of $\sim$ 2.5 m/s in the center of the river. The village of Igiugig, isolated from any large electricity grids, seeks to developed locally generated renewable sources of energy. In this context, ORPC deployed and connected to the local electricity grid its RivGen turbine during the summers of 2014 and 2015, and future deployments are planned for 2019.

## *1.4 Turbulent flows*

At a single location in space, the full velocity signal $\mathbf{u}(x, y, z)$ can be decomposed as:

$$\mathbf{u}(x, y, z) = \overline{u} + \tilde{u} + u' \tag{1.3}$$

where $\overline{\mathbf{u}}$ represents the mean flow velocity and is usually deterministic. Wave orbital motions are represented by $\tilde{u}$, and $u'$ refers to the turbulent fluctuations of the mean velocity. The turbulent fluctuations spann from large-scale two-dimensional eddies to small-scale isotropic eddies. At these four study sites, waves are typically small ($H_s < 1$ m), and wave orbital velocities decrease rapidly with depth, being negligible at the depths where in-stream turbines would be located. Thus, wave orbital velocities are neglected for the rest of the thesis.

### *1.4.1 Mean Flow*

The deterministic component of the total flow velocity, $\overline{u}$, refers to the mean flow velocity at a single location in space under statistically stationary conditions. In rivers, the deterministic mean flow velocity will be equivalent to the flow velocity under steady-state conditions. Seasonal variations in the mean flow velocity occur during the hydrological year, due to changes in discharge. In tidal channels, when the flow is continuously changing in time due to tides, statistically stationary conditions last only between 5 to 10 minutes (McCaffrey et al., 2015).

In tidal channels, a portion of the deterministic currents is modulated in time by tidal harmonics. The mean flow velocity is assumed to be equivalent to the superposition of tidal

harmonic constituents, whose frequencies are known and depend on the periodic motions of the earth, moon, and sun. Then, the mean flow velocity can be approximated as:

$$\overline{u} = u_0 + \sum_{i}^{N} u_i cos(\alpha_i + \omega t) \tag{1.4}$$

where $\overline{u}$ is the along-channel mean flow velocity at time $t$, $u_0$ is the underlying mean flow velocity, and $u_i$, $\alpha$, and $\omega$ are the amplitude, phase, and frequency of each tidal constituent considered in the analysis, respectively. Amplitudes and phase values are site specific, and field measurements or hydrodynamic numerical models are needed to determine them. Tidal harmonic analysis allows to predict mean flow velocities in tidal channels for long periods of time. In places where the tides present a semi-diurnal regime (two ebb and two flood tides each lunar day), the most energetic component is the $M_2$ tidal harmonic (also known as principal semi-diurnal), with a period of 12.42 hours. In some places, like Admiralty Inlet, the amplitude of this component has been estimated to be greater than 1.5 $ms^{-1}$ (Polagye and Thomson, 2013). It important to note that harmonic analysis cannot be used to predict sub-tidal flows nor turbulence, hence additional methods must be used to describe and predict these velocity components.

Sub-tidal flows also contribute to the deterministic mean currents, and are usually related to estuarine circulation or non-linear interactions of tidal currents with local bathymetry. In places like Admiralty Inlet, residual flows strong as 0.4 $ms^1$ have been observed, with important seasonal variations related to denser ocean water intrusions (Polagye and Thomson, 2013; Deppe et al., 2018). Residual flows up to 0.5 $ms^1$ have been observed in Chacao Channel, showing a spatial structure where inflow occurs in the shallower portion and outflow occurs in the deeper portion of an specific channel cross section with strong bathymetric gradients (Cáceres et al., 2003).

For detailed energy resource characterization, currents cannot be assumed uniform in space. Channel bathymetry and boundary layers influence the spatial distribution of flow velocities. Velocity shear, defined as the spatial gradient of mean flow velocity in all three cartesian components, leads to rapid changes in flow velocity within short distances (and

even greater changes in available power). At Admiralty Inlet, sharp horizontal gradients occur in less than 100 m distances (Palodichuk et al., 2013). In the Kvichak River strong lateral shear occurs at the cross section of the turbine location, with velocity increasing more than 0.5 $ms^{-1}$ in less than 25 m (for reference the turbine installed there is 12 m long).

Vertically, currents are affected by the bottom boundary layer, resulting in slower currents closer to the bottom. In unstratified turbulent flows, the mean velocity vertical shear is well represented by the law of the wall approximation:

$$\frac{\partial \overline{u}(z)}{\partial z} = \frac{u_*}{\kappa z} \tag{1.5}$$

where $z$ is the distance from the bottom, $u_*$ is the shear velocity, and $\kappa$ is the Von Kármán constant, equal to 0.41. The logarithmic vertical profile of mean velocity can be obtained by integrating equation 1.5 such that:

$$\overline{u}(z) = \frac{u_*}{\kappa z} \ln\left(\frac{z}{z_0}\right) \tag{1.6}$$

where $z_0$ represents the bottom roughness length.

### *1.4.2 Turbulence*

Turbulent flow motions vary within a wide range of scales depending on Reynolds number. These turbulent fluctuations, also known as turbulent eddies, are usually represented by their kinetic energy content, defined as turbulent kinetic energy (TKE) (Pope, 2001).

Within the in-stream energy community, the most common parameter used for describing turbulence is the turbulence intensity, $TI$, a ratio between the turbulent fluctuations, represented by their standard deviation $\sigma_u$, and the mean flow velocity, $\overline{u}$. This bulk parameter is typically used in models that evaluate turbine performance, however it does not provide specific information about turbulent eddies sizes or energetics that might be important for hydrokinetic turbines durability.

In a turbulent flow, the evolution of turbulent kinetic energy at a single location in time and space is described by the turbulent kinetic energy balance, which can be written as:

$$\frac{D}{Dt}(TKE) = \nabla T + P - \varepsilon \tag{1.7}$$

where $D/Dt$ represents the total rate of change of TKE, $\nabla T$ is the turbulent transport of TKE, $P$ represents the production of TKE, and $\varepsilon$ represents the dissipation of TKE.

The turbulent transport term, $\nabla T$, represents the spatial transport of turbulent kinetic energy due to turbulent pressure fluctuations, viscous diffusion, and turbulent stresses. These terms act to redistribute TKE within a control volume, rather than generate and/or dissipate TKE (Kundu et al., 2008).

In fresh water environments and in energetic tidal channels, which are usually well-mixed, TKE is primarily produced by the mean flow shear, and TKE changes due to stratification can be neglected. The Reynolds stresses combined with the mean flow shear define the TKE production as:

$$P = -\overline{u_j u_i}\frac{\delta \overline{u}_j}{\delta x_i} \tag{1.8}$$

where $\overline{u_j u_i}$ are the Reynolds stresses, and $i$ and $j$ represent the three cartesian directions. The estimation of total TKE production requires the estimation of all six components of the Reynolds stress tensor, and the mean flow shear in all three cartesian directions. If TKE is mainly produced at the bottom and horizontal shear is negligible, the TKE production is mainly produced by the vertical shear of the along-channel velocity $\frac{\delta \overline{u}_1}{\delta x_3}$, and can be approximated by:

$$P \approx -\overline{u_1 u_3}\frac{\delta \overline{u}_1}{\delta x_3} \tag{1.9}$$

Applying a drag law and the law of the wall for fully developed turbulent flows, the approximate TKE production from equation 1.9 can be estimated as:

$$P(z) = \frac{u_*^3}{\kappa z} \tag{1.10}$$

where $z$ is the distance from the bottom, $u_*$ is the shear velocity, and $\kappa$ is the Von Kármán constant, equal to 0.41.

The turbulent kinetic energy dissipation rate $\varepsilon$, a sink term in the TKE balance, represents how TKE is transformed into internal energy (Pope, 2001), and it is defined by:

$$\varepsilon = 2\nu\overline{s_{ij}s_{ij}} \tag{1.11}$$

where $\nu$ is the kinematic viscosity and $s_{ij} = 1/2\,(\delta u_i/\delta x_j + \delta u_j/\delta x_i)$ is the fluctuating rate of strain.

To estimate the TKE dissipation rate from its definition, the turbulent rates of strain must be resolved. These gradients of turbulent velocity fluctuations are practically impossible to measure in the field or to resolve by numerical models. However, indirect methods derived from Kolmogorov's hypothesis can be used to estimate TKE dissipation rates.

*Turbulence Energy Cascade*

The energy cascade theory (Richardson, 1922; Kolmogorov, 1941) states that the turbulent kinetic energy is transferred from larger energy containing eddies to ever smaller eddies until it is dissipated to heat and sound by viscosity. Three regions are distinguished in the energy cascade from larger to smaller turbulent eddies. The large anisotropic energy containing eddies compose the first region. These eddies primarily get their energy from TKE shear production. In the second region, turbulent eddies become isotropic and the transfer of energy to smaller scales occurs. According to Kolmogorov (1941) hypotheses of turbulence, in this region, also known as the inertial subrange, the energy transfer depends exclusively on the TKE dissipation rate. In the third region, known as dissipation range, turbulent motions remain isotropic and the transfer of energy continues, however viscous effects dominate and the smallest sized eddies are ultimately dissipated to heat and sound (Pope, 2001).

The energy cascade is well illustrated by the turbulent kinetic energy spectra, which represents the distribution of TKE among eddies of different sizes, and by the structure

function of turbulence, which describes the covariance between turbulent fluctuations at two different points in space separated by a distance $r$ (which is a proxy for eddy size).

The same energy cascade regions can be observed in the TKE spectra. From Kolmogorov's hypotheses is derived that in the inertial subrange the TKE spectra scales with the TKE dissipation rate $\varepsilon$ and with the eddy size, represented by their spatial wavenumber $k$ ($k = 2\pi/l$, where $l$ is the eddy length scale), such that:

$$S(k) = C\varepsilon^{2/3}k^{-5/3} \tag{1.12}$$

where $S(k)$ is the wavenumber TKE spectra and $C$ is a constant. This relation is known as the Kolmogorov $-5/3$ spectra.

The second-order structure function is defined as the covariance between turbulent fluctuations at two different points in space by:

$$D_i(z,r) = \overline{(u_i(z+r) - u_i(z))^2} \tag{1.13}$$

where $z$ is the location in space, $r$ is the distance between the two points, and $u_i$ corresponds to each velocity fluctuation; the over line denotes a time average. Similarly, to the spectrum, in the inertial subrange, the second-order structure function is related to the distance $r$ and to the dissipation rate $\varepsilon$ by:

$$D_i(z,r) = C_v^2\varepsilon^{2/3}r^{2/3} \tag{1.14}$$

where $C_v^2$ is a constant.

The TKE dissipation rate can be estimated from TKE spectra and turbulence structure functions when turbulent flows are measured at sufficiently high sample frequencies and enough spatial resolution, such that the inertial subrange can be resolved from the observations. Note that frequency spectra can be related to wavenumber spectra in a simple change of variables $f = \bar{u}k$. This applies Taylor's frozen field hypothesis, in which turbulence does not evolve on the short time scales with which mean advection occurs.

### *1.5 Flow measurement techniques*

The most common instruments for measuring flow velocities are based on acoustics. These instruments use the Doppler effect of a sound pulse reflected back from particles suspended through the water column to estimate velocity. Acoustic Doppler current profilers (ADCPs) are commonly used to measure fluid velocities at set distance intervals using three or four diverging acoustic beams. Velocities are measured along profiles in the acoustic beam direction. Using the beam configuration geometry and the instrument's orientation, along-beam velocities can be transformed into cartesian and/or east, north, up (ENU) velocities. The raw measurements are typically burst-averaged in time in order to reduce the Doppler noise inherent to the measurement method.

ADCPs can be fixed to a stationary platform or mounted onboard a moving platform. Fixed ADCPs are usually bottom-mounted or moored, and provide time-series of velocities along depth profiles at a single location. In tidal channels, at least 35 days of measurements are needed to capture the main tidal constituents, and longer (or repeated) deployments are needed for capturing seasonal sub-tidal flows and stronger currents (Yang and Copping, 2017). ADCPs mounted on board buoys or vessels are used to capture the spatial variability of the flow. In tidal channels and rivers, the station keeping technique from Palodichuk et al. (2013) has been proven effective for capturing velocity shear and currents spatial variability.

Turbulence characterization in rivers and tidal channels requires sampling at high frequency in order to resolve the three dimensional velocity fluctuations among a wide range of time and length scales. In addition, turbulence measurements must be sufficiently plentiful to obtain robust statistics (Burchard et al., 2008).

Most ADCPs are not well-suited for turbulence measurements, as the inherent Doppler noise typically obscures the expected turbulent cascade through the inertial subrange (Richard et al., 2013). However, if the raw along-beam velocities are retained and the noise variance is explicitly removed, many turbulence parameters, such as turbulence intensity, Reynolds stresses, and turbulent kinetic energy dissipation rates, can be estimated from ADCP mea-

surements (Lu and Lueck, 1999; Stacey et al., 1999; Wiles et al., 2006; Thomson et al., 2012).

Acoustic Doppler velocimeters (ADVs) measure three dimensional velocities at a single point in space. These instruments are distinct from ADCPs in that they are bistatic (i.e., separate transducers for send and receive) and coherent. ADVs have high temporal precision and lower Doppler noise, and thus ADVs often are a preferred choice for turbulence measurements. ADVs have been used to measure turbulence at tidal energy sites using moorings that target the hub-height depths of turbines. The use of compliant moorings introduces motions that contaminate the turbulence signals. These motions must be removed from the data before attempting any calculations of turbulence parameters. Harding et al. (2017) and Kilcher et al. (2017) provide suitable motion characterization and motion correction techniques for moored ADV turbulence measurements. The corrections effectively remove the motion contamination, yielding a clean turbulent kinetic energy spectra and cross-spectra, allowing estimations of TKE dissipation rates and Reynolds stresses for different mean flow conditions at a single point in the water column.

New broadband ADCPs with the ability to measure flow velocity at higher frequencies and with lower noise levels (similar to ADVs noise levels) are now available. These instruments will improve and facilitate routine turbulence measurements. Moreover, the inclusion of a fifth beam allows for a true measurement of vertical velocities and the estimation of five (out of six) Reynolds stresses, total turbulent kinetic energy (TKE), and anisotropy directly from the along-beam velocities (Lu and Lueck, 1999; Dewey and Stringer, 2007).

### *1.6 Thesis Outline*

This thesis presents comprehensive flow characterizations from field measurements at highly energetic locations. Two different environments are studied, tidal channels and rivers. Traditional and novel methodologies are used to measure and describe flow characteristics at each site for pre- and post-turbine installation conditions. Figure 1.2 shows an schematic of the wide range of instruments and measurement techniques used through this work, which

will be described in the chapters to follow.

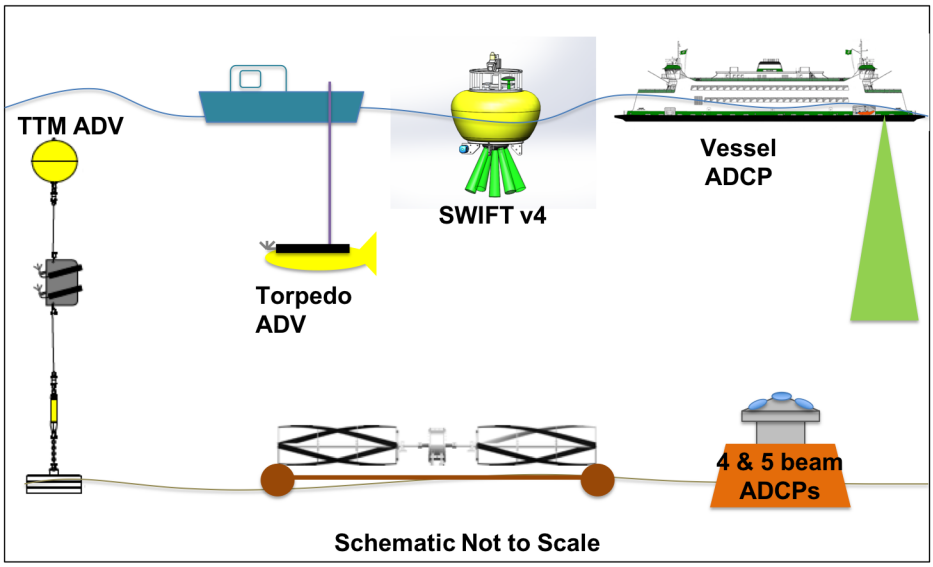


Figure 1.2: Instruments and platforms used in this thesis for flow characterization at in-stream energy sites. Schematic is not to scale.

In Chapter 2 traditional methods are applied for tidal energy resource characterization at Chacao Channel, including field measurements of tidal elevation, tidal currents in time and in space, and turbulence. Field data were previously used to calibrate and validate a FVCOM hydrodynamic numerical model of the entire channel, and results from this model are used here for tidal energy resource assessment. This chapter is reproduced from

**Guerra, M., Cienfuegos, R., Thomson, J., and Suarez, L.** (2017). *Tidal energy resource characterization in Chacao Channel, Chile.* International journal of marine energy, 20, 1-16.

Chapter 3 presents turbulence measurements from two new five-beam acoustic Doppler current profilers at Admiralty Inlet and Rich Passage. The quality of the data is tested by analyzing the turbulent kinetic energy frequency spectra, the turbulence spatial structure function, the shear in the velocity profiles, and the covariance Reynolds stresses. These

combined results are then used to evaluated the turbulent kinetic energy balance through the water column at these two locations. This chapter is reproduced from

**Guerra, M., and Thomson, J.** (2017). *Turbulence measurements from five-beam acoustic Doppler current profilers.* Journal of Atmospheric and Oceanic Technology, 34(6), 1267-1284.

Chapter 4 presents a cost-effective method for measuring tidal currents using ADCPs mounted onboard ferries. Data collected through Admiralty inlet are analyzed to capture tidal current harmonic components. Preliminary estimates of residual currents through the inlet are also presented, which are relevant to water quality within the Puget Sound. This chapter will be submitted for publication in the future.

Chapter 5 explores the hydrodynamic effects caused by a full-scale hydrokinetic turbine deployed and connected to the grid in the Kvichak river. Field observations are used to produce a three-dimensional data set of velocities in the vicinity of the turbine before and after turbine deployment. The turbine wake is well captured by the measurements and it is analyzed in terms of velocity and turbulence parameters for non-operational and operational turbine conditions. This chapter is under review at Renewable Energy journal as

**Guerra, M., and Thomson, J.** *Wake measurements from a hydrokinetic river turbine*, in review.

Finally, Chapter 6 presents a summary of the main findings of this thesis, including future directions for in-stream energy resource characterization and the evaluation of the hydrodynamic impacts of energy extraction.

# Chapter 2

# TIDAL ENERGY RESOURCE CHARACTERIZATION IN CHACAO CHANNEL, CHILE

## *2.1 Introduction*

Historically, electricity in Chile has been mainly generated from hydroelectric dams (nearly 80% in the 1980s) (Ministerio de Energía de Chile, 2015). In recent years, hydroelectricity generation has reduced to 43% (on average from 2010 to 2014). The variability of hydrological conditions has prompted the search for reliable forms of electricity generation, and thus electricity at present is mostly generated from fossil fuels (52%, natural gas and coal) (Ministerio de Energía de Chile, 2015; Raineri, 2006). Due to the shift in the Chilean energy matrix, the Chilean government has set as goal to produce 60% of its electricity from renewables by 2035, and 70% by 2050 (Ministerio de Energía de Chile, 2015). (Note that these renewable percentages include hydroelectricity.) In this context, tidal energy is an enticing source of renewable energy for Chile, as the chilean coast has been recognized to be among the most energetic in South America (Cruz et al., 2009). Among the priority sites along the Chilean coast, Chacao Channel (S 41°; W 74°) has been previously recognized as the most suitable site for tidal energy extraction considering its available resource and its proximity to the electrical grid (Cruz et al., 2009). However, this statement is based on global model predictions over coarse bathymetric information. A detailed resource characterization, in time and in space, is necessary for selecting interesting areas for tidal energy extraction within the channel, for better power extraction estimations, and for appropriate turbine design (Lewis et al., 2015; Polagye and Thomson, 2013).

According to guidelines from the European Marine Energy Center (EMEC), the tidal energy resource characterization at a specific tidal channel should include long-term mea-

surements of tidal currents (from which tidal harmonics can be calculated) together with hydrodynamic numerical models that expand the information from the field measurements (Legrand, 2009). Field measurements typically use Acoustic Doppler Current Profilers (ADCPs), which provide time series of the three components of velocities at different depths in the water column. Up-looking bottom-mounted ADCPs are used to analyze the temporal variability in the tidal currents at a single location (Polagye and Thomson, 2013; Goundar and Ahmed, 2014; Carpman and Thomas, 2016; Thiébaut and Sentchev, 2016), while down-looking ship-mounted ADCPs are used to analyze tidal current variation in space (Palodichuk et al., 2013; Carpman and Thomas, 2016).

A wide range of different hydrodynamic numerical models are used to characterize the tidal energy resource (Yang et al., 2013; Tang et al., 2014). Simple analytic models, such as Garrett and Cummins (2008) (Garrett and Cummins, 2008), are also used in resource assessment. Three-dimensional (3-D) models are currently the choice for tidal energy resource assessment (Yang et al., 2013), since they provide information about the vertical structure of velocity, and hence a better estimation of localized power. In Lewis et al. (2015), ROMS (Regional Ocean Modeling System) is used to evaluate the tidal energy resource in the Irish Sea; a sensitivity analysis on grid resolution indicates that a resolution of less than 500 m is required for a regional-scale resource assessment (Lewis et al., 2015). Tang et al. (2014) evaluated the tidal energy potential along the New Jersey coast using the unstructured FVCOM model, with resolutions as fine as 10 m, and this allowed for a detailed representation of the New Jersey coastline. The most favorable sites were found in the mouths of bays, narrow channels, and headlands (Tang et al., 2014).

In addition to mean flow conditions (needed for power estimations), time and space characterization of ambient turbulence is also necessary for tidal energy resource characterization. At a single location in space, the full tidal current signal $\mathbf{u}(z)$ can be decomposed as:

$$\mathbf{u}(z) = \overline{\mathbf{u}} + \tilde{u} + u' \tag{2.1}$$

where $\overline{\mathbf{u}}$ represents the deterministic currents, including both harmonic and anharmonic

components. The deterministic currents are usually dominated by harmonic constituents associated with lunar and solar forcing, while anharmonic currents result from interaction with the local bathymetry (Thomson et al., 2012; Polagye and Thomson, 2013). Wave and wind induced currents, and residual flows, are represented by $\tilde{u}$ and are neglected within this Chaco Channel study. Finally, $u'$ refers to the turbulent fluctuations of the mean current, spanning from large-scale two-dimensional eddies to small-scale isotropic eddies (Thomson et al., 2012).

Turbulence has a significant impact in turbine performance and durability (Chamorro et al., 2013a; Blackmore et al., 2016; Pyakurel et al., 2017), as well as extension and recovery of the wake behind the turbine (Blackmore et al., 2014). Many turbulence parameters can be estimated from ADCP measurements, if variance due to noise is correctly removed from the raw data. However, Acoustic Doppler Velocimeters are the preferred instrument for turbulence measurements, as they record velocities at high-sampling frequencies with low noise, and thereby allow for the observation of a wide range of turbulence scales. Osalusi et al. (2009) characterize the turbulent structure, and turbulence evolution, at EMEC's tidal energy site using ADCPs measurements. Osalusi et al. (2009) estimate Reynold's stresses, and Turbulent Kinetic Energy (TKE) production and dissipation rates. Thomson et al. (2012) examine the ambient turbulence at two prospective tidal energy sites in Puget Sound, WA., using both ADCPs and ADVs. A set of turbulence statistics and turbulence estimation techniques are provided, which are useful to estimate turbine design loads (Thomson et al., 2012). The studied turbulence parameters include, among others, noise-corrected turbulence intensity, TKE frequency spectra, and the examination of an approximate TKE balance. However, the authors emphasize that turbulence measurements from ADCPs are limited by their higher Doppler noise (which needs to be removed), and by the bin sizes (which limit the observed turbulence length scales) (Thomson et al., 2012).

### *2.1.1 Site Description*

Chacao Channel is an energetic tidal channel located in the north of the Chilean Patagonia fjord region (S 41°; W 74°). The channel separates mainland Chile (to the north) and Chiloé Island (to the south). In the east-west direction, it connects the Chilean Inland Sea (CIS) to the Pacific Ocean, via the Gulf of Ancud. The channel is approximately 40 km long and about 2.5 km wide in its narrowest part. The map on Figure 2.1 shows the location of Chacao Channel within the Chilean Inland Sea region. The flow in Chacao Channel exhibits a cyclic behavior dominated by astronomical tidal currents, the $M_2$ semi-diurnal component being the most significant one (Cáceres et al., 2003). Previous investigations report the presence of high tidal amplitudes and currents, up to 6 m and 4 $ms^{-1}$, respectively, during spring tides (Cáceres et al., 2003; Aiken, 2008). The circulation in Chacao Channel is weakly influenced by river discharge, with typical salinities around 30 PSU (Cáceres et al., 2003).

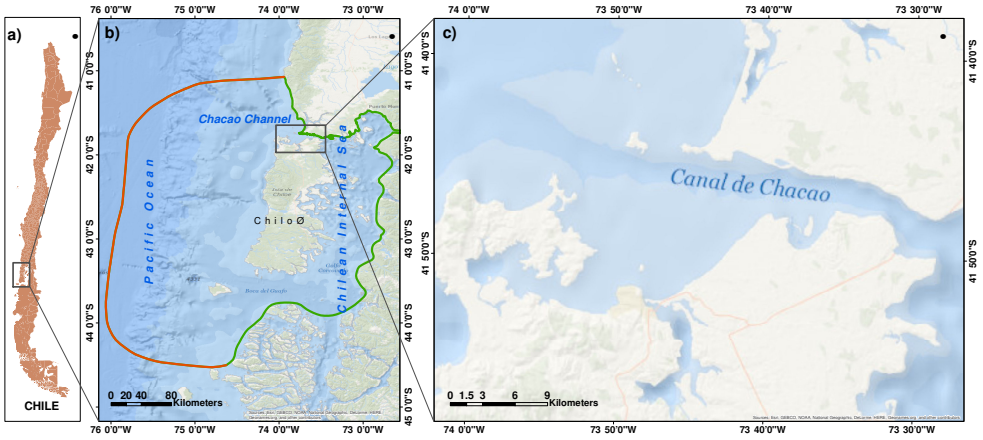


Figure 2.1: a) Chacao Channel location in the south of Chile, b) Northern portion of Chilean Internal Sea, FVCOM domain boundaries in green, and FVCOM forcing boundary in orange, and c) Chacao Channel.

Chacao Channel is the entrance to the Chilean Patagonia, an area characterized by pristine landscapes and fjord-like channels. This area is expected to receive high pressure from infrastructure and energy projects in the future (Pantoja et al., 2011). Chacao Channel

is regionally important for environmental, social and economic reasons. The channel is home to a great diversity of benthic organisms and mammals. It is, for example, one of the few sites where a blue whale has been sighted (Hucke-Gaete et al., 2004; Vernazzani et al., 2012). Chacao Channel has eight fishing villages, where more than 4,000 artisan fishermen work and more than 25,000 tons of fisheries resources are extracted every year (Castilla et al., 2012). Despite its importance to the Chilean society, the knowledge of Chacao Channel's hydrodynamics is limited. The previous published hydrodynamic investigations focused on Chacao Channel are the works of Cáceres et. al (2003) (Cáceres et al., 2003) and Aiken (2008) (Aiken, 2008). Both emphasized the energetic behavior of the channel and its complex hydrodynamics.

Cáceres et al. (2003) studied the across channel flow structure at the narrowest part, where a large pinnacle, known as Roca Remolinos, exists in the center of the cross section. They analyze the across channel velocity variations as the strong tidal flows interact with the pinnacle, and they present estimates for the terms of the across channel momentum balance equation. The main findings suggest nonlinear interactions between the flow and the bathymetry, which cause a strong lateral structure of residual flows, wherein there is an outflow in the deep channels and inflows on the shoals (Cáceres et al., 2003). The work of Aiken (2008) studies the propagation of tidal waves from the Pacific Ocean into the Chilean Inland Sea (CIS) region (shown in Figure 2.1), with a focus on the behavior of tidal constituents within the CIS. Numerical investigations of barotropic tides are conducted using a ROMS model of the entire CIS (Aiken, 2008). Aiken showed tidal amplification within the northern part of the CIS (located southeast of Chacao Channel) due to the resonance of tidal waves as they interact with the basin geometry. This resonance is thought to be responsible for the large range of tidal elevations at the east end of Chacao Channel, which in turn drives the strong tidal currents (Aiken, 2008).

In the present study, established methods for tidal energy resource characterization and assessment are applied to Chacao Channel. The field characterization, described in Section 2.2.1, includes sea-level measurements from tidal gauges, tidal current measurements from

fixed and shipboard ADCPs at multiple locations, and a detailed characterization of turbulence using moored ADVs at a single location (Thomson et al., 2013). An FVCOM model (Chen et al., 2003) was prepared for the Chacao Channel region, using the field data for calibration and validation of the model (Section 2.2.2). The data analysis includes harmonic analysis of tidal elevation and tidal currents, quantification of spatial gradients in tidal currents, spectral analysis of turbulence, and the estimation of available power density (Section 2.3). The hydrodynamics of Chacao Channel are briefly analyzed in a discussion section.

## *2.2 Methods*

### *2.2.1 Field Characterization*

The Chacao Channel field campaign consisted of multi-month sea level and tidal current measurements at several fixed locations throughout the channel, along with short-term measurements of spatial gradients and turbulence in a single area.

The locations of the instruments are shown in Figure 2.2, where stars represent tidal gauges distributed along the south and north banks of the channel, and circles show the position of the acoustic Doppler instruments used for tidal current measurements. Previous bathymetric information of the channel is available through nautical charts from the Chilean Navy, but these are too coarse to be used in a detailed numerical model of the channel. New multi-beam bathymetry is available for this investigation. The new 10 m resolution channel bathymetry is shown in Figure 2.2. From west to east a deeper longitudinal channel is observed, beginning offshore of Carelmapu fishing village. At the narrowest part, the Roca Remolinos is observed and is surrounded by the deeper portion of the channel ($\sim$ 200 m). (This feature is the focus of Caceres et al. (2003) (Cáceres et al., 2003).) The channel ends in a deep semi-enclosed bay known as Ancud Gulf.

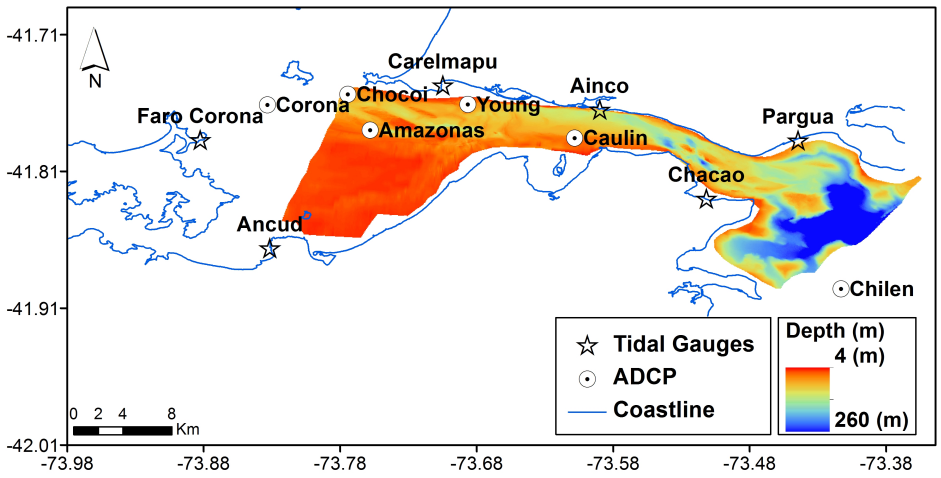


Figure 2.2: Chacao Channel high-resolution multi-beam bathymetry and instruments location along the channel. Stars represent the location of tidal gauges used to measure tidal elevation, and circles represent the location of the ADCPs used for the multi-month characterization of tidal currents.

*Tidal Elevation*

Five tidal gauges were distributed along the south and northern banks of Chacao Channel to quantify time and space variations in sea level. The specific location of each tidal gauge is shown in Figure 2.2. The tidal gauges collected data for over 30 days between May and June 2012. The gauges were set up to register sea level variations every 5 minutes with a 10 m range. The data were referenced to an unique horizontal plane, defined by the mean sea level at the Carelmapu station.

*Tidal Currents*

***Deterministic velocities***

Similarly to the sea level measurements, deterministic tidal currents in Chacao Channel were measured by six bottom-mounted RDI Workhorse Sentinel Acoustic Doppler Current Profilers (ADCPs) distributed along the channel between May and July 2012. The maximum depth of installation was approximately 40 m due to logistical constraints in the deployments.

Each doppler profiler measured three components of velocity at 1 Hz sampling frequency, then averaged these measurements every 10 minutes. These measurements were in vertical profiles, in bins spaced every 2 m. To characterize the local spatial variability of tidal currents a set of measurements was conducted following the station-keeping procedure described in (Palodichuk et al., 2013). Station-keeping is a vessel-based methodology originally developed to map small-scale variations of tidal currents as gradients between select stations. Using a vessel-mounted ADCP, vessel position is maintained at each target station for a short period of time and then each station is reoccupied several times during a tidal cycle. At Chacao Channel, measurements were collected at the corners and center of a 500 m square centered at the Young site (S 41°45.746′; W 73°40.949′) on February 12, 2013. Each of the five stations were surveyed five times during one ebb and one flood tide. The ADCP was an RDI Workhorse 1200 KHz ADCP pole-mounted to the R/V Dr. Jurgen Winter. The ADCP was set to measure three components of velocity at 2 Hz in bins spaced every 3 m, down to 30 m depth.

***Turbulent Velocities***

Turbulent velocity fluctuations were measured in a short-term deployment at the Young site, which was chosen due to its high and consistent currents, as previously detected during the long-term (deterministic) ADCP measurements. Turbulence measurements were taken using Acoustic Doppler Velocimeters (ADVs), since they are more precise than ADCPs. Specifically, ADVs provide high frequency velocity measurements with much lower Doppler noise. The ADVs were deployed using the Tidal Turbulence Mooring (TTM) method, in which the instruments are in-line along a tension mooring (Thomson et al., 2013; Harding et al., 2017; Kilcher et al., 2017). The TTM deployed in Chacao Channel consisted of a heavy anchor (approx. 1000 Kg weight) to hold the mooring in place, a buoy (approx. 300 Kg buoyancy), to hold the mooring vertical, and an instrument vane inline between anchor and buoy. Two 6MHz Nortek Vector ADVs were mounted on the instrument vane. The instruments are referred to according to the institutions providing them (i.e., the NREL ADV and the APL ADV). The two instruments targeted a tidal turbine's nominal hub-height (10

m from the sea-bottom). Both ADVs were oriented to point into the flow under all conditions (i.e., flood and ebb) by using swivels above and below the vane. The ADVs sampled the tidal currents at 16 Hz in their local XYZ coordinate system. The nominal velocity range was set at 2 $ms^{-1}$ (along-beam), which gives approximately 3.5 $ms^{-1}$ horizontal range.

The TTM deployment lasted 2.5 days, between 11 and 14 February 2013; this was a short deployment since the long-term characterization of tidal currents was already conducted via the multi-month deployment. The deployment site is approximately 38 m deep (rel. MLLW) and was approximately the same position as the Young ADCP deployment.

Contamination from mooring motion needs to be removed from turbulent velocities prior to the data analysis. For this deployment inertial motion units (IMU) were attached to each ADV in order to sample mooring acceleration (both linear and rotational) and orientation. The NREL ADV had a Microstrain 3DM-GX3 motion sensor with synchronous data acquisition; the APL ADV had a x-IMU motion sensors with asynchronous data within 1 second of the velocity data (Thomson et al., 2013). Direct motion correction (Thomson et al., 2013; Kilcher et al., 2017), which requires synchronous data acquisition between raw velocities and mooring acceleration and rotation, was applied to every point of the time series of the NREL ADV measurements. For the asynchronous motion data ADV, only a correction based on burst-averaged mooring orientation angle was applied. For this deployment, turbulent kinetic energy spectral density comparisons between the two corrected data sets show that differences are not significant when the full motion correction was not applied (shown below in Figure 2.8c)). This is because the site is highly energetic, and the turbulence signals are much larger than the motion contamination signals.

### *2.2.2 Hydrodynamic numerical model*

A numerical model of Chacao Channel was constructed to extrapolate the field measurements. This allows a study of the large spatial variations of the tidal flows in Chacao Channel, as thereby assessment of the tidal resource at potential sites throughout the Channel. The Finite-Volume Community Ocean Model (FVCOM; (Chen et al., 2003)) is used for

this purposes. FVCOM is a three-dimensional, non-structured, finite-volume hydrodynamic model that solves the primitive ocean circulation equations (Chen et al., 2003). FVCOM is widely used in the study of physical and biological processes in coastal regions characterized by complex bathymetry and diverse forcing (tides, wind, river discharge, etc.). For a detailed description of FVCOM model, the reader is referred to (Chen et al., 2003) and to the FVCOM user manual (Chen et al., 2013).

The hydrodynamic model covers the portion of Chilean Sea surrounding the island of Chiloé, including the Chacao Channel and part of the continental shelf. This domain size is necessary to: i) assess the propagation of tidal waves in the south of Chiloé Island; ii) observe the resonance phenomenon in the Chilean Internal Sea (east of Chiloé) previously described in (Aiken, 2008); and iii) to fully develop the flow that will enter Chacao Channel through the east end.

The study domain extends approximately 66,400 $km^2$. It is discretized in a non-structured mesh of approximately 50,000 triangular elements with a resolution ranging from 5000 m, in the open ocean, up to 50 m in Chacao Channel. The model bathymetry is constructed from the new high resolution bathymetric measurements, together with nautical charts from the Hydrographic and Oceanographic Service of the Chilean Navy (SHOA) for areas where no new surveys were made. Although this data is coarse, it is the only alternative bathymetric data available for the area. The sole external forcing applied in the simulations were tides. The model was forced from its western edge using 34 astronomical tidal harmonic components obtained from the global model TPXO 7.1 (Egbert and Erofeeva, 2002). The simulation domain is shown in Figure 2.1. The model limits are denoted by a green line, while the orange line denotes the forcing boundary.

The hydrodynamic model was run from May 4th 2012 until July 7th 2012 (considering 3 days to spin-up the model). This date range includes the long-term tidal elevation and tidal current measurementa, and it is sufficient to map the main harmonic components of the tidal flows of Chacao Channel. The time step was 0.2 seconds, and the output was saved every 30 minutes. The default turbulent closure schemes were used for the estimation of the

vertical eddy viscosity and horizontal diffusion coefficients, namely the modified Mellor and Yamada level 2.5 (Mellor and Yamada, 1982) and Smagorinsky (Smagorinsky, 1963) models.

## *2.3 Analysis*

### *2.3.1 Tidal Elevation*

Tidal elevation at Chacao Channel varies in time and space. In time, the tidal elevation is characterized by a mixed semidiurnal harmonic behavior at all stations, featuring two low and two high tides each day of slightly different magnitude. Figure 2.3 shows two tidal elevation time series from Carelmapu and Pargua tidal gauges. As depicted in Figure 2.3, the measurement period covered more than one lunar cycle, capturing at least two neap and two spring tides at each station. Spatial variations of tidal elevation show an increase in its amplitude, and consequently in its range, from west to east. The maximum observed tidal elevation range at Carelmapu (west) tidal gauge is 3.7 m, while at Pargua (east) the maximum range is 6.9 m. The daily inequality was also observed to increase from west to east within Chacao Channel, specially during spring tides. For the spring tide observed around day 17 (Figure 2.3) the high tide inequality at Carelmapu was 0.69 m, while the high tide inequality at Pargua was 0.96 m. For the same spring tide, there was an approximate 40 min delay between the occurrence of higher-high tide between Carelmapu and Pargua.

Harmonic analysis of tidal elevation has been conducted using the *t_tide* model developed by (Pawlowicz et al., 2002). The analysis indicates that the most energetic component at Chacao Channel is the principal lunar semidiurnal $M_2$ component. The following four most energetic components are the semi-diurnal S2 and N2, and the diurnal lunar O1 and K1 components. The $M_2$ amplitude is about 0.6 m on the west mouth of the channel, increasing to 1.8 m at Pargua station. According to (Aiken, 2008), the $M_2$ tidal elevation amplitude is expected to continue to increase within Gulf of Ancud and north to Reloncaví Sound.

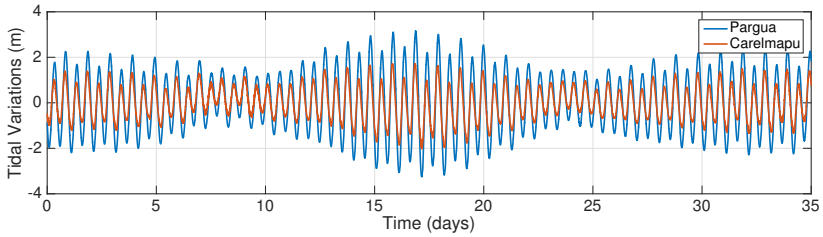


Figure 2.3: Tidal elevation variations at Carelmapu (red) and Pargua (blue) tidal gauge stations relative to their respective mean sea level elevation.

### *2.3.2 Tidal Currents*

#### ***Deterministic Currents***

The following analysis is focused in the horizontal velocity components, and the horizontal velocity magnitude and direction at each depth of the water column. The horizontal velocities are the relevant resource for extraction by tidal turbines, and, furthermore, the observed vertical velocities are two orders of magnitude smaller than horizontal velocities. The horizontal current magnitude is defined as $U = \sqrt{u^2 + v^2}$, where $u$ and $v$ represent the east and north velocities respectively. As general convention, a negative $U$ indicates ebb current (seaward) and a positive one, flood current (landward).

Tidal currents at Chacao Channel present a mixed semidiurnal regime, with two ebb and two flood currents of different magnitude each lunar day. Harmonic analysis of tidal currents is performed using the widely used *t_tide* model from (Pawlowicz et al., 2002). The $M_2$ tidal current component is predominant at all ADCP stations, being one order of magnitude greater than the next most energetic components. $M_2$ tidal ellipses for horizontal current at 10 m above the sea-bottom for all ADCP stations are shown in Figure 2.4. $M_2$ ellipse orientation and axis magnitudes vary along the channel. From west to east, ellipse orientation becomes almost inline with the channel's principal orientation. Semi-major axis values of $M_2$ current remain fairly constant along the channel (contrary to tidal elevation magnitude), then greatly decrease at Chilen station, which is outside the channel's boundaries. At Corona

ADCP station the $M_2$ semi-major amplitude is 1.6 ms$^{-1}$, increasing to be approximately 1.9 ms$^{-1}$ at Chocoi, Amazonas, Young and Caulin stations. Semi-minor axis $M_2$ values decrease as the flow gets constrained into the channel, resulting in small cross-channel flows (and large along-channel flows).

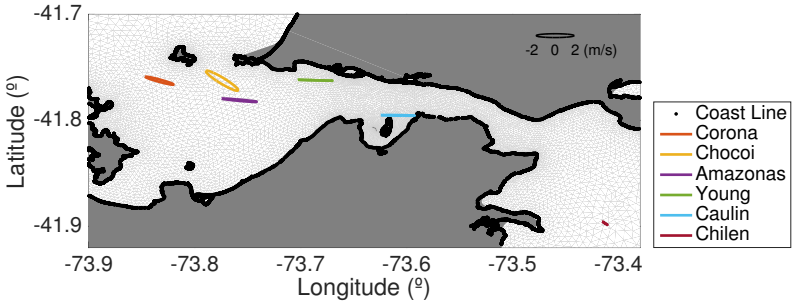


Figure 2.4: $M_2$ tidal ellipses at 10 m above the sea-bottom at each ADCP station along Chacao Channel.

Figure 2.5 shows a record of the horizontal current magnitude together with flow direction along the water column at the Young station. Harmonic behavior of horizontal currents is observed through the water column; spring and neap tidal currents are clearly observed. The maximum horizontal current observed at this site was approximately 3.5 ms$^{-1}$ at ebb tide. As seen in the record, direction varies from $\sim 90°$ (ebb) to $\sim 270°$ (flood), which is consistent with the channel's geometry and orientation. At Young, the observed time-averaged horizontal current magnitude is 1.6 ms$^{-1}$, increasing with water depth. The vertical profile shows enhanced ebb currents at all depths. The ebb/flood asymmetry indicates that mean ebb current is about 10% greater than flood mean current at all depths at this station. However, this ebb/flood magnitude asymmetry is not significant at all stations. For example, at Caulin (not shown), ebb/flood asymmetry is less than 1%. Regarding direction, the flow within Chacao Channel is mainly constrained by its west-east orientation. At Young, the principal direction of the flow is close to 90° from North, and there is small ebb/flood

directional asymmetry (maximum 4°). The direction is more variable along the water column during the flood currents.

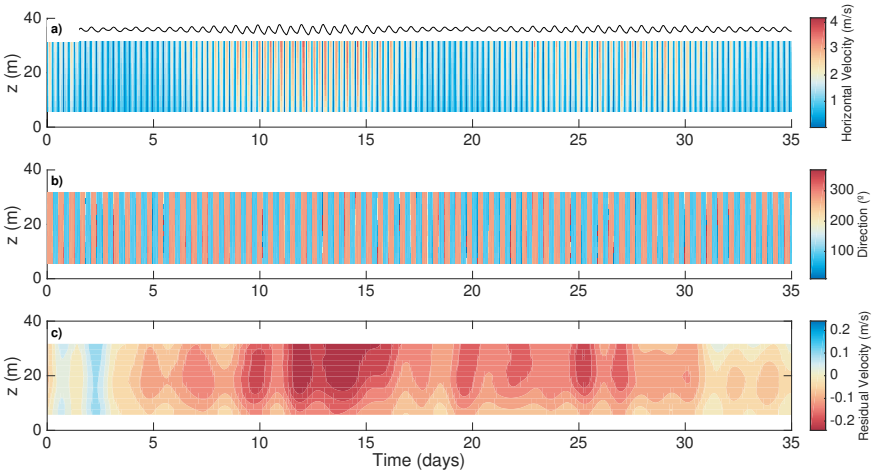


Figure 2.5: a) Horizontal current, b) direction, and c) residual flow recorded at Young station in 2012. Analysis performed with methodology from (Polagye and Thomson, 2013).

Results from the station keeping procedure around Young station are shown in Figure 2.6. The station-keeping data was collected and processed according to the methodology presented in (Palodichuk et al., 2013). High local variability in currents is observed in the across-channel direction and between ebb and flood tide. Stations closer to the shore, A and B, show significantly smaller currents than offshore stations C and D. During ebb tide, the currents increase from 2 $ms^{-1}$ to 3.5 $ms^{-1}$ in the across-channel direction, resulting in a mean gradient of 0.3 $ms^{-1}$ every 100 m. Spatial variability is enhanced during flood tides where maximum current increases from about 2 $ms^{-1}$ on stations A and B, to more than 4 $ms^{-1}$ at stations C and D. Also during flood tide, a large longitudinal variability is observed between stations C and D. These results illustrate the complex flow field variations in Chacao Channel. These large spatial gradients in velocity are of great importance for tidal energy resource assessment and the distribution of tidal turbines, as a variation of 0.3 $ms^{-1}$ in currents is equivalent to approximately a 1.4 $kWm^{-2}$ variation in power density.

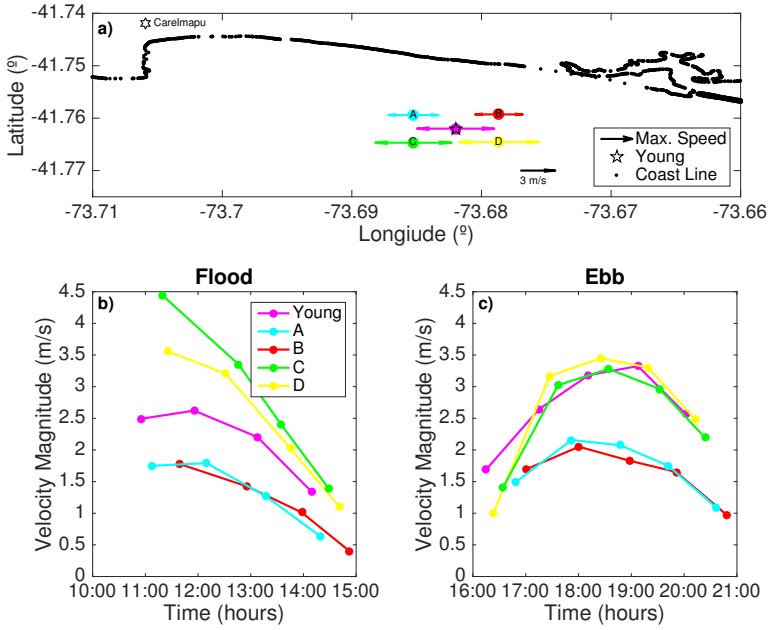


Figure 2.6: Station-keeping velocity measurements around Young station: a) Station-keeping measurement locations, and maximum recorded ebb and flood velocity magnitude (arrows) at each of the station-keeping target locations, b) Flood tide measurements, and c) Ebb tide measurements. Legend in b) and c) correspond with station-keeping locations at a).

### *Turbulent Velocities*

Turbulent variations of the mean flow are characterized in terms of turbulent intensity and turbulent kinetic energy spectra. Velocity data obtained from the ADVs onboard the TTM were corrected for TTM motions, quality-controlled to remove points with low acoustic correlations, and despiked using a 3D phase space method of Goring and Nikora (2002) (Goring and Nikora, 2002). Velocity data were processed in five minute bursts in order to ensure flow stationarity in the turbulence time-series and to capture the large scale turbulence (i.e., short enough to have a stable mean current, yet long enough to have reliable statistics) (Thomson et al., 2012; McCaffrey et al., 2015).

For every five minute burst of ADV data, the noise corrected turbulence intensity (TI)

(Thomson et al., 2012) is defined as:

$$TI = \frac{\sigma_u}{\overline{u}} = \frac{\sqrt{\sigma_u^2 - \sigma_n^2}}{\overline{u}} \tag{2.2}$$

where $\sigma_u^2$ is the variance of the velocity fluctuations, $\sigma_n^2$ is the instrument Doppler noise variance, and $\overline{u}$ is the mean along channel velocity. Mean along channel flow velocity and turbulent intensities are shown in Figure 2.7. As expected, the along channel velocity shows an harmonic behavior. TI ranges from 5 to 20% at the site, similar to other energetic tidal channels such as Admiralty Inlet, WA. (Thomson et al., 2012), however the turbulent intensity does not seem to follow a clear trend with the mean flow during the deployment.

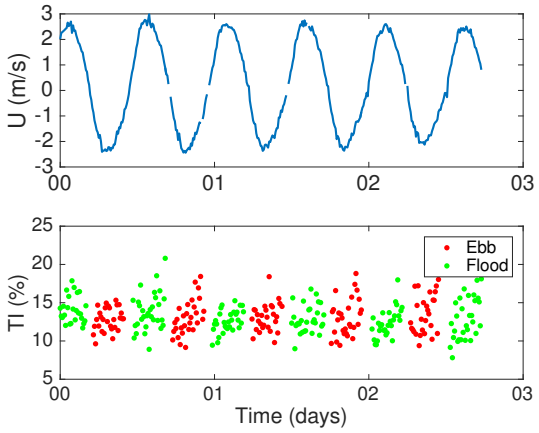


Figure 2.7: Mean current and turbulence Intensities from the February 2013 turbulence measurements at Young station.

The distribution of turbulent kinetic energy among eddies of different sizes is represented trough the turbulent kinetic energy spectra. Frequency spectra of horizontal along channel velocities and vertical velocities are calculated for every five minute burst using six 75 s sub-windows with 50% overlap and a Hanning data taper, which results in a spectral density estimate with 16 degrees of freedom. Each spectra, $S(f)$, corresponds to the turbulent kinetic energy (TKE) components of velocity such that $\langle u'^2 \rangle = \int S_u(f)df$ and $\langle w'^2 \rangle = \int S_w(f)df$.

All spectral density estimates are bin-averaged by mean along-channel velocity (0.5 $\text{ms}^{-1}$ bins) for clarity in presentation. These spectra are shown in Figure 2.8. All spectra are

well sorted by mean flow velocity, indicating that total TKE increases as mean velocity increases. Three regions are distinguished on the TKE spectra for both along-channel and vertical velocity components. At low frequencies ($f < 0.2$ Hz), a region of anisotropic eddies is observed, in which TKE reaches a maximum and remains fairly constant as frequency decreases, probably limited by the channel's lateral length scales. TKE from vertical motions is one order of magnitude smaller than TKE from horizontal motions at low frequencies (Figure 2.8 (c)), consistent with the presence of two dimensional eddies and limitation of vertical motion by the depth of the channel. At mid frequencies ($0.2 < f < 2$ Hz), an isotropic region of three-dimensional turbulence is present, which follows the classic $f^{-5/3}$ Kolmogorov's inertial subrange slope (Kolmogorov, 1941). In this region TKE is transferred from large scale eddies to short scale eddies until energy is dissipated by viscosity at even smaller scales. At higher ($f > 2$ Hz) frequencies, the spectrum becomes affected by the inherent Doppler noise of the instrument (Brumley et al., 1991). A white-noise energy level is observed around $S(f) = 10^{-4}$ m$^2$s$^{-2}$Hz$^{-1}$.

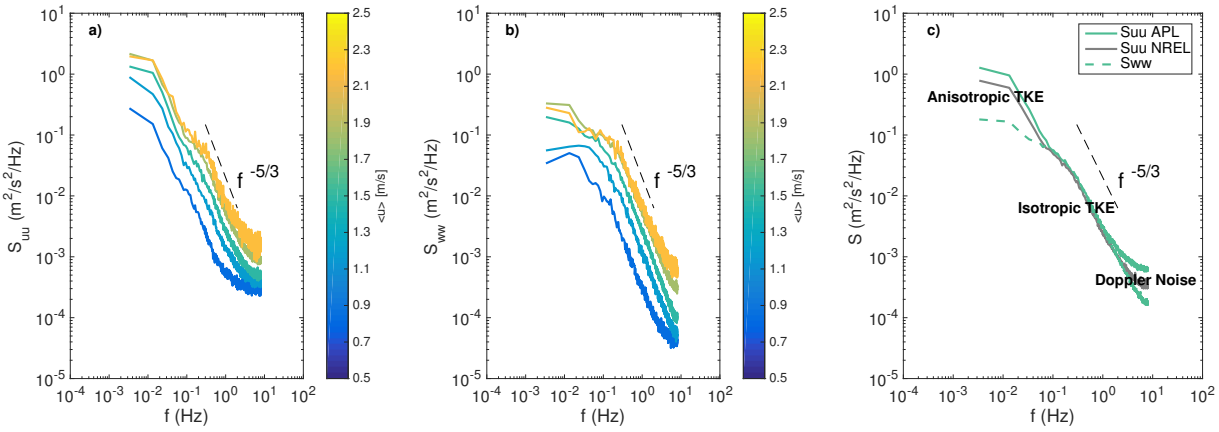


Figure 2.8: Turbulent kinetic energy spectral density estimates from APL ADV data: a) Along-channel TKE spectra sorted by mean flow conditions, b) Vertical TKE spectra sorted by mean flow conditions, and c) Along-channel and vertical TKE spectra averaged across all mean flow conditions, averaged along-channel TKE spectra from NREL ADV is included in grey. Dashed black lines show the theoretical $f^{-5/3}$ energy cascade.

### *2.3.3 Hydrodynamic numerical model*

The FVCOM numerical model results are validated by comparisons of tidal elevations, tidal currents, and turbulence parameters. The model results agree well with field measurements in terms of tidal elevation and tidal currents. Tidal elevation harmonic components are well represented by the numerical model. Estimated amplitude and phase for the $M_2$ component fall within the 95% confidence intervals for all tidal gauges stations. The relative differences of component amplitudes are less than 10%, and phase relative differences are less than 20%.

Figure 2.9 a) shows the $M_2$ tidal elevation component along the CIS, and Figure 2.9 b) shows this component within Chacao Channel. The tidal elevation amplification and phase change are well-captured by the FVCOM model, which is forced using 34 tidal components at the same time and includes the detailed bathymetry in Chacao Channel. The $M_2$ tidal elevation amplitude increases by a factor of 4 from the CIS south entrance (south of Chilo Island) towards the Ancud Gulf (Chacao Channel east end), while the phase changes 23° (not shown). This tidal wave amplification results approximately in a 2 m $M_2$ amplitude difference between the ends of Chacao Channel, consistent with both the tidal gauge observations and the Aiken (2008) (Aiken, 2008) results.

Tidal ellipses of depth integrated velocities are compared for evaluating model performance in reproducing tidal currents. The model correctly represents the semi-major and semi-minor tidal ellipses axes, and the inclination of the ellipses at all stations. The main model-data differences are in tidal phase. Vertical profiles of time-averaged horizontal speeds (averaged over the FVCOM simulation period) at the different ADCP stations are estimated following the tidal energy resource characterization methodology from (Polagye and Thomson, 2013). FVCOM time-averaged horizontal speeds agree well with the data at the ADCP stations located within Chacao Channel; relative differences are less than 10% through the water column. Greater differences are observed for the Corona ADCP station ($\approx$ 30%) and for the Chocoi ADCP station ($\approx$ 20%), which are located outside Chacao Channel boundaries, where no high-resolution bathymetry was available. From the measurements,

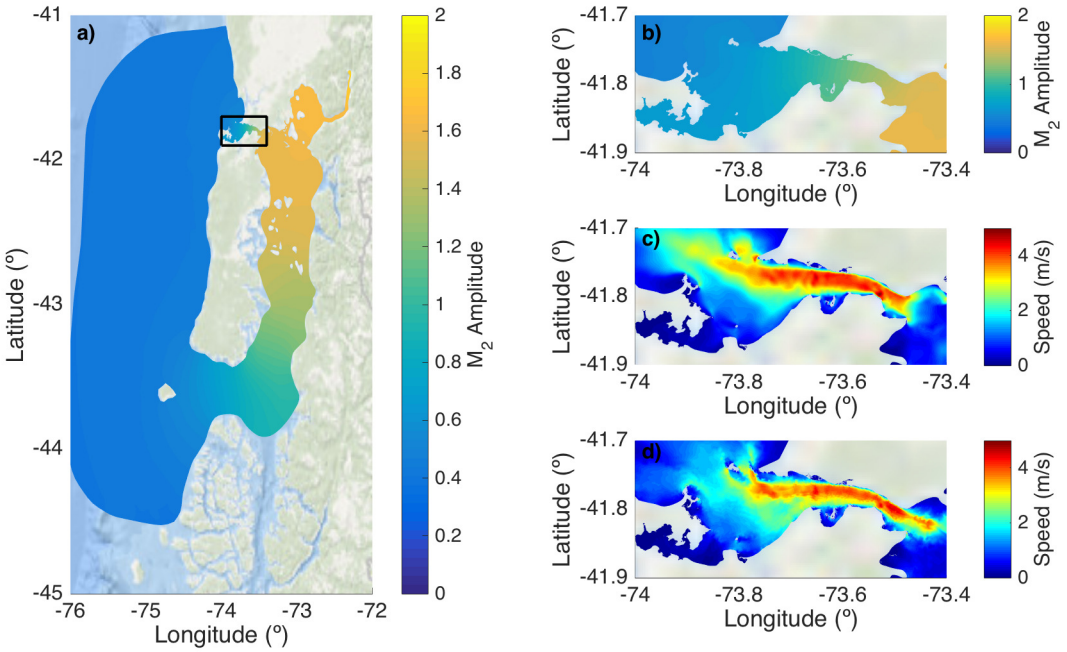


Figure 2.9: FVCOM results: a) $M_2$ Tidal elevation component along the CIS, black rectangle denotes zoom-in area within Chacao Channel, b) $M_2$ Tidal elevation component within Chacao Channel, c) maximum ebb depth averaged velocities, and d) maximum flood depth averaged velocities.

ebb-averaged horizontal speeds are of higher magnitude, this trend is reproduced in the model results for all except the Chocoi station.

Model results are also analyzed in terms of the total turbulent kinetic energy (TKE) and TKE dissipation rates, which are given by a turbulence closure scheme in the model. These turbulence parameters are compared with estimates from the TTM measurements. This analysis is included since turbulence parameters are key inputs for tidal energy infrastructure design. Due to the timing difference between the model run and the TTM measurements, continuous tidal cycles from the model output have been selected to perform the comparisons, following the matching methodology described in Thyng et al. (2013). The alignment of numerical results and field data uses the best match between along-channel tidal currents at the depth bin closest to the TTM target height.

Turbulent kinetic energy and TKE dissipation rates are a direct output from the FVCOM numerical model. The TKE from the model, defined as $TKE = 1/2(u'^2 + v'^2 + w'^2)$, includes the three components of velocity fluctuations and is assumed to be isotropic (Chen et al., 2003; Mellor and Yamada, 1982). The TKE from the field data is obtained by integrating the TKE frequency spectra estimates from section 2.3.2, and the field TKE dissipation rate is estimated from the isotropic portion of the TKE spectra as explained in section 2.4.2.

Time series of observed horizontal speed, total TKE, and TKE dissipation rates, together with numerical results from the selected period, are shown in Figure 2.10. There is good agreement for the tidal current horizontal speed and in the TKE dissipation rates, however the total TKE from measurements greatly exceeds the total TKE estimate from FVCOM. As noted in (Thyng et al., 2013), this difference likely is due to the isotropic turbulent kinetic energy assumption and the scales represented in the turbulence closure model (Mellor and Yamada, 1982). The Chacao Channel measurements indicate the dominance of anisotropic turbulence at low frequencies, yet this portion of the TKE is not captured by the model. To obtain a fair comparison between measured and modeled total TKE, a new estimate using only the inertial subrange of the field data spectra has been calculated. This isotropic-only TKE is estimated as $\mathrm{TKE}_{iso} \approx 3/2u'^2$ and is obtained from the numerical integration of the

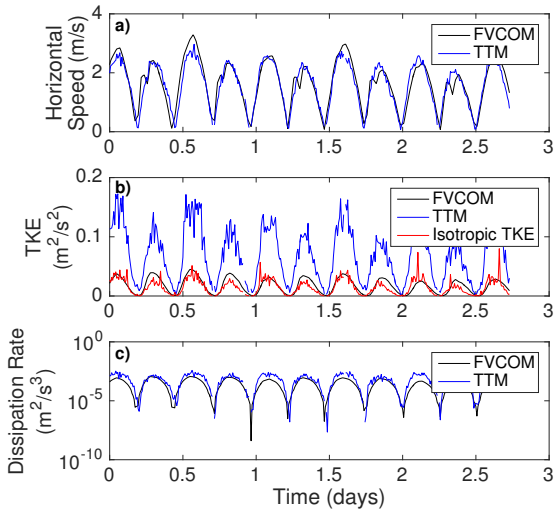


Figure 2.10: Turbulence parameters at Young Station for selected FVCOM tidal cycles and comparable field data results: a) Horizontal speed, b) Turbulent Kinetic Energy (TKE), and c) TKE Dissipation Rate

$u'^2$ TKE spectra between 0.1 and 2 Hz. Note that this isotropic TKE corresponds to what is called Classic TKE in Thyng et al. (2013). The FVCOM TKE output agrees well with the isotropic TKE estimate from field measurements, indicating that the model does well reproducing specific turbulence parameters, but that the results must be used cautiously if large scales of turbulence are of interest. A technique developed in Thyng et al. (2013) can be applied to extrapolate model results to account for the low-frequency TKE missing from the model results.

### *2.3.4 Kinetic Power Density*

Estimation of the kinetic power density available in Chacao Channel is presented below using both ADCP measurements and FVCOM results. Power density, $P$, is estimated as:

$$P = \frac{1}{2}\rho U^3 \tag{2.3}$$

where $\rho$ is the water density and $U$ is the horizontal speed. Vertical profiles of mean power

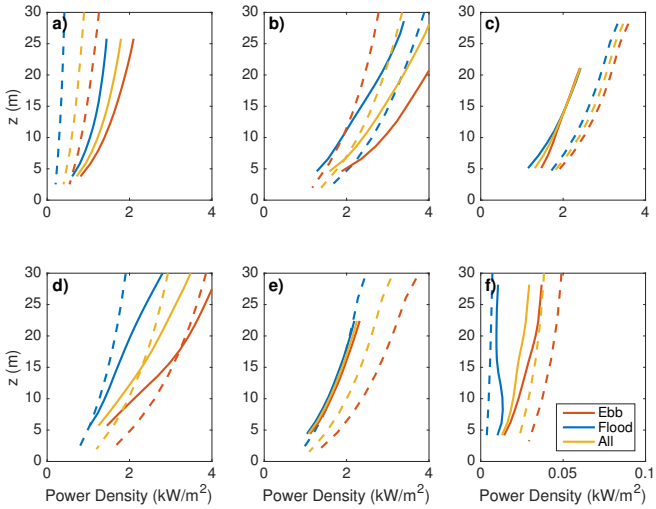


Figure 2.11: Vertical profiles of time-averaged power density estimates at ADCP stations: a) Corona, b) Chocoi, c) Amazonas, d) Young, e) Caulin, and f) Chilen. Ebb tide is in red, flood tide is in blue, and all records are in yellow. Dashed lines correspond to power estimates using FVCOM velocity profiles. Note the different scale in the Chilen station plot, this ADCP was located outside of the main Chacao Channel area.

density from ADCP data and from FVCOM results are calculated using the methodology from (Polagye and Thomson, 2013) at each ADCP station. These profiles are shown in Figure 2.11. Power density is higher at the stations within the narrow area of Chacao Channel. It is approximately 2 kWm$^{-2}$ at hub-height (10 m above sea-bottom), increasing up to 4 kWm$^{-2}$ about 30 m from the sea-bottom. For comparison, the values at the Admiralty Inlet prospective tidal energy site in Puget Sound, WA, USA, are about 2 kWm$^{-2}$ at 30 m above the sea-bottom. Overall, the power density exceeds 5 kW/m$^{-2}$ approximately 20% of the time at mid depth for the ADCP stations located within Chacao Channel (i.e except at Corona and Chilen stations). Differences between power estimations from ADCP data and those from FVCOM results are explained by the difference in horizontal velocities between measurements and model. The differences are amplified in the power profiles (in comparison with the velocity profiles) since power proportional to the cube of velocity.

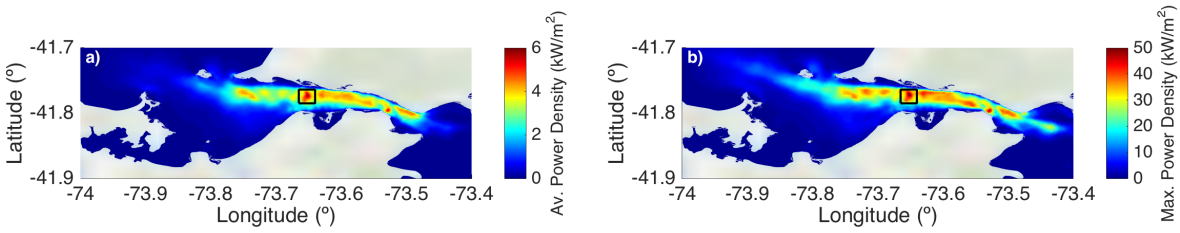


Figure 2.12: Power density estimates from FVCOM results, using depth averaged velocities in $kWm^{-2}$: a) Average power density, and b) Maximum power density. Black rectangle delimits the area with the higher averaged power density.

Figure 2.12 panels a) and b) show maps of time-averaged and maximum power density estimated using depth-averaged horizontal velocities from the FVCOM model (time-average over the modeled period). The area with the highest average and maximum power density is located at (41.78 S, 73.65W, marked with a square in Figure 2.12). This area is close to the Caulin ADCP station, which shows the less ebb/flood asymmetry in horizontal velocities, hence in power density. Depth at this area is about 60 m and currents exceed 1.5 $ms^{-1}$ approximately 60% of the time.

***Power Generation***

A simple horizontal-axis turbine model is used to estimate power generation at the ADCP stations within Chacao Channel (Chilen ADCP station is excluded due to its low power density). The turbine power output is estimated using the methodology from (Polagye and Thomson, 2013), which estimates the power output as a function of horizontal speed, the angle between the current and the turbine rotor, the turbine swept area, the overall turbine efficiency, and the water density. For this study, turbine parameters from a twin-rotor SeaGen turbine available in (Lewis et al., 2015) are used in the generation analysis. Each rotor in the model is 16 m in diameter. The cut-in speed and rated speed are 1 $ms^{-1}$ and 2.68 $ms^{-1}$, respectively (Lewis et al., 2015). The overall efficiency, assumed to be constant during all operating conditions, is 30% (Lewis et al., 2015). These parameters result in 0.6 MW rated power rotors. Hub-height is set at 15 m above the sea-bottom.

Table 2.1: Power generation estimates for a twin-rotor SeaGen horizontal-axis turbine. Power is estimated using ADCP velocity measurements.

| Location | Av. Power (MW) | Max. Power (MW) | C.F. (%) | Op. time (%) | A.E.P (MWh) |
|---|---|---|---|---|---|
| Corona | 0.18 | 1.19 | 0.15 | 0.99 | 1,585 |
| Chocoi | 0.33 | 1.19 | 0.28 | 0.99 | 2,880 |
| Amazonas | 0.27 | 1.19 | 0.23 | 0.69 | 2,386 |
| Young | 0.30 | 1.19 | 0.26 | 0.70 | 2,665 |
| Caulin | 0.26 | 1.19 | 0.22 | 0.69 | 2,250 |

Power generation estimates based on ADCP velocity measurements are shown in Table 2.1. At all tested sites, a single turbine would operate at least $\sim$ 70% of the time, with average annual energy production above 1,500 MWh. For example, a single turbine located at the Chocoi site would operate 99% of the time, generating an average of 0.33 MW. The capacity factor, defined as the ratio of average generated power and turbine rated power, is estimated to be 28%, which results in an average annual energy production (AEP) of $\sim$2,800 MWh. The same turbine located at the Young site, would operate 70% of the time, generating an average of 0.3 MW, with a capacity factor of 26%, resulting in an AEP of $\sim$2,600 MWh.

## *2.4 Discussion*

### *2.4.1 Ebb/Flood Asymmetry*

The Ebb/Flood asymmetry is defined as the ratio of the ebb and the flood time-averaged horizontal velocities (Polagye and Thomson, 2013). An ebb/flood asymmetry in the tidal currents is observed in both the measured tidal currents and in the model results at Chacao Channel.

Figures 2.9 c) and d) show maximum ebb and flood depth averaged velocities from the FVCOM model. Towards the west end of the channel (close to Carelmapu and Ancud

villages), maximum depth-averaged velocities are higher during ebb than during flood, which is consistent with the findings from the ADCP measurements.

From the ADCP stations, it is found that the ebb/flood asymmetry is more significant at the Corona, Chocoi and Young ADCP stations, where it is observed to be above 50% at 15 m from the sea-bottom. At the Amazonas ADCP station, the asymmetry is higher below 10 m from the sea-bottom (20%), and at the Caulin station, ebb/flood asymmetry is less than 1%.

The ebb dominance might be explained by residual flows oriented seaward. According to (Cáceres et al., 2003), residual flows vary in magnitude and direction across Chacao Channel due to nonlinear interactions between the currents and the channel's bathymetry (Cáceres et al., 2003). In other regions, residual flows are often an estuarine exchange driven by river discharge into an inland sea. Chacao Channel residual flows, calculated by applying a 40-hour filter to the ADCPs station data set (Polagye and Thomson, 2013), are predominantly seawards during most of the deployment at Corona, Chocoi and Young stations, with residual flows reaching 0.2 $ms^{-1}$ during spring tide. Residual flows at the Young ADCP station are shown in Figure 2.5 c). At Amazonas the residual flow is less than 0.1 $ms^{-1}$, and at Caulin it varies evenly from seaward to landward during the deployment period. Residual flows are enhanced in magnitude during spring tides, but the measurement duration is too short to observe a seasonal component in the residual flow. From the data, it is not possible to identify the source of the residual flows. However, a principal component analysis of the measured currents at Chacao Channel shows that a 99.9% of their variability is explained by barotropic circulation, while only a 0.1% of the variability is explained by baroclinic circulation.

### *2.4.2 TKE Balance*

In order to characterize the dynamics of turbulence at the Young site in Chacao Channel, and tounderstand where turbulence is being produced and dissipated, the full TKE balance

is examined, which can be written as:

$$\frac{D}{Dt}(TKE) = \nabla T + \mathscr{P} - \varepsilon \tag{2.4}$$

Where $D/Dt$ is the rate of change of TKE, $T$ is the turbulent transport of TKE, $\mathscr{P}$ is the production of TKE from the mean flow shear (positive production) and from buoyancy (negative production), and $\varepsilon$ represents the dissipation of TKE to heat and sound.

The dissipation rate of TKE, $\varepsilon$, is related to the isotropic portion of the TKE frequency spectrum by:

$$S(f) = \alpha \varepsilon^{2/3} f^{-5/3} \left(\frac{\bar{u}}{2\pi}\right)^{2/3} \tag{2.5}$$

where $\alpha$ is a constant equal to 0.69 when using the vertical TKE spectra, $\varepsilon$ is the dissipation rate, $f$ is the frequency and $\overline{u}$ is the mean along channel velocity. The dissipation of TKE is calculated from the vertical TKE spectra presented in §2.3.2. Each estimated spectra was multiplied by $f^{-5/3}$ in order to get a compensated spectra, which is expected to be horizontal (flat) in the inertial subrange. Different ranges of frequencies were considered in the fitting of the compensated spectra to a linear model. The fit with the minimum slope was chosen for the dissipation rate calculation, using at least 51 frequency bands (each of 0.01 Hz). The mean of the best linearly fitted flat spectra was estimated, and $\varepsilon$ was calculated by solving $\overline{S_{flat}} = \alpha \varepsilon^{2/3} \left(\frac{\bar{u}}{2\pi}\right)^{2/3}$.

In a well-mixed environment such as Chacao Channel (Cáceres et al., 2003), TKE loss (negative production) due to buoyancy is expected to be negligible and TKE is primarily produced by the mean flow shear. If TKE is mainly produced by bottom stress driving vertical shear, and thus lateral shear is negligible, then TKE production can be approximated as:

$$\mathscr{P} \approx -\overline{u'w'} \frac{\delta \overline{u}}{\delta z} \tag{2.6}$$

which requires an estimation of the $\overline{u'w'}$ Reynolds stress and the mean flow vertical shear $\delta\overline{u}/\delta z$. The TTM measurements provide turbulence measurements at a single location in the water column, thus it is not possible to estimate the mean flow vertical shear directly

from the those velocity measurements. Instead, the tidal current vertical profiles from the multi-month ADCP measurements of velocity at the Young station are used. The law of the wall assumption is used in order to estimate the approximate TKE production from the ADCP measurements as follows. Considering a constant stress layer, the $\overline{u'w'}$ Reynolds stress is linked to the bottom stress, and to the shear velocity $u_*$ through the drag law as

$$\tau_b = -\rho\overline{u'w'} = \rho u_*^2. \tag{2.7}$$

For a fully developed turbulent flow, the law of the wall provides the following definition for the mean flow vertical shear,

$$\frac{\delta\overline{u}}{\delta z} = \frac{u_*}{\kappa z} \tag{2.8}$$

were $u_*$ is the shear velocity, $\kappa$ is de Von Kármán constant, equal to 0.41, and $z$ de distance from the wall, or bottom, where the gradient is defined. Combining equations 2.7 and 2.8, the TKE production $P$ can be estimated as

$$\mathscr{P} = \frac{u_*^3}{\kappa z}. \tag{2.9}$$

The shear velocity $u_*$ is estimated by fitting a logarithmic profile to the horizontal velocity profile obtained from integration of equation 2.8, to each of the 10 minute averaged vertical profiles at Young station, following the methodology described in (Bassett et al., 2013).

Independent TKE production estimates and dissipation estimates are compared in Figure 2.13 for the Young site. As seen in Figure 2.13, the dissipation rate strongly follows Kolmogorov's self similarity theory $\varepsilon \sim \frac{u^3}{L}$ (Kolmogorov, 1941), were $L$ is typically a length scale given by the depth (in the absence of stratification). Although the production estimate is noisier than the dissipation estimate, a fairly good agreement between TKE the production and TKE dissipation is observed at the targeted depth. This suggests that the turbulence observed at the Young site is locally produced by bottom stress, as opposed to being produced elsewhere and advected to the site.

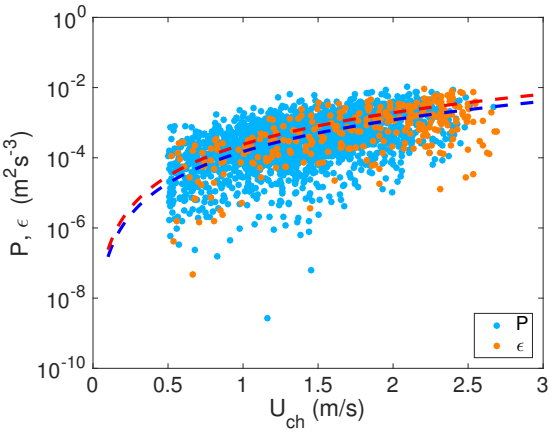


Figure 2.13: Approximate TKE Production and Dissipation rates estimates for different along-channel mean flow conditions at the Young site. Light blue and orange dots respectively represent TKE production and dissipation rates. Blue and red dashed lines represent the best non-linear fit to $\sim u^3$ for $P$ and $\varepsilon$ estimates respectively.

## *2.5 Conclusions*

The tidal energy resource of Chacao Channel is characterized from field measurements and assessed from numerical simulations. Six sites along Chacao Channel are characterized using bottom-mounted ADCP measurements. Local variability of currents and turbulence are characterized at the Young site (offshore Carelmapu) using shipboard ADCP measurements and a mid-water mooring.

The results show that several areas of Chacao Channel are suitable for tidal current energy extraction, with mean kinetic power density above 5 kWm$^-$2 more than 20% of the time at depths less than 60 m. This large kinetic resource is associated with sea elevation tidal harmonic components within Chacao Channel that increase in amplitude from east to west and significantly change in phase (1.2 m and 20° respectively for $M_2$). The underlying dynamic is tidal wave resonance within the northern portion of the Chilean Inland Sea (Aiken, 2008).

Tidal currents are largely harmonic along the channel, with currents that surpass 4 ms$^{-1}$

during spring tides in the narrower parts of the channel. Currents above 1.0 $ms^{-1}$ are observed more than 65% of the time during a monthly tidal cycle. Despite the ubiquitous high currents, significant local variability is observed in the vicinity of the Young site, with currents increasing more than 1 $ms^{-1}$ within 500 m in the cross-channel direction offshore of Carelmapu. These variations show the necessity to conduct higher resolution measurements and modeling when defining crucial aspects of tidal energy projects, such as turbine array location and distribution (sometimes referred to as micro-siting).

Turbulent velocity fluctuations are analyzed at the Young site using the compliant mooring approach from (Thomson et al., 2013). Turbulence intensities range between 5 to 20% and do not show a clear relation with the mean flow. Spectral analysis shows highly energetic anisotropic turbulence, probably related to the bathymetric features of the channel, together with a clear isotropic energy cascade that follows the theoretical relation of $f^{-5/3}$. Dissipation rate estimates from the TKE spectra follow the theoretical relation with $\bar{u}^3$. The turbulent kinetic energy budget suggest a local TKE production-dissipation balance at mid depth, implying that turbulence is locally produced and dissipated, and that TKE transport is less significant.

The FVCOM hydrodynamic model correctly captures the tidal dynamics within the Chilean Internal Sea and Chacao Channel; surface elevation and tidal ellipses agree well with measurements. In terms of turbulence parameters, the model correctly reproduces the isotropic portion of the turbulent kinetic energy. However, the model fails in describing the anisotropic portion of the turbulent kinetic energy, because these scales are outside of the formulation of the turbulence closure scheme. This is particularly important for turbine design, as hydrokinetic turbines might react to a wide range of turbulence length-scales, including the anisotropic range of scales. Thus, numerical model results are valuable for tidal resource energy application, but must be used with caution for tidal turbine design inputs (i.e., turbulence) (Thyng et al., 2013). This constraint can be overcome by following the method developed in (Thyng et al., 2013) to extrapolate the scales not captured by the model.

The gathered information and numerical model results constitute a knowledge base for future tidal energy development in the region, including more detailed resource assessments and definition of priority sites. Model results can also be used for integration with high resolution turbulence models of tidal energy turbines. Other areas of application include contaminant dispersion, sediment transport, and analysis of residual flows.

# Chapter 3

# TURBULENCE MEASUREMENTS FROM 5-BEAM ACOUSTIC DOPPLER CURRENT PROFILERS

## *3.1 Introduction*

Acoustic Doppler Current Profilers (ADCPs) are commonly used to measure the horizontal components of fluid velocities along depth profiles in the ocean using three or four diverging acoustic beams. The raw data from ADCPs, termed pings, correspond to single velocity measurements in the along-beam direction. The raw ping data are typically burst-averaged in time (5 -10 minutes for tidal flows to ensure stationary mean flow conditions (McCaffrey et al., 2015)). Averaging reduces the Doppler noise inherent to the measurement, which can add significant variance to the raw signals (above and beyond the variance due to real turbulent fluctuations) (Brumley et al., 1991). However, if the raw along-beam velocities are retained, many turbulence parameters, such as turbulent kinetic energy dissipation rates and Reynolds stresses, can be estimated from ADCP measurements. Estimation methods are based on the variance and correlations of the along-beam velocity fluctuations, often with explicit removal of the variance contributed by the Doppler noise (Lu and Lueck, 1999; Stacey et al., 1999; Wiles et al., 2006; Thomson et al., 2012).

Indirect methods to estimate turbulent dissipation rates, such as turbulence kinetic energy (TKE) spectra and the turbulence structure functions (Pope, 2001), are based on Kolmogorov's hypothesis about the existence of a range of turbulent length scales within the isotropic turbulence energy cascade, known as inertial subrange, in which the energy transfer is solely determined by the dissipation rate (Kolmogorov, 1941; Pope, 2001). The application of these methods requires the observation the inertial subrange in the data (Pope, 2001).

In the frequency domain, some authors (e.g Thomson et al., 2012; Richard et al., 2013;

Durgesh et al., 2014) have attempted to use spectra calculated from raw along-beam velocity ADCP data, but the inherent Doppler noise typically obscures the inertial subrange (Richard et al., 2013). Recently, turbulence dissipation rates have been estimated from turbulence spectra after averaging the frequency spectra for different mean flows and bins in order to successfully observe the inertial subrange in the turbulence energy cascade in McMillan et al. (2016) and (McMillan and Hay, 2017). Another common technique is to estimate turbulent dissipation rates using the second-order spatial structure function of turbulence (Wiles et al., 2006; Rusello and Cowen, 2011).

One of the most frequently used techniques to estimate Reynolds stresses from ADCP along-beam velocities is the variance technique (Lu and Lueck, 1999; Stacey et al., 1999; Rippeth et al., 2003), which provides two components (out of six) of the Reynolds stresses and is based on the variance of opposite beam velocity fluctuations.

A new generation of broadband 5-beam ADCPs with the ability to measure flow velocity at higher frequencies and with lower noise levels is poised to expand routine turbulence measurements. Moreover, the inclusion of a fifth beam allows for a true measurement of vertical velocities and the estimation of five (out of six) Reynolds stresses, total turbulent kinetic energy (TKE), and anisotropy directly from the along-beam velocities (Lu and Lueck, 1999; Dewey and Stringer, 2007). This is a notable expansion beyond the four-beam variance methods (Lu and Lueck, 1999; Stacey et al., 1999; Rippeth et al., 2003). These new features, together with the integration of inertial motion units, might even expand the application of these ADCPs to the study of upper ocean turbulence and wave breaking turbulence, and to improve the estimation of parameters used in turbulence models.

This paper presents turbulence measurements from two new 5-beam acoustic current profilers: the Nortek Signature 1000 (kHz), which uses the acronym AD2CP to distinguish it from the previous generation of profilers, and the new Teledyne RDI Sentinel V50 500 (kHz). The new instruments' capabilities are assessed in two field deployments in highly energetic tidal channels, calculations of turbulence parameters, and the subsequent evaluation of turbulent kinetic energy (TKE) budgets.

The results are validated using measurements from Acoustic Doppler Velocimeters (ADVs), which are typically the preferred choice for turbulence measurements. However, ADVs only measure at a point, and their deployment at mid-depths requires complicated moorings and subsequent motion corrections to the raw data (Thomson et al., 2013). The new ADCPs are shown to be a more practical alternative to ADVs, with the potential for new insights about where turbulence is being produced and dissipated in the water column.

In Section 2 details of the field measurements are presented. In Section 3, estimates of the TKE dissipation rate are presented using two different methods: the TKE frequency spectra and the second-order spatial structure function. In Section 4, the terms of the TKE production rate are estimated; in particular, Reynolds stresses are calculated using along-beam velocities from all five beams. Finally, in Section 5, the TKE dissipation and production rate estimates are used to examine the TKE budget at the two tidal channels.

## *3.2 Data Collection*

### *3.2.1 Site Description*

Turbulence measurements were taken at Admiralty Inlet and Rich Passage, two tidal channels located in Puget Sound, WA, USA. Figure 3.1a shows the location of the field sites and the detailed locations of the instruments. A summary of the deployments and instrument settings is presented in Table 5.1.

Admiralty Inlet is located in the northern part of Puget Sound (48.14°N, 122.71° W). Admiralty Inlet is $\sim$ 6.5 km wide and $\sim$ 50 m deep at the measurement site. The principal direction of the flow is $\sim 50°$ from the east in the clockwise direction.

Rich Passage is located south of Bainbridge island in Puget Sound (47.59° N, 122.56° W). At the measurements site the channel is $\sim$ 24 m deep and $\sim$ 550 m wide. The channel is oriented $\sim 45°$ from north in the clockwise direction.

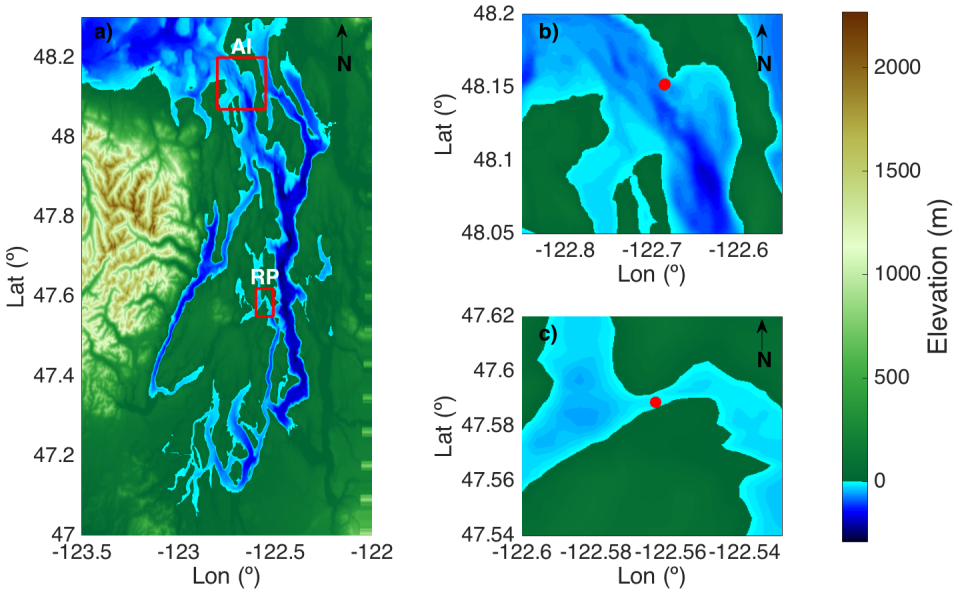


Figure 3.1: Bathymetry and location of the two tidal channels: a) Puget Sound in Washington, U.S.A., b) Admiralty Inlet (AI) and c) Rich Passage (RP). Red dots indicate instruments location.

### *3.2.2 Instruments and Settings*

The 5-beam Doppler profilers were deployed mounted looking upward on separate Oceanscience Sea Spider tripods, which place each instrument $\sim 0.9$ m above the seafloor when deployed. The instruments have four beams slanted at 25° from the vertical, plus a fifth vertical beam. Deployments were on May 11 2015 at Admiralty Inlet and on May $17-18$ 2015 at Rich Passage. Table 5.1 summarizes the deployments and sampling parameters.

The Nortek Signature was configured to measure turbulence in along-beam coordinates using its five beams at 8 Hz (the maximum possible when using all five beams) for bursts lasting 10 minutes in duration. At Admiralty Inlet, the interval between bursts was 20 minutes and there were 20 velocity bins at 1 m spacing. At Rich Passage, the interval between bursts was thirty minutes and there were 15 velocity bins at 1 m spacing.

The Teledyne RDI Sentinel V50 was configured to measure along-beam turbulent veloc-

ities at 2 Hz (the maximum possible when using all five beams) for 10 minute bursts with a 20 minute interval. At Admiralty Inlet, the RDI Sentinel V50 tripod was $\sim$ 80 m away from the Nortek Signature tripod and there were 20 velocity bins at 1 m spacing. At Rich Passage, the Sentinel V50 was not deployed (it was unavailable).

In addition to the two 5-beam Acoustic Doppler Current Profilers, Acoustic Doppler Velocimeters (ADVs) were deployed at both sites in the vicinity of the instruments in order to compare and validate the data from the profilers.

At Admiralty Inlet, a Nortek Vector ADV was deployed 130 m east of the Nortek Signature on board a Tidal Turbulence Mooring (TTM) (Thomson et al., 2013; Harding et al., 2017; Kilcher et al., 2017) on May $11 - 13$ 2015. The TTM consists of an anchor (approx. 1000 kg wet weight) to hold the mooring in place, a sphere (approx. 300 kg positive buoyancy) to hold the mooring vertical, and an instrumentation vane inline between the anchor and the buoy where the ADV was mounted. The TTM positions the ADV at 10 m above the sea bottom. The ADV was set to measure velocities at 16 Hz continuously. An inertial motion unit (IMU) synchronously measured TTM acceleration and orientation; these data are used to remove contaminations of mooring motion from the ADV turbulent velocities. The motion correction method is described in detail in Thomson et al. (2013) and Kilcher et al. (2017).

At Rich Passage, a Nortek Vector ADV was deployed in the same location as the Nortek Signature. The ADV was mounted on a Turbulence Torpedo (TT), a sounding weight that hangs from a davit on the side of the ship while the ship is holding station (Thomson et al., 2013; Harding et al., 2017; Kilcher et al., 2017). The Turbulence Torpedo ADV was deployed on June 5 2015, sampling turbulent velocities at 16 Hz for 2.5 hours during ebb tide (mean flow ranging between 1.5 and 2 m/s). Motion corrections were applied to the velocity measurements following the same methods used for the TTM ADV measurements (Thomson et al., 2013; Kilcher et al., 2017).

Table 3.1: Summary of deployments and sampling parameters at Admiralty Inlet and Rich Passage.

| Location | Admiralty Inlet | Admiralty Inlet | Admiralty Inlet | Rich Passage | Rich Passage |
|---|---|---|---|---|---|
| Instrument | Nortek Signature 1000 | RDI Sentinel V50 | Nortek Vector ADV | Nortek Signature 1000 | Nortek Vector ADV |
| Latitude (°) | 48.1522 | 48.1517 | 48.1524 | 47.5887 | 47.5887 |
| Longitude (°) | -122.6852 | -122.6858 | -122.6868 | -122.5641 | -122.5641 |
| Water Depth (m) | 50 | 50 | 50 | 24 | 24 |
| Deployment Duration (days) | 2 | 2 | 2 | 2 | 0.1 |
| Sampling Frequency (Hz) | 8 | 2 | 16 | 8 | 16 |
| Burst-Average (min) | 10 | 10 | 10 | 10 | 10 |
| $\Delta z$ (m) | 1 | 1 | - | 1 | - |
| Distance to first cell (m) | 0.5 | 0.5 | - | 0.5 | - |
| Range (m) | 20.5 | 20.5 | - | 15.5 | - |
| z target (m) | - | - | 10 | - | 17 |
| Single ping error ($ms^{-1}$) | 0.016 | 0.003 | 0.02 | 0.016 | 0.02 |
| Empirical error ($ms^{-1}$) | 0.027 | 0.054 | 0.011 | 0.027 | 0.011 |
| Pitch ° | 2.26 ± 0.005 | 4.45 ± 0.06 | - | 0.35 ± 0.002 | - |
| Roll ° | 0.36 ± 0.02 | -1.61 ± 0.01 | - | -1.19 ± 0.004 | - |

### *3.2.3 Raw Data*

Figure 3.2 shows vertical profiles, and time series, of along channel velocity (after a coordinate transformation of the beam velocities) measured by the Nortek Signature for both study sites. At Admiralty Inlet, it was possible to measure only a single tidal cycle due to the rapid battery consumption when sampling at high frequency and not using external battery canisters. After approximately 12 hours, the Nortek Signature kept sampling, but the bursts became shorter (less than the 10 minutes setting). At Rich Passage, a reduced duty cycle made it possible to measure two tidal cycles before the bursts became shorter. For both deployments, a single battery pack was used, but additional battery packs can be externally connected to the instrument to overcome the limits from rapid battery consumption. According to the Nortek Signature Deployment software, for a deployment using the same settings as for the Admiralty Inlet Signature deployment, the instrument life can extended to 158 days when using a 3600 Wh Lithium external battery pack. For the same deployment settings, a memory card of 64 GB capacity would last 179.5 days (and thereby exceed the

limitations of the external batteries).

A ten-minute time interval is selected for burst-averaging these data sets and for estimation of statistical parameters (spectra, structure function, etc). This time interval is chosen as short enough to remove any trend contamination from tidal currents in the turbulence time-series (i.e short enough so that the tidal current does not change), but long enough to capture the large scale turbulence (McCaffrey et al., 2015). An analysis of this time interval selection for turbulence analysis in tidal channels is available in McCaffrey et al. (2015).

The maximum observed burst-averaged horizontal speed at Admiralty Inlet was 2.04 m/s during flood which corresponds to a Reynolds number of $\mathcal{O}(10^8)$. At Rich Passage the maximum burst-averaged observed horizontal speed was 1.95 m/s during ebb, which corresponds to a Reynolds number of $\mathcal{O}(10^7)$. Although these are short datasets, they are sufficient to observe turbulent velocity fluctuations at a wide range of mean flow conditions at each site (e.g., 10 minute burst-averaged horizontal speeds varied from 0 to 2 m/s). Data are quality controlled to remove measurements with low beam correlations (less than 50) and low echo amplitude (less than 30 dB), as per manufacturer recommendation. This removes a very small fraction (less than 0.5%) of the raw data.

## *3.3 Analysis: Turbulent Kinetic Energy Dissipation Rate*

At each depth in the ADCPs measured profiles, the TKE dissipation rate is estimated by two methodologies: from the frequency spectra (Lumley and Terray, 1983) and from the spatial structure function (Wiles et al., 2006). Both methods are derived from Kolmorogv's turbulence hypotheses (Kolmogorov, 1941; Pope, 2001) and require the observation of the inertial subrange of isotropic turbulence.

### *3.3.1 Turbulent Kinetic Energy Spectra*

The distribution of turbulent kinetic energy among eddies of different sizes is represented trough the turbulent kinetic energy spectra. Assuming stationarity, the turbulence advected past the instruments at average speeds $\overline{u}$ has frequency ($f$) spectra that are related to the

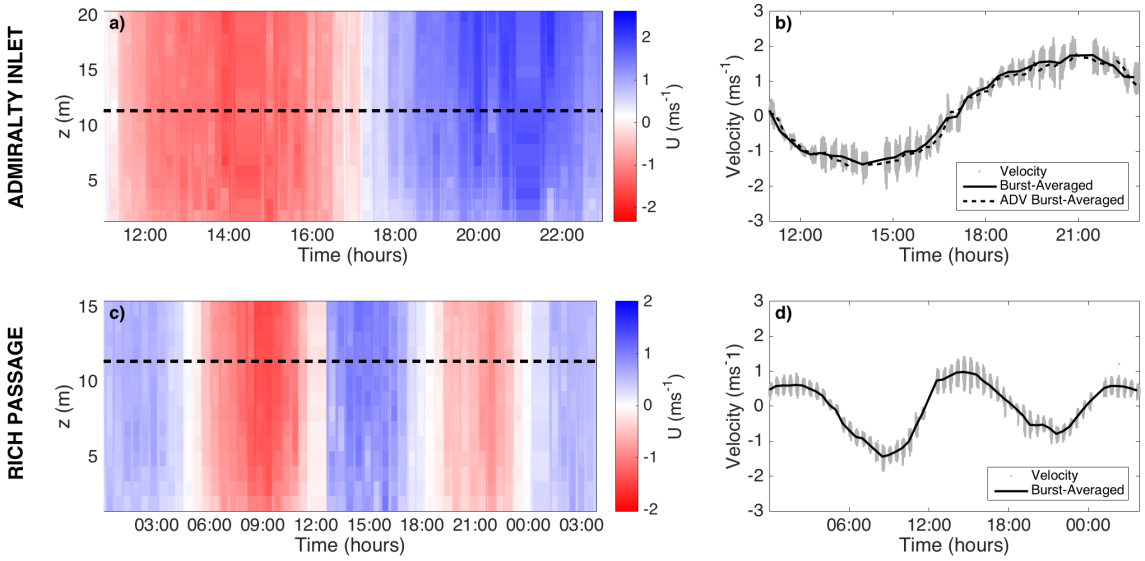


Figure 3.2: Vertical profiles and time series of along-channel velocities measured with the Nortek Signature: a), b) at Admiralty Inlet, and c), d) at Rich Passage. In a) and c) black dashed line indicates depth corresponding to the time series (as $z = 10.4$ m from sea-bottom). In b) and d), grey dots correspond to measured along-channel velocity, and black line corresponds to 10 minute burst-averaged along-channel velocity. Burst-averaged along-channel velocity measured with the TTM ADV at Admiralty Inlet is included as a black dashed line in b).

wavenumber ($k$) spectra by $\bar{u} \propto f/k$ (i.e., Taylor's frozen field). Thus, the frequency spectra are expected to include an inertial sub-range, in which the turbulent kinetic energy follows $f^{-5/3}$ as a manifestation of the energy cascade following $k^{-5/3}$ (Kolmogorov, 1941; Pope, 2001).

TKE spectra are estimated using Welch's Overlapped Segment Averaging method applied to the vertical beam velocities (beam 5). For the Nortek Signature data sets, spectral estimates are calculated for every ten-minute burst using 23 50 s sub-windows with 50% overlap and a Hanning data taper, which results in an ensemble spectral density estimate with $\sim$ 45 degrees of freedom. TKE spectra with the same degrees of freedom are also

estimated for the RDI Sentinel V50 vertical beam velocities and for the Nortek Vector ADV measurements.

TKE spectra estimates for both sites for the tenth vertical bin (10.4 m from the sea bottom) are presented in Figure 3.3 colored by mean flow conditions. The TKE spectra estimates from the RDI Sentinel V50 measurements for the same bin are included in the Admiralty Inlet figures in grey. Averaged TKE spectra from the Nortek Vector ADV data is included for comparison as a red dashed line when available; the range of TKE spectra from the TTM ADV data is included as a pink area in the Admiralty Inlet plots. In this analysis, mean flows that are close to slack conditions ($\overline{u} < 0.5$ m/s) have been removed as the spectra does not show the theoretical $f^{-5/3}$ slope. Spectral density estimates from the Nortek Signature data are generally well sorted by mean flow velocity, implying that a higher TKE is observed at higher mean flows. The exception is during the stronger ebb at Rich Passage, where the instrument is in the lee of a sill.

The most novel result from the Nortek Signature data is the clear observation of the TKE energy cascade in the spectral estimates, which is usually obscured by the Doppler noise of profiling instruments. An isotropic region of tridimensional turbulence is present at mid frequencies ($0.1 < f < 1$ Hz) which follows the classic $f^{-5/3}$ energy cascade (Kolmogorov, 1941). At higher ($f > 1$ Hz) frequencies, the spectra become affected by the instrument inherent Doppler noise. The spectral noise level of the Nortek Signature is observed around $S_w(f) = 10^{-4}$ m$^2$s$^{-2}$Hz$^{-1}$, while the noise level of the Nortek Vector is observed around $S_w(f) = 10^{-5}$ m$^2$s$^{-2}$Hz$^{-1}$. The noise level of the RDI Sentinel V50, by contrast, is much higher at $S_w(f) = 10^{-2}$ m$^2$s$^{-2}$Hz$^{-1}$, and thus the inertial subrange is typically obscured in those spectra.

The lower spectral noise floor observed from the Nortek Signature data might be attributed to its ability to sample faster. Even if the single-ping error were the same between the RDI Sentinel V50 and the Nortek Signature, the noise floor observed in a spectral density will still be lower when the sampling is faster, as it is redistributed along a wider frequency range. In order to fairly compare the observed spectral noise floor of the two profilers, the

data from the Nortek Signature is sub-sampled down to 2 Hz and new spectra are estimated (but not shown). For the sub-sampled case, the TKE energy cascade is still observed between $0.1 < f < 0.8$ Hz, and the noise level is observed around $S_w(f) = 2 * 10^{-4}$ m$^2$s$^{-2}$Hz$^{-1}$. This is slightly higher than when sampling at 8 Hz, but not nearly as high as the spectral noise level of the RDI. The latter implies that even when sampling at the same frequency, the Nortek Signature presents a lower Doppler noise. The higher noise level of the RDI Sentinel V50 data obscures the inertial subrange in these TKE spectra, preventing the following estimation of TKE dissipation rate.

Figure 3.4 shows spectral estimates at maximum ebb and flood at the two sites for all vertical bins from the Nortek Signature data. The spectral estimates are well-sorted by depth, except for the maximum ebb at Rich Passage due to the existence of a vertical sill upstream of the measurement location. TKE density decreases as the distance from the bottom increases, consistent with bottom-generated turbulence. In the higher bins, the observable portion of the inertial subrange becomes narrower due to the decrease in TKE density (i.e., the noise floor affects spectra at a lower frequency); for example at 20.4 m from the sea bottom the inertial subrange is observed at $0.1 < f < 0.6$ Hz.

The dissipation rate of TKE, $\varepsilon$, is related to the isotropic portion of the vertical TKE frequency spectrum by:

$$S_w(f) = \alpha \varepsilon^{2/3} f^{-5/3} \left( \frac{\bar{u}}{2\pi} \right)^{2/3} \tag{3.1}$$

where $\alpha$ is a constant equal to 0.69 (Sreenivasan, 1995), $\varepsilon$ is the TKE dissipation rate, $f$ is the frequency and $\overline{u}$ is the mean along channel velocity. This applies Taylor's ' frozen field hypothesis ', which assumes that the turbulence is in steady state as it advects past the instrument (neither developing nor decaying), such that we can transform the temporal observation into a spatial one (i.e., $f = \overline{u}k/2\pi$, where $k$ is the spatial wavenumber).

Each estimated spectra is multiplied by $f^{5/3}$ to obtain a compensated spectra, which should be horizontal (flat) in the presence of an inertial subrange. The dissipation rate is estimated by solving $\overline{S_w(f) f^{5/3}\big|_{f_1}^{f_2}} = \alpha \varepsilon^{2/3} \left( \frac{\bar{u}}{2\pi} \right)^{2/3}$, where $f_1$ to $f_2$ is the frequency range with the slope closest to zero in the compensated spectra. The range of frequencies used

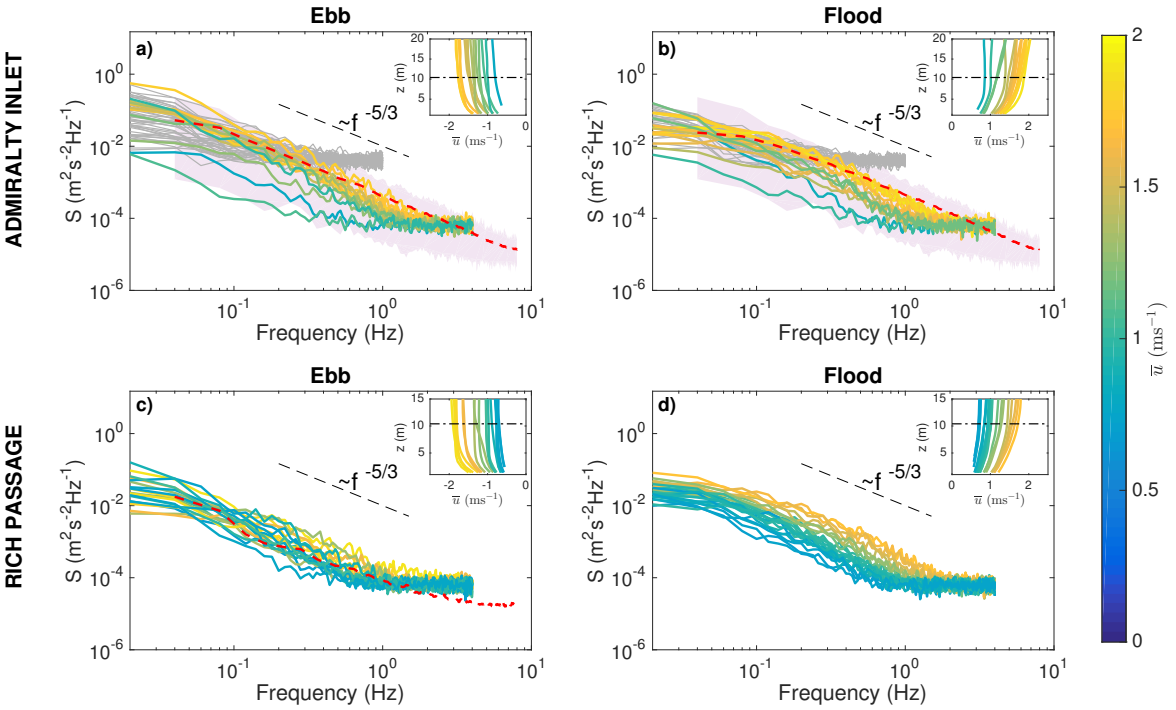


Figure 3.3: TKE spectra at $z = 10.4$ m for different mean flows (by color): a), b) at Admiralty Inlet, and c), d) at Rich Passage. Dashed black line is proportional to $f^{-5/3}$. Inset plots show burst-average horizontal speed vertical profiles (also by color); dot-dashed line shows $z = 10.4$ m in the profiles. In the Admiralty Inlet plots, spectra from the RDI Sentinel V50 data are included as grey curves, and the range of spectra from the TTM ADV data is included as a light pink are. Dashed line corresponds to averaged spectra from ADV data.

to estimate the mean compensated spectra, $\overline{S_w(f)f^{5/3}}$, varies according to the position of the inertial subrange for different mean flows and depths, ranging between $0.1 < f < 1$ Hz. A minimum of five frequencies are used to estimate dissipation rates from the compensated spectra.

Uncertainties in the TKE dissipation rates from spectra are calculated by propagating the uncertainty in the compensated spectra (Bassett et al., 2013), such that:

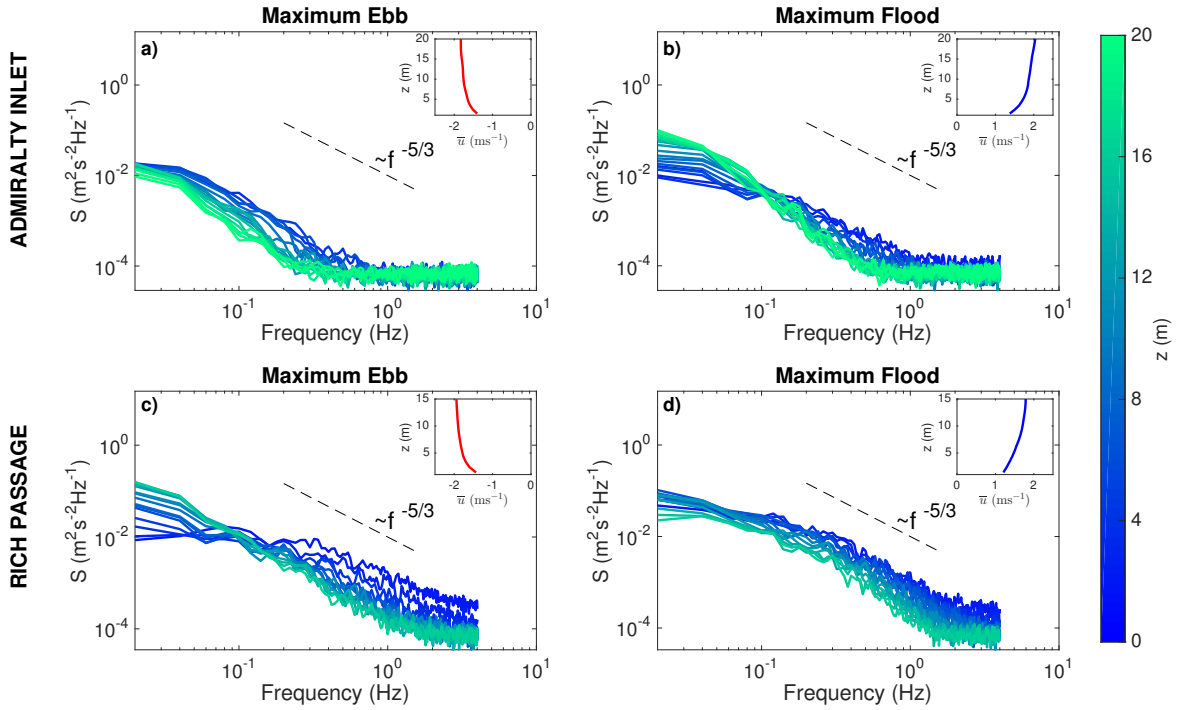


Figure 3.4: TKE spectra at maximum ebb and flood mean flow conditions at different depths (by color): a), b) at Admiralty Inlet, and c), d) at Rich Passage. Dashed black line is proportional to $f^{-5/3}$. Inset plots show corresponding mean flow vertical profile.

$$\sigma_{\varepsilon_S} = \frac{2\pi}{\overline{u}} \left(\frac{1}{\alpha}\right)^{3/2} \frac{3}{2} \overline{S_{w_{comp}}}^{1/2} \sigma_{S_{w_{comp}}} \tag{3.2}$$

where $\sigma_{\varepsilon_S}$ is the uncertainty in the dissipation rate estimate, and $\sigma_{S_{w_{comp}}}$ is taken to be the variance of the compensated spectra in the range of frequencies used to estimate $\varepsilon$.

### *3.3.2 Turbulence Structure Function*

The along-beam velocities can be used to estimate the second-order spatial structure function of the along-beam turbulent fluctuations, $D(z, r)$, following the methodology described in (Wiles et al., 2006). The structure function is defined as:

$$D_i(z,r) = \langle (u_i'(z+r) - u_i'(z))^2 \rangle \tag{3.3}$$

where $z$ is the along-beam measurement location, $u_i'$ corresponds to each along-beam velocity fluctuation, and $r$ is the distance between two velocity bins; the angle brackets denote a time average over the burst (ten-minute bursts for these data sets).

The structure function $D_i(z,r)$ is estimated from the bottom of the profile upwards. The distance $r$ is set to be positive and limited by the distance to the closest boundary, which in these cases is the sea bottom. Figure 3.5 shows examples of the spatial structure function for the vertical beam turbulent fluctuations, $D_5(z,r)$, at $z = 10.4$ m from the sea bottom at both sites. The structure function estimates from the RDI Sentinel V50 measurements for the same bin are included in the Admiralty Inlet figures in grey. Structure functions from the Nortek Signature data are generally well-sorted by the mean flow, except during the stronger ebb at Rich Passage, where again the sill creates a region of low turbulence. The slopes of the structure functions from the Nortek Signature agree well with the expected $r^{2/3}$ at both sites. Again, it is not possible to observe the theoretical $r^{2/3}$ slope in the structure function estimates from the RDI Sentinel V50. The structure function off-set at $r = 0$, $N$, is related to the instrument Doppler noise, $\sigma_N$, as $N = 2 * \sigma_N$ (Wiles et al., 2006; Thomson, 2012). A higher offset $N$ is observed in the RDI Sentinel V50 structure functions due to its higher Doppler noise, which prevents the structure function drop-off as $r$ approaches zero, obscuring the $r^{2/3}$ slope, and thus limiting the estimation of the TKE dissipation rate. In these measurements, the 1 m bin size limits the observed turbulence length-scales, and particularly affects the observation of the inertial subrange in the turbulence structure function (McMillan and Hay, 2017).

In the inertial subrange, the structure function is related to the distance $r$ and to the dissipation rate $\varepsilon$ by:

$$D_i(z,r) = C_v^2 \varepsilon^{2/3} r^{2/3} \tag{3.4}$$

where $C_v^2$ is a constant equal to 2.1 (Wiles et al., 2006; Thomson et al., 2012).

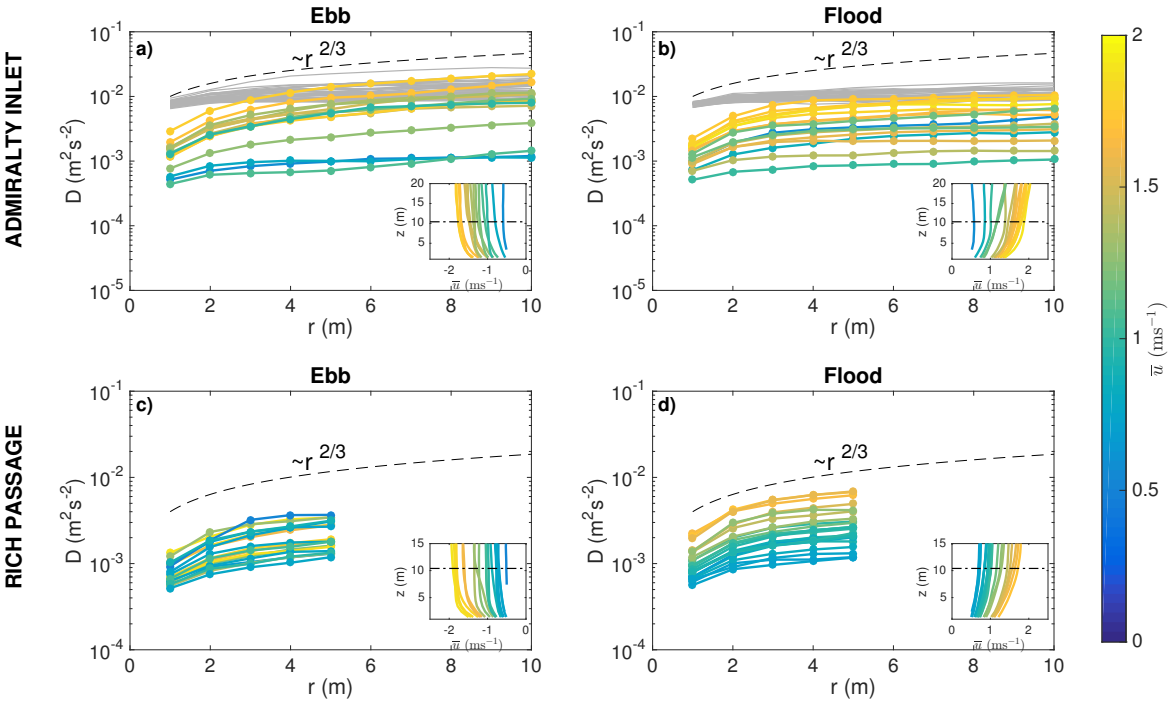


Figure 3.5: Spatial structure function at $z = 10.4$ m for different mean flows (by color): a), b) at Admiralty Inlet, and c), d) at Rich Passage. The dashed line is proportional to $r^{2/3}$. Inset plots show mean flow vertical profiles (also by color); the dot-dashed line corresponds to $z = 10.4$ m. In the Admiralty Inlet plots, structure functions from the RDI Sentinel V50 data are included as grey curves.

The structure function is multiplied by $r^{-2/3}$ to obtain a compensated structure function in the inertial subrange (Rusello and Cowen, 2011). The dissipation rate is estimated by solving $\overline{D(z,r)r^{-2/3}\big|_{r_1}^{r_2}} = C_v^2\varepsilon^{2/3}$, where $r_1$ to $r_2$ is the range with the slope closest to zero. Estimates are not calculated for depths with less than four points in the structure function. At Admiralty Inlet, the minimum $r$ range used in the estimates is 1 to 4 m and the maximum range is 1 to 10 m; at Rich Passage the minimum range is 1 to 4 m, and the maximum range is 1 to 7 m. Within the valid depths, the structure function is quality controlled to remove estimates with negative slope, resulting in a loss of 21% of valid structure functions

at Admiralty Inlet and 28% at Rich Passage, for which no dissipation estimate is available. Although this is a rather severe amount of quality control, it is less than that of other studies applying the structure function (McMillan et al., 2016; Thomson, 2012).

Uncertainties in TKE dissipation rates from the structure function fitting are calculated by propagating the uncertainty in the compensated structure function, such that:

$$\sigma_{\varepsilon_D} = \left(\frac{1}{Cv^2}\right)^{3/2} \frac{3}{2} \overline{D_{comp}}^{1/2} \sigma_{D_{comp}} \tag{3.5}$$

were $\sigma_{\varepsilon_D}$ is the uncertainty in the dissipation rate estimate, and $\sigma_{D_{comp}}$ is taken to be the variance of the compensated structure function in the range of bin separations used to estimate $\varepsilon$.

Figure 3.6 shows averaged vertical profiles of TKE dissipation rates, separated by ebb and flood tides, with their corresponding error estimates for both sites and compares the two methods. The TKE dissipation rate estimates from the two methods are in agreement, although the estimates from the structure function do not cover the entire measured profile due to the $r$ limitation. AD2CP TKE dissipation rate estimates are also in good agreement with estimates from ADV data, even at Rich Passage, where the TT ADV was located above the top of the profile measured by the Nortek Signature. Averaged uncertainties, expressed as percentage of the flood/ebb averaged TKE dissipation rates, present different patterns at each site. At Admiralty Inlet, uncertainties from the structure function range between 12%, closer to the bottom, to 22%, higher in the water column. At Rich Passage, uncertainties from the structure function method remain between 10 to 15% through the water column, while uncertainties from the TKE spectra method range between the 15%, closer to the bottom, and 25% higher in the water column.

## *3.4 Analysis: Turbulent Kinetic Energy Production Rate*

In a well-mixed environment, the buoyancy TKE sink term can be neglected, and the TKE is primarily produced by the mean flow shear. If horizontal shear is small, the TKE production can be approximated in terms of the Reynolds stresses and the velocity vertical gradients as:

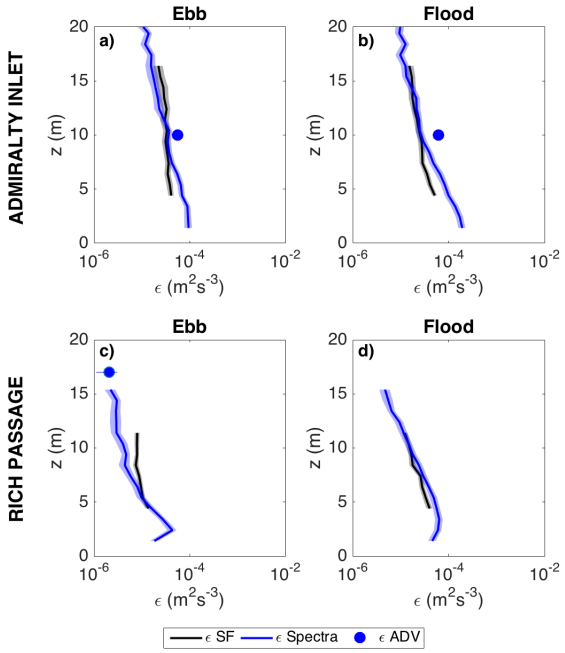


Figure 3.6: Average vertical profiles of TKE dissipation rate at: a), b) at Admiralty Inlet, and c), d) at Rich Passage. In blue from the TKE spectra and in black from the turbulence structure function. Blue dots correspond to TKE dissipation rate estimates from the TTM ADV spectra.

$$P = -\overline{u'_{ch}w'}\frac{\partial \overline{u_{ch}}}{\partial z} - \overline{v'_{ch}w'}\frac{\partial \overline{v_{ch}}}{\partial z} - \overline{w'w'}\frac{\partial \overline{w}}{\partial z} \tag{3.6}$$

where $P$ is the production of TKE, $u_{ch}$, $v_{ch}$ and $w$ are the along channel, across channel and vertical velocities respectively, and the primes denote velocity fluctuations.

### *3.4.1 Vertical Shear*

Along-beam velocities are transformed into orthogonal east-north-up components. The horizontal components are rotated to obtain along and across channel velocity components at each location. The vertical gradients of the along channel, across channel and vertical velocity, $\frac{\partial \overline{u_{ch}}}{\partial z}$, $\frac{\partial \overline{v_{ch}}}{\partial z}$, $\frac{\partial \overline{w}}{\partial z}$, are estimated as the centered difference of their burst-average using the

vertical distance between measurements.

The uncertainty in the shear estimations is calculated following Williams and Simpson (2004) method as:

$$\sigma_S^2 = \frac{\sigma_N^2}{M\Delta z^2 \sin^2 2\theta} \tag{3.7}$$

where $\sigma_N$ is the instrument inherent Doppler noise, $M$ is the number of samples used in the burst-averaged and $\theta$ is the beam inclination angle. This estimate corresponds to the minimum level of shear detection considering only instrument noise as a source of error in the measurements (Williams and Simpson, 2004). It has been previously reported that instrument noise from instrument softwares is usually biased low (Williams and Simpson, 2004; Thomson et al., 2012). In this study, the instrument noise is estimated from the spectral noise level, as it is considered to be white noise (i.e. has a constant horizontal spectra) (McMillan and Hay, 2017). The estimated ping-to-ping instrument noise levels from spectra are: $\sigma_N = 2.65$ cm/s for the Nortek Signature, and $\sigma_N = 5.39$ cm/s for the RDI Sentinel V50. Instrument noise reported by the instruments corresponding software for each deployment and empirically estimated noise are shown in Table 5.1.

### *3.4.2 Reynolds Stresses*

The Reynolds stress tensor is estimated following the methodology of (Dewey and Stringer, 2007) for a 5-beam ADCP configuration. This methodology extends the variance technique (Lu and Lueck, 1999; Stacey et al., 1999; Rippeth et al., 2003) to different ADCP beam configurations including expressions for the Reynolds stresses for non-zero tilt. The use of five beams allows for exact expressions for five of the Reynolds stresses, total TKE and anisotropy (Dewey and Stringer, 2007). This method assumes small angle approximations for pitch and roll, which were achieved in these deployments (mean pitch $\sim 2.3^\circ$ and mean roll $\sim 0.4^\circ$ at Admiralty Inlet, mean pitch $\sim 0.35^\circ$ and mean roll $\sim -1.19^\circ$ at Rich Passage). The Reynolds stresses from (Dewey and Stringer, 2007) are written in instrument coordinates

(assuming heading is equal to zero), thus the obtained stresses are rotated to along and across channel coordinates after the calculations.

The following equations, from (Dewey and Stringer, 2007), define the Reynolds stresses in instruments coordinates for any 5-beam ADCP, assuming small tilt angles approximation:

$$\begin{aligned}\overline{u'^2} = \frac{-1}{4\sin^6\theta\cos^2\theta}\{&-2\sin^4\theta\cos^2\theta(\overline{u_2'^2}+\overline{u_1'^2}-2\cos^2\theta\overline{u_5'^2}) \\ &+2\sin^5\theta\cos\theta\phi_3(\overline{u_2'^2}-\overline{u_1'^2})\}\end{aligned} \tag{3.8}$$

$$\begin{aligned}\overline{v'^2} = \frac{-1}{4\sin^6\theta\cos^2\theta}\{&-2\sin^4\theta\cos^2\theta(\overline{u_4'^2}+\overline{u_1'^3}-2\cos^2\theta\overline{u_5'^2})-2\sin^4\theta\cos^2\theta\phi_3(\overline{u_2'^2}-\overline{u_1'^2}) \\ &+2\sin^3\theta\cos^3\theta\phi_3(\overline{u_2'^2}-\overline{u_1'^2})-2\sin^5\theta\cos\theta\phi_2(\overline{u_4'^2}-\overline{u_3'^2})\}\end{aligned} \tag{3.9}$$

$$\begin{aligned}\overline{w'^2} = \frac{-1}{4\sin^6\theta\cos^2\theta}\{&-2\sin^5\theta\cos\theta\phi_3(\overline{u_2'^2}-\overline{u_1'^2}+2\sin^5\theta\cos\theta\phi_2(\overline{u_4'^2}-\overline{u_3'^2}) \\ &-4\sin^6\theta\cos^2\theta\overline{u_5'^2})\}\end{aligned} \tag{3.10}$$

$$\begin{aligned}\overline{u'w'} = \frac{-1}{4\sin^6\theta\cos^2\theta}\{&\sin^5\theta\cos\theta(\overline{u_2'^2}-\overline{u_1'^2})+2\sin^4\theta\cos^2\theta\phi_2(\overline{u_2'^2}+\overline{u_1'^2}) \\ &-4\sin^4\theta\cos^2\theta\phi_3\overline{u_5'^2}-4\sin^6\theta\cos^2\theta\phi_2\overline{u'v'}\}\end{aligned} \tag{3.11}$$

$$\begin{aligned}\overline{v'w'} = \frac{-1}{4\sin^6\theta\cos^2\theta}\{&\sin^5\theta\cos\theta(\overline{u_4'^2}-\overline{u_3'^2})-2\sin^4\theta\cos^2\theta\phi_2(\overline{u_4'^2}+\overline{u_3'^2}) \\ &+4\sin^4\theta\cos^2\theta\phi_3\overline{u_5'^2}+4\sin^6\theta\cos^2\theta\phi_3\overline{u'v'}\}\end{aligned} \tag{3.12}$$

where $\theta$ is the beam inclination angle (25° in these cases), $\phi_2$ and $\phi_3$ correspond to Dewey's pitch and roll respectively, and $\overline{u_i'^2}$ are the along-beam velocity fluctuation variances. For the Nortek Signature configuration: $\phi_2$ corresponds to negative roll, and $\phi_3$ to pitch, and $u_1 = u_{1Sig}$, $u_2 = u_{3Sig}$, $u_3 = u_{4Sig}$, and $u_4 = u_{2Sig}$. For the RDI Sentinel V50: $\phi_2$ corresponds to roll, and $\phi_3$ to pitch, and $u_1 = u_{2Sent}$, $u_2 = u_{1Sent}$, $u_3 = u_{4Sent}$, and $u_4 = u_{3Sent}$.

The Reynolds stress tensors are quality controlled to be a positive definite matrix. A total of 12% of the Reynolds stress tensors at Admiralty Inlet, and an 8% at Rich Passage, do not meet this requirement.

The uncertainty in the Reynolds stresses estimations is calculated following (Williams and Simpson, 2004) method as:

$$\sigma_{RS}^2 = \frac{\sigma_N^4}{M \sin^2 2\theta} \tag{3.13}$$

where $\sigma_N$ is the instrument noise, $M$ is the number of samples used in the averaging and $\theta$ is the beam inclination angle. This uncertainty estimate corresponds to the minimum level of Reynolds stress detection only considering instrument noise as for the estimation of shear uncertainty (Williams and Simpson, 2004). This uncertainty will be used in the estimation of TKE Production uncertainty.

A comparison between the obtained Reynolds stresses from the 5-beam profilers (after explicit noise removal) and from direct covariance with the TTM ADV at Admiralty Inlet are shown in the scatter plot of Figure 3.7. Blue and red dots are averages binned by $\overline{u'_{ch}w'}$ from the TTM ADV measurements. Despite large scatter in the comparison, the binned results from both instruments are in agreement at higher Reynolds stresses. The large differences might be explained by the separation of the instruments and by remaining noise in the Reynolds stress estimates.

Figures 3.8 and 3.9 show time series of vertical profiles of the five Reynolds stresses estimated following the Dewey and Stringer (2007) method at Admiralty Inlet and Rich Passage respectively. The horizontal Reynolds stresses ($\overline{u'^2_{ch}}$, $\overline{v'^2_{ch}}$) reach values that are an order of magnitude higher than the rest of the estimated Reynolds stresses at both sites. The magnitude of the Reynolds stresses are modulated by the tidal currents. At Admiralty Inlet, Reynolds stresses magnitudes increase as the horizontal speed increases, and the maximum values are observed during the observed ebb. At Rich Passage (Figure 3.9), the Reynolds stresses magnitude also increases with the horizontal speed. The highest Reynolds stresses are observed during the highest flood tidal current.

Figure 3.10 shows vertical profiles of the estimated vertical shear Reynolds stress ($\overline{u'_{ch}w'}$),

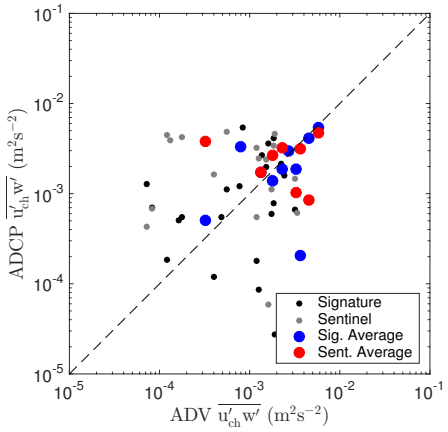


Figure 3.7: Vertical shear Reynolds stress ($\overline{u'_{ch}w'}$) at Admiralty Inlet: from TTM ADV data (x-axis), and from Nortek Signature and RDI Sentinel V50 estimated using Dewey and Stringer (2007) 5-beam method after noise removal (y-axis). Blue and red dots are averages binned by $\overline{u'_{ch}w'}$ from the TTM ADV measurements. Black-dashed line correspond to $y = x$. Averaged data correlation coefficients: 0.6 (Nortek Signature to TTM ADV), 0.05 (RDI Sentinel V50 to TTM ADV).

averaged for ebb and flood at the two sites together with ADV estimates when available. Additionally, estimates using the variance technique with no tilt corrections for the two 5-beam Acoustic Doppler Current Profilers at both sites are included.

At Admiralty Inlet, during ebb, averaged estimates from the two instruments are in good agreement, and are also in good agreement with the TTM ADV estimates. For the first 15 m of the water column, the estimates from the Nortek Signature are higher than those from the RDI Sentinel V50. During flood, the RDI Sentinel V50 estimates are higher than those from the Nortek Signature through the entire water column. During ebb, the estimates from the variance technique are biased low during the lower portion of the water column and they are higher during the second portion of it. During flood, the variance technique estimates remain lower for most of the water column. This difference highlights the importance of the tilt corrections incorporated in the new calculations of the Reynolds stresses as previously reported by Lu and Lueck (1999).

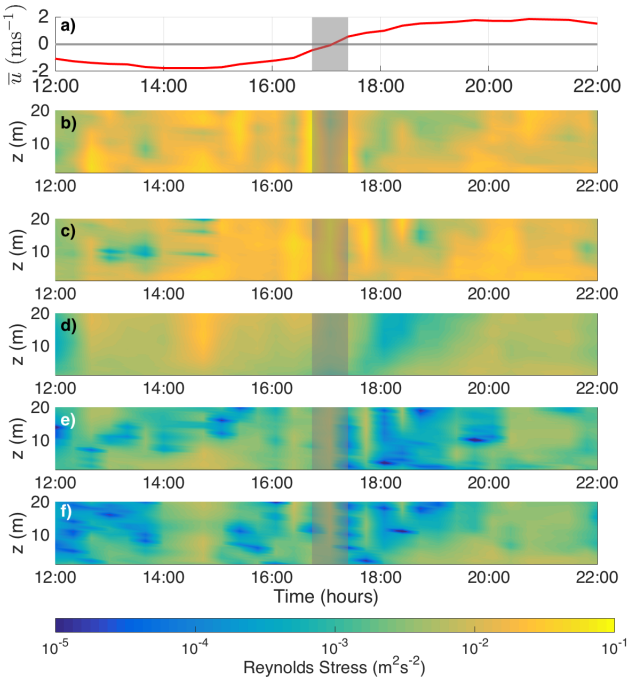


Figure 3.8: Horizontal burst-averaged speed and vertical profiles of Reynolds stresses in time estimated using Dewey and Stringer (2007) 5-beam method at Admiralty Inlet: a) Mean flow, b) $\overline{u'^2_{ch}}$, c) $\overline{v'^2_{ch}}$, d) $\overline{w'^2}$, e) $\overline{u'_{ch}w'}$ , and f) $\overline{v'_{ch}w'}$. Slack conditions are marked in grey.

At Rich Passage the two methods are in good agreement, with slightly lower estimates from the variance technique through the water column. However, the average estimate from the TT ADV at this site is much higher, which might be explained by motion contamination at low frequencies in $u'_{ch}$ (Kilcher et al., 2017).

### *3.4.3 Vertical shear TKE Production*

The estimated Reynolds stresses together with the vertical shear are used to estimate the vertical shear TKE production rate. The uncertainty in the TKE production estimations is calculated following Williams and Simpson (2004) method, which is based in the variance of

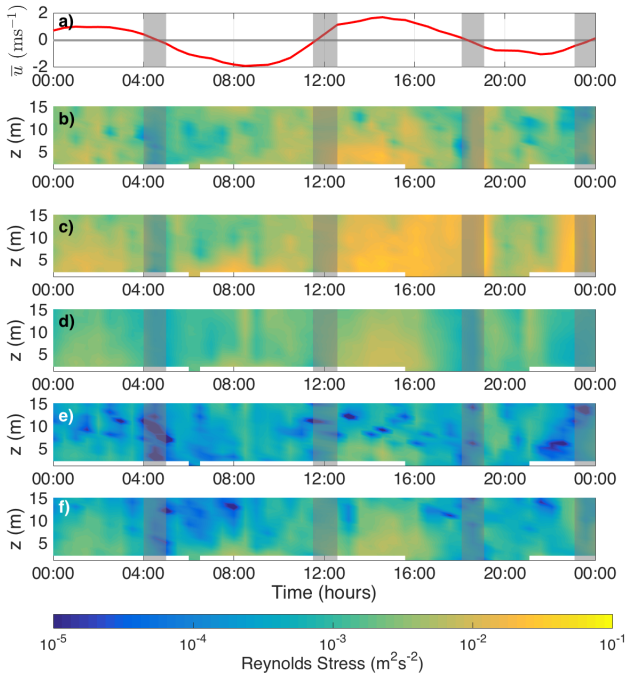


Figure 3.9: Horizontal burst-averaged speed and vertical profiles of Reynolds stresses in time estimated using (Dewey and Stringer, 2007) 5-beam method at Rich Passage: a) Mean flow, b) $\overline{u'^2_{ch}}$, c) $\overline{v'^2_{ch}}$, d) $\overline{w'^2}$, e) $\overline{u'_{ch}w'}$ , and f) $\overline{v'_{ch}w'}$. Slack conditions are marked in grey.

the product of two variables:

$$\sigma^2_{P_{ij}} = \overline{u'_i u'_j}^2 \sigma^2_S + \frac{\partial \overline{u_i}}{\partial x_j} \sigma^2_{RS} + \sigma^2_S \sigma^2_{RS} \tag{3.14}$$

where $\sigma_{P_{ij}}$ is the uncertainty associated with the TKE production generated by the Reynolds stress $\overline{u'_i u'_j}$ and the shear $\frac{\partial \overline{u_i}}{\partial x_j}$. Then the uncertainty of the vertical shear production $P$ (Eq. 3.6) is estimated as:

$$\sigma_P = \sqrt{\sigma^2_{P_{u_{ch}w}} + \sigma^2_{P_{v_{ch}w}} + \sigma^2_{P_{ww}}} \tag{3.15}$$

Figure 3.12 shows averaged vertical profiles of TKE production for both sites separated by ebb and flood tides and their respective uncertainty. In these plots, TKE production decreases with $z$, as expected for bottom-generated turbulence. The uncertainty in the TKE

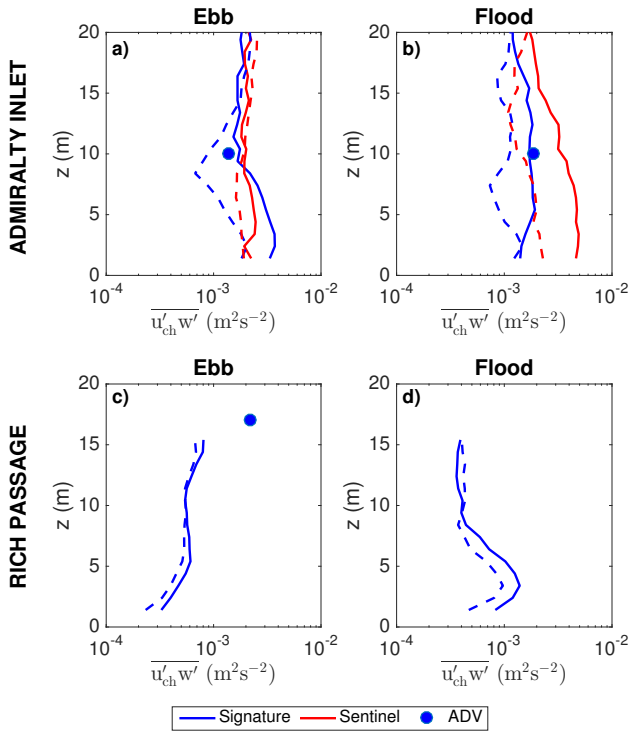


Figure 3.10: Average vertical shear Reynolds stress ($\overline{u'_{ch}w'}$) profiles estimated using Dewey and Stringer (2007) 5-beam method at: a), b) at Admiralty Inlet, and c), d) at Rich Passage. In blue from the Nortek Signature data, in red from the RDI Sentinel V50 data. Dashed lines correspond to estimates using the original variance technique with no tilt corrections (Stacey et al., 1999). Blue dots correspond to estimates from the ADV data.

production increases with $z$, because $\sigma_{P_{\overline{ww}}}$, which is the dominating term in the production uncertainty, increases with $z$. The $\sigma_{P_{\overline{ww}}}$ uncertainty is dominated by its first term, $\overline{w'w'}\sigma_S^2$, which increases with $z$ as would be expected as vertical fluctuations grow towards the mid water column, as the distance from the boundary increases. At Admiralty Inlet, TKE production uncertainties range from 2% closer to the bottom, up to 90% at the top of the measured profile during ebb (26% maximum uncertainty during flood). At Rich Passage, uncertainties range from 6% closer to the bottom, up to 90% at the top of the measured profile.

### *3.5 Application: Turbulent Kinetic Energy Balance*

The analysis of the turbulent kinetic energy balance from field measurements usually assumes that TKE production balances TKE dissipation. The inclusion of the 5th beam in these new Acoustic Current Doppler Profilers allows for an improved estimation of TKE production; hence, a better closure of the TKE balance is possible. This improved TKE balance might indicate that other terms in the TKE balance, such as the TKE transport, are of importance, and it can be used to improve turbulence closure models in these environments.

Assuming that the buoyancy term is negligible at these well-mixed sites and that self-advection is small, the rate of change of TKE can be approximated as a local production-dissipation balance,

$$\frac{D}{Dt}(TKE) \approx P - \varepsilon \tag{3.16}$$

Figure 3.11 shows the burst-averaged horizontal speed and vertical profiles in time of total TKE, TKE dissipation rate (from spectra), and TKE vertical production from the Nortek Signature data at both sites. At Admiralty Inlet, all three variables seem to be modulated by the stage of the tidal current, increasing as the velocity magnitude increases, however larger TKE, and TKE dissipation and production rates are observed during ebb. A similar pattern is observed at Rich Passage, where the variables are also modulated by the tidal currents, but larger values observed during the stronger flood.

Figure 3.12 shows an approximate TKE budget as depth profiles of vertical shear TKE production and TKE dissipation rates from the Nortek Signature data. Rates are averaged over all burst-average horizontal speeds, for ebb and flood at each site. The expected balance is generally found, however there are distinct patterns that likely are related to the lateral headland at Admiralty Inlet and the vertical sill at Rich Passage.

During ebb at Admiralty Inlet, TKE production exceeds dissipation closer to the bottom and then an approximate balance is observed above $z = 10.4$ m. During flood, production and dissipation are approximately balance up to $z = 15.4$ m, and production exceeds dissi-

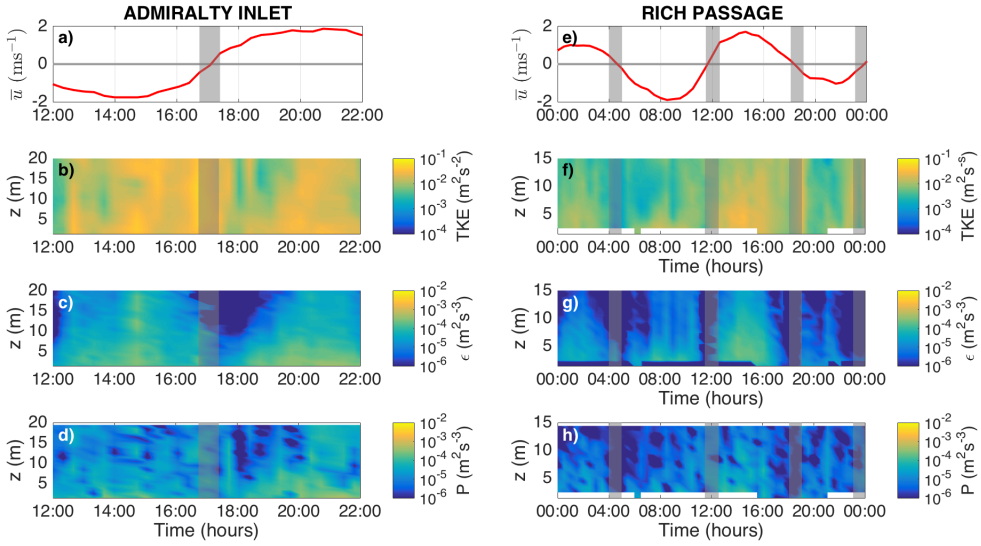


Figure 3.11: Vertical profiles of TKE dissipation and production rates in time at Admiralty Inlet (left) and at Rich Passage (right). Panels show: a) and e) Mean horizontal speed, b) and f) Total TKE, c) and g) TKE dissipation rate, d) and h) TKE production rate.

pation in the higher portion of the water column. At Rich Passage, production is balanced by dissipation for most of the water column during ebb, except below $z = 5.4$ m, where dissipation exceeds production. During flood, dissipation exceeds production through the entire profile.

Figure 3.13 shows scatter plots of TKE production versus TKE dissipation rates for all burst-average velocities and all depths. The values are well correlated over several orders of magnitude, albeit with significant scatter. At Admiralty Inlet, a near 1:1 balance between TKE production and TKE dissipation during the most energetic conditions is observed. During less energetic conditions, TKE production exceeds TKE dissipation, suggesting that the transport of turbulent kinetic energy is of importance during such conditions. At Rich Passage, a near 1:1 balance between TKE production and TKE dissipation is observed during all conditions.

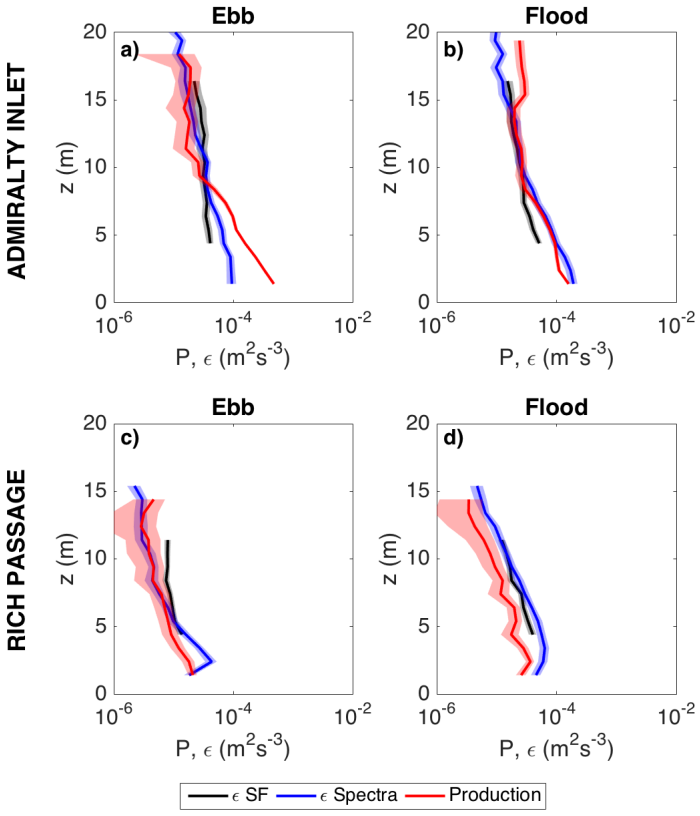


Figure 3.12: An approximate TKE budget shown using average TKE dissipation rates from the two methods and TKE shear production from Reynolds stresses from the Nortek Signature data: a), b) at Admiralty Inlet, and c), d) at Rich Passage.

## *3.6 Conclusions*

Two new 5-beam acoustic current profilers, the Nortek Signature 1000 (KHz) AD2CP and the RDI Sentinel V50 are successfully used to measure turbulence at two energetic tidal channels: Admiralty Inlet and Rich Passage (Puget Sound, WA, U.S.A). Turbulent kinetic energy (TKE) production and dissipation rates are estimated from the measurements, and an approximate TKE budget is obtained.

The results illustrate the capabilities of 5-beam profilers for assessing high order turbulence parameters. The TKE frequency spectra from the Nortek Signature presents a low

noise level, of $\mathcal{O}(10^{-4})$ $m^2s^{-2}$, while the RDI Sentinel V50 presents a higher noise level of $\mathcal{O}(10^{-2})$ $m^2s^{-2}$ that is comparable to the previous generation of profilers.

The lower noise observed on the Nortek Signature spectra might be attributed to its ability to sample faster (8 Hz when using all 5 beams), however when subsampling the Nortek Signature data to 2 Hz (the maximum possible with the RDI), the noise level in the TKE spectra remains of $\mathcal{O}(10^{-4})$ $m^2s^{-2}$. The TKE spectra obtained with the Nortek Signature are in agreement with spectra from ADV measurements at both sites.

The lower noise level of the Nortek Signature enables observation of the inertial subrange of turbulence, and thus improved estimations of the TKE dissipation rate from both, TKE spectra and second order structure function of turbulence. TKE dissipation rates from the two methods agree well with each other through the water column, and also with estimates from ADV data.

Although the TKE spectra from the RDI Sentinel V50 does not allow the observation of the inertial subrange, the lower frequency portion of the spectra is well-resolved and in agreement with the estimates from the Nortek Signature and from the Nortek Vector. The RDI Sentinel V50 data can be used to estimate a synthetic vertical TKE spectra using the non-dimensional Kaimal curves (Kaimal et al., 1972). These curves can be fit to the lower portion of the TKE spectra and then used to extend the inertial subrange, and subsequently estimate the TKE dissipation rate. However, the derivation of the Kaimal curves is based on a balance between TKE production and dissipation, thus their application might only be appropriate at all depths were an approximate Production - Dissipation balance is observed in the studied sites (Walter et al., 2011).

The use of all five beams enables the direct estimation of five out of six of the Reynolds stresses, which allows for improved estimations of the TKE production rate and provides better information for developing and validating turbulence closure models. The new Reynolds stresses calculations include tilt corrections following the Dewey and Stringer (2007) method. At Admiralty Inlet, Reynolds stresses estimates from the two profiling instruments are in agreement with estimates from ADV at higher Reynolds stresses. The small differences

may be attributed to instrument separation and to remaining noise in the Reynolds stresses estimations.

The TKE dissipation rates and TKE production rates are used to analyze an approximate TKE budget at Admiralty Inlet and at Rich Passage. In general, the expected balance is observed, however, distinct patterns are observed at the two sites, which are thought to be related to bathymetric features that promote TKE advection and transport.

The most recent version of the Nortek Signature 1000 includes an integrated motion unit, which enables instrument motion corrections, such that the instrument can also be mounted in buoys and/or moorings. The new firmware version of the Nortek Signature supports High-Resolution (HR) measurements, enabling high-sampling frequency measurements in velocity bins small as 0.02 m. The low Doppler noise of the Nortek Signature, similar to ADV noise levels, makes it even suitable for lower turbulence environments. ADVs have been successfully used to estimate TKE dissipation rates from TKE spectra in low turbulence environment such as lakes in Brand et al. (2008) and in Vachon et al. (2010).

The turbulence parameters that can be obtained with these new instruments are useful for the development and improvement of turbulence models, for the study of mixing processes, and for predicting sediment transport. The methods presented in this paper are implemented in Matlab and are available through the Matlab File Exchange website as 5-Beam Acoustic Doppler Current Profiler Turbulence Methods: `http://www.mathworks.com/matlabcentral/fileexchange/57551-mguerrap-5beam-turbulence-methods`

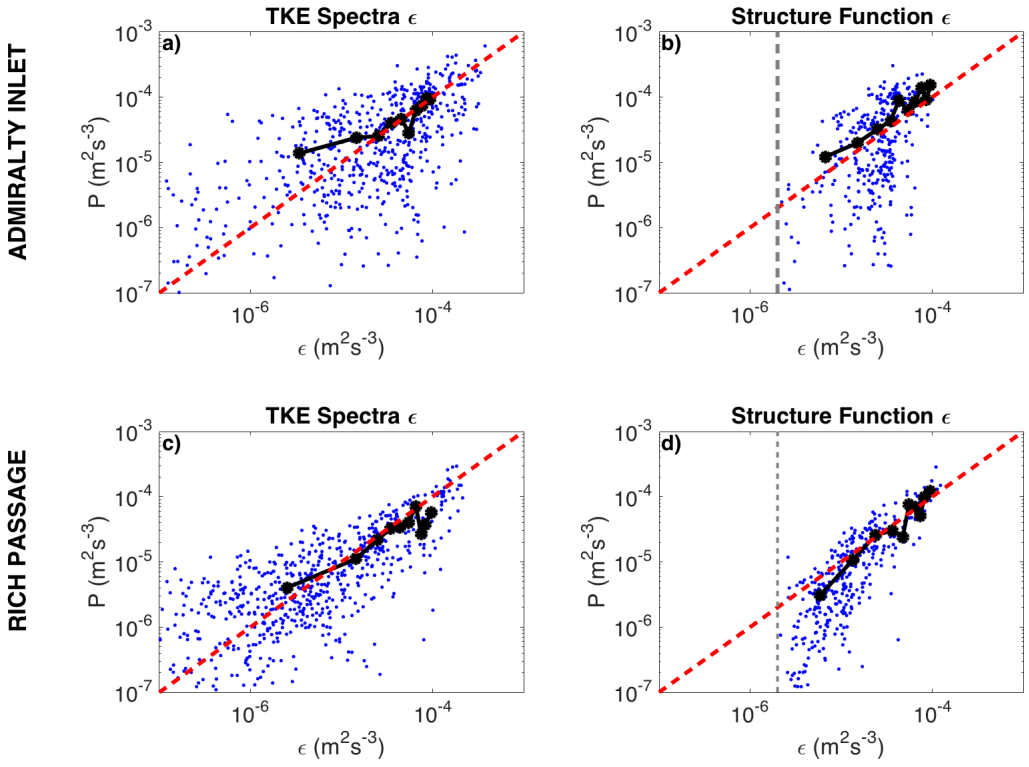


Figure 3.13: TKE Dissipation Rate and TKE Production for all $\bar{u}$ and all depths: a), b) at Admiralty Inlet and b), c) at Rich Passage. Black dots represent mean values of dissipation and production binned by dissipation. Red dashed line corresponds to $y = x$. In the plots showing the TKE dissipation rate from the structure function, the dashed grey line represents the limit of TKE dissipation detection when using the turbulence structure function.

# Chapter 4

# LONG-TERM OBSERVATIONS OF TIDAL CURRENTS THROUGH ADMIRALTY INLET FROM FERRY-MOUNTED ADCPS

## *4.1 Introduction*

### *4.1.1 Ferry-based observations*

Previous research projects have demonstrated the utility of ferry-based measurements in the collection of oceanographic data (Merckelbach, 2006; Codiga and Nehra, 2012; Balfour et al., 2012; Petersen, 2014; Nauw et al., 2014; Zhu et al., 2017; Liu et al., 2017). The FerryBox systems have been widely used in ferry lines and commercial vessels in Europe since 2003 (Petersen, 2014). These automated systems measure a range of oceanographic parameters, such as temperature, salinity, turbidity and chlorophyll-*a*. Some FerryBox systems are integrated with acoustic Doppler current profilers (ADCPs) to measure flow velocities, and with a variety of sensors for measuring pH, disolved oxygen, and nutrients (Petersen, 2014). Data from the FerryBox systems has a broad range of applications: from the study of algal blooms to the validation of remote sensing measurements of ocean surface properties (Petersen, 2014). Recently, acoustic Doppler current profilers have been mounted on board ferry systems covering long transects ($\mathcal{O}(1000)$ km), measuring flow velocities through the water column. Continuous ferry-based measurements along the eastern edge of the East China Sea provided up to 8 tidal harmonic constituents in Liu et al. (2017), and data from the same ferry-system was successfully used to estimate residual currents from the north-west Pacific Ocean into the East China Sea in Zhu et al. (2017). Acoustic backscatter data from ferry-mounted ADCPs has been used to estimate suspended sediment concentrations across the Marsdiep inlet ( 3 km wide) in The Netherlands in Merckelbach (2006) and Nauw et al.

(2014).

Within the US, the Ferry-based Observations for Science Targeting Estuarine Research - Long Island Sound (FOSTER-LIS) project collects data between the east end of the Long Island Sound between Bridgeport, CT, and Port Jefferson, NY. This is where most of the exchange flow occurs in the region, which is measured using instruments installed on board MV John H. ferry, operated by Cross Sound Ferries, Inc. (Codiga, 2007; Codiga and Nehra, 2012). The project provides measurements of currents from a vessel-mounted ADCP to quantify both the exchange flow and the surface water quality parameters, such as temperature, conductivity, salinity and Chlorophyll-*a*. All collected data is post-processed for quality control, gridded within the cross-section of the LIS, and available online for research purposes (Codiga, 2007; Codiga and Nehra, 2012). In a similar project, the Washington State Department of Ecology (WSDOE) has taken advantage of these so called vessels-of-opportunity by installing water quality sensors on board the Victoria Clipper ferry which runs from Seattle, WA, to Victoria, B.C, passing trough Admiralty Inlet. These measurements are complimented by vessel-mounted ADCPs on Washington State Ferries crossing Admiralty Inlet from Port Townsend, WA to Coupeville, WA.

### *4.1.2 Admiralty Inlet site description*

Puget Sound is a estuarine system located in the northwest of the USA (47.85°N - 122.43° W). The main connection between Puget Sound and the Strait of Juan de Fuca (thus the Pacific Ocean) is through Admiralty Inlet, a narrow sill located in the northern part of Puget Sound (48.14°N - 122.71° W) (Sutherland et al., 2011).

Admiralty Inlet is a highly energetic constriction, where fast tidal currents are observed and strong tidal mixing occurs. Previous measurements of tidal currents and turbulence at Admiralty Inlet, from fixed bottom-mounted instruments, indicate that maximum velocities are above 3 $ms^{-1}$ mid-channel and faster flows occur near Admiralty Head (northeast), where turbulence intensity is about 10% (Polagye and Thomson, 2013; Thomson et al., 2012). Estuarine circulation patterns have been observed at different locations across Admiralty Inlet

from long-term fixed bottom-mounted measurements of velocities, with maximum residual velocities reaching up to 0.4 $ms^{-1}$ (Deppe et al., 2018; Polagye and Thomson, 2013). Seasonal variations of these residual currents are mainly related to freshwater inputs and tidal phase (Deppe et al., 2018), and are associated with low-oxygen ocean water intrusions into Puget Sound, impacting water-quality and marine life through the estuary. Deppe et al. (2018) showed that these low-oxygen ocean water intrusions occur under minimal tidal mixing conditions and maximum diurnal inequalities at Admiralty Inlet (i.e. low turbulence and high exchange flow conditions). In addition, Admiralty Inlet experiences high ship traffic, and has been recognized as a prominent site for tidal energy extraction due to its strong tidal currents.

As a compliment to high temporal resolution measurements at single locations across the inlet, long-term measurements of high spatial resolution spanning the entire inlet are crucial for understanding circulation through Puget sound, improving navigation safety, and for tidal energy resource characterization.

Although the instrumentation and capabilities exist, the use of multiple moored instruments does not provide enough spatial resolution, and can become cost-prohibitive, as instruments need to be frequently recovered and redeployed for data retrieval and changing batteries. Continuous measurements from vessel mounted instruments provide the spatial resolution needed, but the use of a dedicated research vessels for long periods of time can become cumbersome and impractically expensive. In this context, commercial vessels that sail the same route for extended periods of time pose an excellent cost-effective platform to obtain long time series of oceanographic variables across a large domain (Petersen, 2014; Balfour et al., 2012). Such is the case of the Washington State Department of Transportation (WSDOT) Ferries, which run year round through the basins of Puget Sound.

The WSDOE and WSDOT have partnered with the University of Washington Applied Physics Laboratory to implement and maintain a Ferry-Based Monitoring System of Puget Sound Currents. The aim of the project is to determine the exchange of water between Puget Sound and the Strait of Juan de Fuca, in order to improve and calibrate water quality models

through Puget Sound. ADCPs have been installed on board the MV Kennewick and MV Salish ferries, and these continuously collect water velocities across Admiralty Inlet during the multiple daily runs of the ferries.

This paper presents flow velocity observations across Admiralty Inlet collected from the ferry-mounted ADCPs. Data from the first four years of operations (2014-2017) are analyzed to obtain the harmonic constituents of tidal currents through the inlet, and first steps are taken to estimate residual currents from the data. Data collection details are given in section 4.2, data quality control and organization are presented in section 4.3. Section 4.4 presents the data analysis and results, including tidal currents harmonic analysis and rough estimations of residual currents. Finally, conclusions are presented in section 4.5.

## *4.2 Data Collection*

### *4.2.1 Ferry routes and ADCP settings*

Admiralty Inlet is 6 km wide with large bathymetric gradients in the across-channel direction. Figure 4.1 shows the location of the inlet within Puget Sound, and a detailed map of the Admiralty Inlet area colored by bathymetry, including the Port Townsend - Coupeville ferry route. The maximum depth along the ferry route is approximately 120 m.

Two down-looking Acoustic Doppler Current Profilers (ADCPs) were installed on board MV Kennewick and MV Salish WSDOT ferries, which cross Admiralty Inlet between Port-Townsend and Coupeville about twelve times a day. The instruments were installed using a through-hull mount filled with fresh water and capped with a transparent polycarbonate window.

The ADCPs, both 300 kHz RDI Workhorse Monitors, provide full depth profiles of velocities in earth coordinates across the inlet since May 2014 (measurements are ongoing). For each ADCP there are 60 bins of 2 m each, starting with a 2 m blanking distance from the instrument. The ADCPs are set to measure relative water velocities, bottom distance, and bottom-tracking velocities, which are later used to reconstruct true water velocities. Navi-

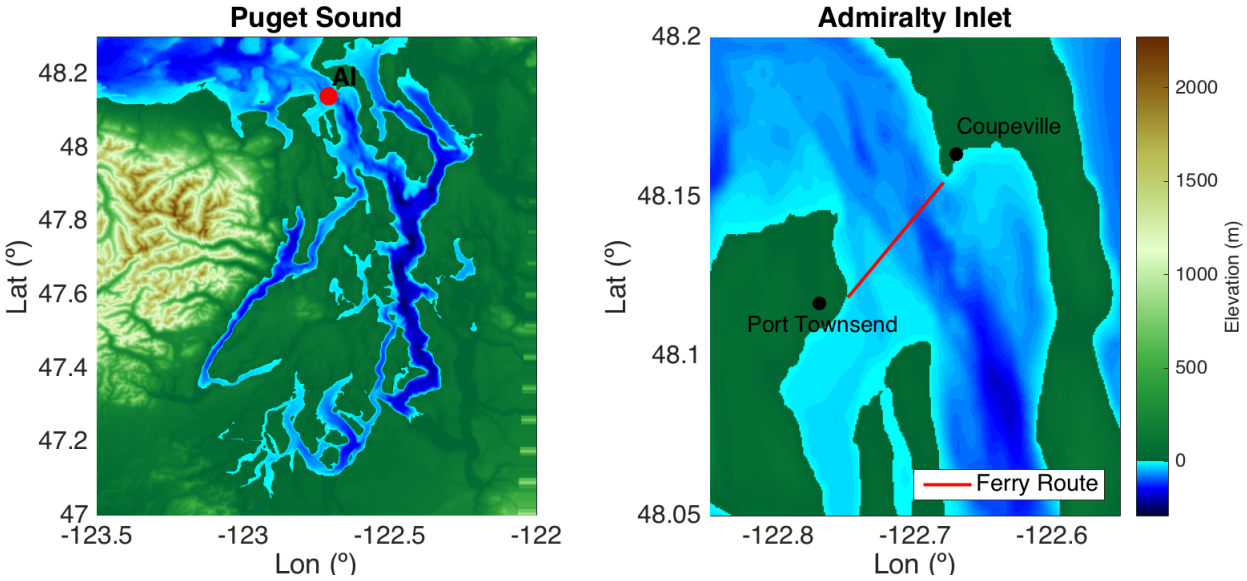


Figure 4.1: Map of Puget Sound Admiralty Inlet colored by topo-bathymetry. Red line represents Port Towsend - Coupeville ferry route.

gation velocities from the ferry's GPS, are also available for data analysis. Data is sampled at 2 Hz, and short time ensembles are calculated every 15 s. Both ferries run during the summer; only one of them runs the Admiralty Inlet route the rest of the year. Which one is running the route depends on other WSDOT Ferry schedules.

Data collection is continuous while the vessels are operational. All raw data collected from the ADCPs is stored locally on board the ferries. Short time ensembles (15 s) are uploaded daily to a public server and are available for download on the project website[1]. Available data includes full vertical profiles of velocity, bottom-track distance and velocity, navigation velocity, and ancillary ADCP data (including data necessary for data quality control). In addition, bathymetry information from a Puget Sound Digital Elevation Model (NAVD88 datum) and tidal elevation predictions are also included for each ADCP measurement location and time. Figure 4.2 shows the spatial distribution of all vertical profiles of velocity

[1]http://www.apl.washington.edu/ferriesforscience

collected by both ferry-mounted ADCPs through Admiralty Inlet (colored by depth). As seen in this map, there is significant scatter in the data location, since the ferry does not take the exact same route at every crossing.

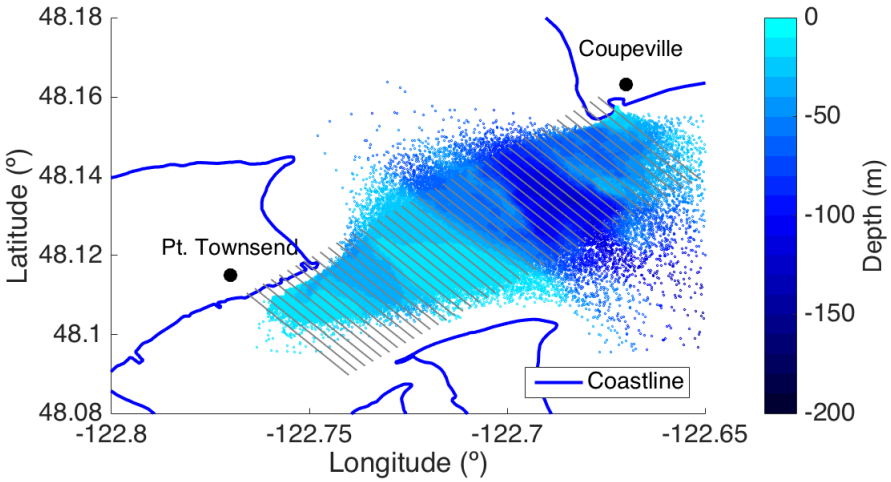


Figure 4.2: Location of ferry-mounted ADCPs measurements colored by depth. Grey lines correspond to the along-channel edges of the data organization grid.

### *4.2.2 Additional data-sets*

Two additional data sets are used to test the accuracy of the data collected by the ferry ADCPs. These data sets provide flow velocities from fixed bottom-mounted ADCPs at several locations through Admiralty Inlet, with deployments lasting up to 3 months.

The first data set, from the Pacific Marine Energy Center (PMEC), includes data from different deployments at selected locations across Admiralty Inlet aimed at characterizing its available tidal energy resource. These deployments were concentrated near Admiralty Head (north-east side of Admiralty). Five deployments are selected for comparison, whose

Table 4.1: Additional deployments and sampling parameters at Admiralty Inlet

| Institution | PMEC | | | | | NOAA | | | |
|---|---|---|---|---|---|---|---|---|---|
| Instrument | RDI Workhorse 300 kHz | | | Nortek AWAC 600 kHz | | RDI Workhorse 300 kHz | | | |
| Station | SS03a | SS01a | SS01b | SS03b | SS01c | PUG1619 | PUG1620 | PUG 1623 | PUG1624 |
| Lat (°) | 48.1521 | 48.1509 | 48.1477 | 48.1515 | 48.1486 | 48.1063 | 48.1193 | 48.1501 | 48.1569 |
| Lon (°) | -122.6954 | -122.6877 | -122.6903 | -122.6738 | -122.7221 | -122.6725 | -122.6623 | -122.7454 | -122.7260 |
| Deployment | 4/9/09 | 5/20/09 | 11/12/09 | 11/10/10 | 2/13/11 | 6/18/16 | 6/19/16 | 6/19/16 | 6/21/16 |
| Recovery | 5/19/09 | 8/3/09 | 1/29/10 | 2/10/11 | 5/9/11 | 8/21/16 | 8/20/16 | 8/21/16 | 8/21/16 |
| Ensembles (s) | 600 | 30 | 45 | 60 | 60 | 600 | 600 | 600 | 600 |
| Depth (m) | | | | | | 64.1 | 101 | 61.9 | 66.5 |
| Nbins | 61 | 51 | 59 | 40 | 40 | 48 | 28 | 46 | 48 |
| First Bin (m) | 4.6 | 3.6 | 3.6 | 1.2 | 1.2 | 10.2 | 39.2 | 12.8 | 14.1 |
| Top Bin (m) | 64.6 | 53.6 | 61.6 | 40.2 | 40.2 | 57.2 | 66.2 | 57.8 | 61.1 |
| $\Delta$ z (m) | 1 | 1 | 1 | 1 | 1 | 1 | 1 | 1 | 1 |

locations coincide with the ferry crossings. The second data set, from NOAA's Center for Operational Oceanographic Products (CO-OPS), includes velocity data from four ADCPs deployed in the vicinity of Admiralty Inlet in the summer of 2016. These deployments were part of NOAA CO-OPS effort to survey Puget Sound currents in order to update tidal current predictions, and to support future hydrodynamic models of the area. A summary of these deployment details is presented in Table 4.1.

In addition, ferry data will also be compared with data from the National Renewable Energy Laboratory Tidal Energy Atlas (Haas et al., 2011; Sutherland et al., 2011). This data set provides tidal currents harmonics (8) from depth-averaged flow velocities estimated from a ROMS numerical model of the area at a 350 m resolution in average (Haas et al., 2011; Sutherland et al., 2011).

## *4.3 Data Processing*

### *4.3.1 Quality Control*

All velocity data captured by the ferry ADCPs is processed in order to remove low quality measurements. Data that does not meet the quality standards is removed from the set and it is not considered in the subsequent analysis. The following criteria are applied to the entire ferry-based data set:

- Bottom-track return from at least two (out of four) ADCP beams is necessary, any less results in removal of the entire velocity profile.
- Remove any data collected deeper than the bottom-track return of each velocity profile
- Remove first 5 bins of data due to acoustic interference (ringing and bubbles) near ferry hull (Nauw et al., 2014)
- Set the following thresholds:
  - Minimum Correlation: 35, established using spurious directions of tidal currents
  - Absolute velocity: 7 m/s, established using the ambiguity velocity of the original ADCP settings
  - Error velocity (vertical): 1 m/s, established empirically
  - Maximum true water velocity magnitude: 4 m/s

The application of these strict quality controls removes more than half of the measured velocity profiles. Some of the causes of low quality measurements are: i) ferry propeller bubbles interfere with ADCP measurements during every other crossing; ii) marine growth accumulates on the ADCP glass window, though it is regularly cleared and coated with zinc oxide to inhibit biofouling; and iii) vessel speeds sometimes exceed the absolute velocity threshold, especially when they take longer routes due to conflicting vessel traffic.

The accuracy of bottom-track distance and bottom-track velocities is tested by comparing them to the Puget Sound DEM (corrected for tidal elevation) and to the GPS based vessel navigation speed, respectively. Figure 4.3 shows scatter plots of both quantities, showing an excellent agreement between the different data sets. For the bottom-track distance, the best fit slope is 0.98 with a 1.57 m intercept, while for the ferry speed the best fit slope is 1.03 with a -0.06 $ms^{-1}$ intercept. Note that these plots only consider data that passed the quality control process.

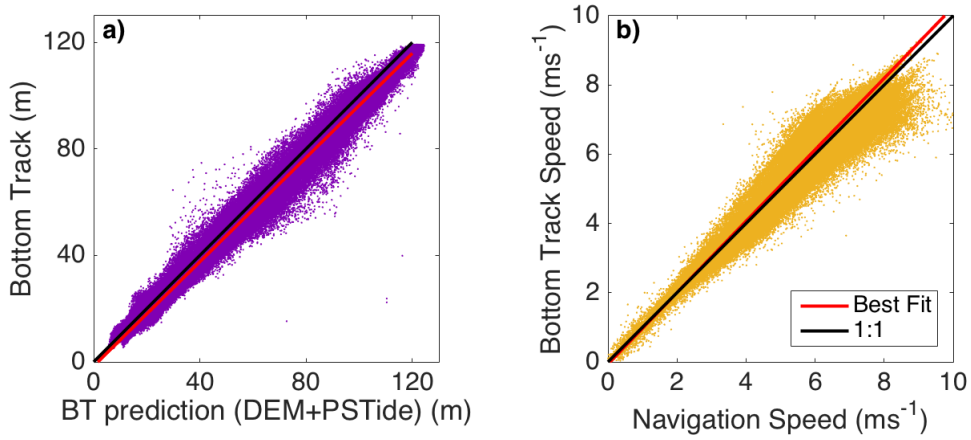


Figure 4.3: a) Puget Sound DEM corrected by tidal elevation (x-axis) vs. ADCP bottom-track distance (y-axis), and b) GPS ferry navigation velocities (x-axis) vs. ADCP bottom-track velocity (y-axis). Red lines correspond to data best-fit, and in black is the 1:1 line.

### *4.3.2 Spatial gridding and generation of time-series*

Quality controlled data are organized in a horizontal and vertical grid across the inlet, which accounts for spatial variability between ferry crossings and tidal elevation changes, respectively. The inlet is gridded into 44 cells each 200 m in the across channel direction, and into 2 m vertical cells (within each horizontal cell). Note that each horizontal grid is 3 km in the along-channel direction. The horizontal grid begins south of Port Townsend (adding 2 km to the width of the inlet) and ends south of Coupeville (see Figure 4.2). The GPS

horizontal location of each measurement is used to map the full velocity profiles into the grid. The vertical grid zero coincides with the NAVD88 datum zero at this location (Puget Sound DEM datum). ADCP's vertical bin locations are referenced to NAVD88 datum using the tidal elevation prediction (referenced to NAVD88 too) at each measuring time.

Finally, data within each grid cell constitutes a non-uniform time series of horizontal velocities across Admiralty Inlet at different depths. Figure 4.4 shows a time series example of along-channel velocity from a grid-cell located-mid channel, about 20 m below the free-surface. In this figure, the gaps in data correspond to low quality measurements. Here, the tidally modulated behavior of currents is also observed.

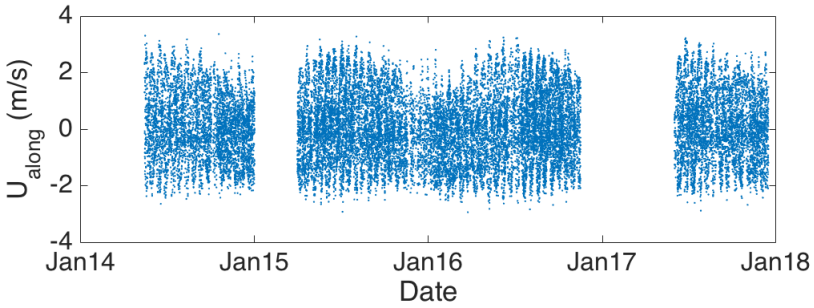


Figure 4.4: Example of a non-uniform time series of along-channel velocity from ferry-based measurements within a single grid cell.

### *4.3.3 Sample Bias Test*

The ferries that cross Admiralty Inlet run only during the day, so there are no ADCP measurements during the night, and two ships cover the inlet during the summer, resulting in more measurements during summer time than during the rest of the seasons. A consequence of this change in schedule is sample bias, in which some tidal stage can be preferentially measured. For example more measurements can occur during low tides than during high tides (or the opposite), and more samples can occur during ebbs than during flood currents. Here, sample bias is tested using the valid gridded data time-stamps.

To test the sample bias at each grid cell, tidal elevation and tidal currents are reconstructed at the time stamps of valid measurements within each grid cell using harmonic analysis. Harmonic constituents for tidal elevation and tidal currents obtained from one of the NOAA ADCPs (PUG1624) are used for the reconstruction. In addition, uniform time series ($\Delta t$ = 10 min) of tidal elevation and tidal currents are reconstructed for the same period of time covered by the valid time stamps. These uniform time series represent what would have been measured by a fixed platform ADCP at the grid location. Following the reconstruction, the probability distributions of the reconstructed tidal elevation and tidal currents are estimated, and compared with the distribution from the uniformly sampled time series.

This testing method is preferred, since no tidal elevation data is collected by the ferry ADCPs. Furthermore, water velocities from the ferry ADCPs have uncertainties from instrument Doppler noise and from the griding process that can influence the distribution of the sampled tidal stages.

Figure 4.5 shows the estimated probability distributions at one grid cell. Although the distributions from the ferry samples have some noise, there is no significant sample bias in the ferry measurements times when compared to uniformly sampled data. The same behavior is observed in all the tested grid cells. The probability skewness for low tide, around -2 m, is also observed in the distributions of free-surface elevation measured by the additional bottom-fixed ADCPs included in this study (see Table 4.1), and is explained by the mixed semi-diurnal tidal regime of Admiralty Inlet.

## *4.4 Data Analysis*

### *4.4.1 Tidal Currents Harmonic Analysis*

Tides dominate the circulation signal at Admiralty Inlet, thus the first application of the clean and organized data set is to capture the tidal harmonic constituents of the currents. Harmonic analysis of binned, non-uniform time series of horizontal currents is performed

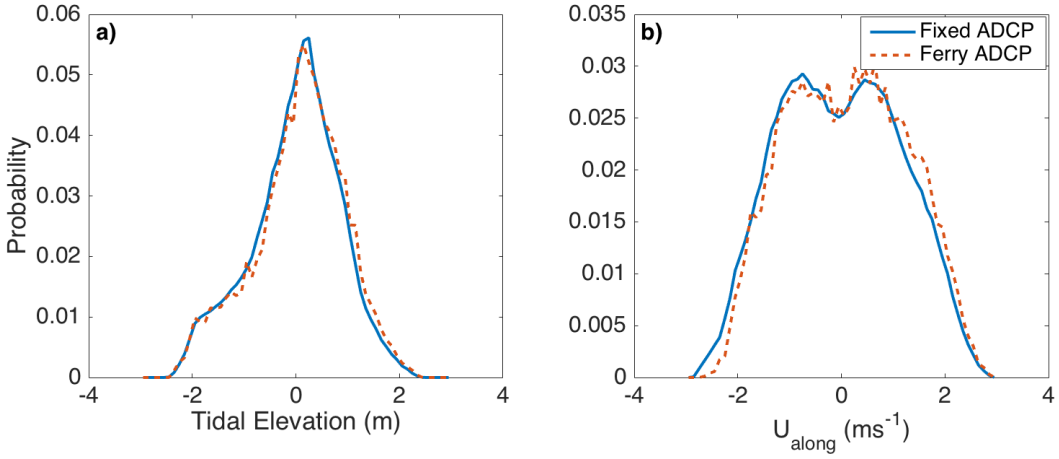


Figure 4.5: Probability distribution of a) tidal elevation, and b) along-channel depth-averaged velocity. Blue lines represent distributions from a uniformly sampled time series, while the red dashed line represents the distribution from a non-uniformly sampled

using UTIDE (Codiga, 2011), which is a unified tidal analysis and prediction model. UTIDE performs harmonic analysis of two-dimensional time series with irregular sample times, such as the time series created in the griding process. Harmonic analysis is also applied to the fixed ADCP data for comparison.

Ferry measurements are ongoing, thus the data set is continuously growing. Here, the accuracy and convergence of the harmonic analysis results are tested as more valid samples are added to the data set. Using data from a single grid cell at a single depth, harmonic analysis is applied to a valid velocity time series of increasing length. For each test, one extra month of data was added, which for some cases meant adding a reduced amount of new valid data or none at all. Figure 4.6 shows the harmonic analysis test results for the $M_2$ tidal current semi-major amplitude (which is the dominant harmonic at Admiralty Inlet) together with the confidence interval results from UTIDE. As seen in this plot, the confidence intervals decrease significantly when more than 10,000 valid data points are used in the analysis. When more than 20,000 valid samples are used, the $M_2$ amplitude has converged and the confidence interval width remains constant. The confidence interval width is fitted

to the amount of valid samples $N$, and it is found to agree very well to the typical standard error definition of $1/\sqrt{N}$,

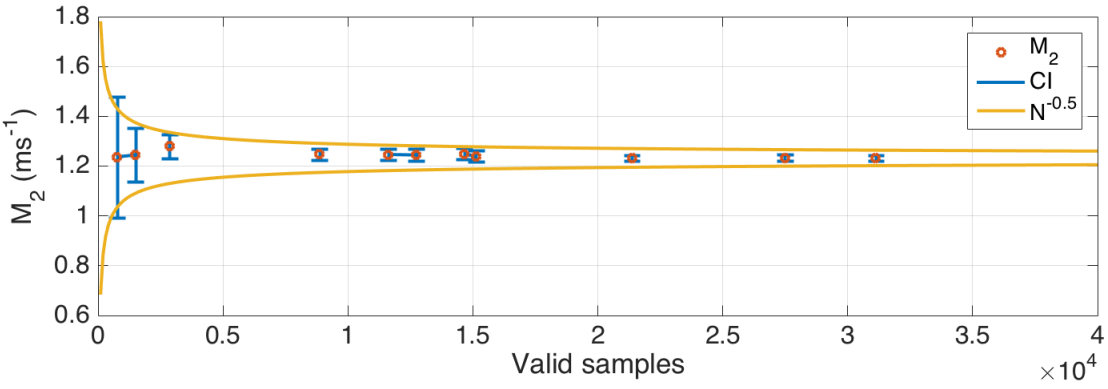


Figure 4.6: Sensitivity of HA

Based on this convergence, the ferry-based ADCP measurements to-date are sufficient to resolve the tides. Harmonic analysis is applied at all horizontal and vertical grid cells to obtain a spatial distribution of the tidal current harmonics across the inlet.

At least 5 tidal current components are recognized from the data set ($M_2$, $S_2$, $N_2$, $K_1$ and $O_1$), accounting for ~95% of the energy in the tidal current signal. Figure 4.7 shows the vertical distribution of the $M_2$ tidal current harmonic component and its correspondent confidence interval across the inlet. Large spatial variability is observed in the amplitude of this tidal current component, probably related to topographic and bathymetric features of the area. Lower amplitudes (below 0.5 $ms^{-1}$) are observed in the shallow area to the south of Port Townsend. Stronger amplitudes (above 1 $ms^{-1}$) are observed through the water column at mid channel, where a deeper and narrow channel exists. However, confidence intervals are large in the shallower areas south of Port Townsend and closer to the bottom in the deeper channel, probably because less data is available at those locations.

Comparisons are made with harmonic analysis results from the additional bottom-fixed ADCP measurements and from the Tidal Energy Atlas data. Since the Tidal Energy Atlas only provides harmonic results from depth-averaged tidal currents, harmonic analysis is

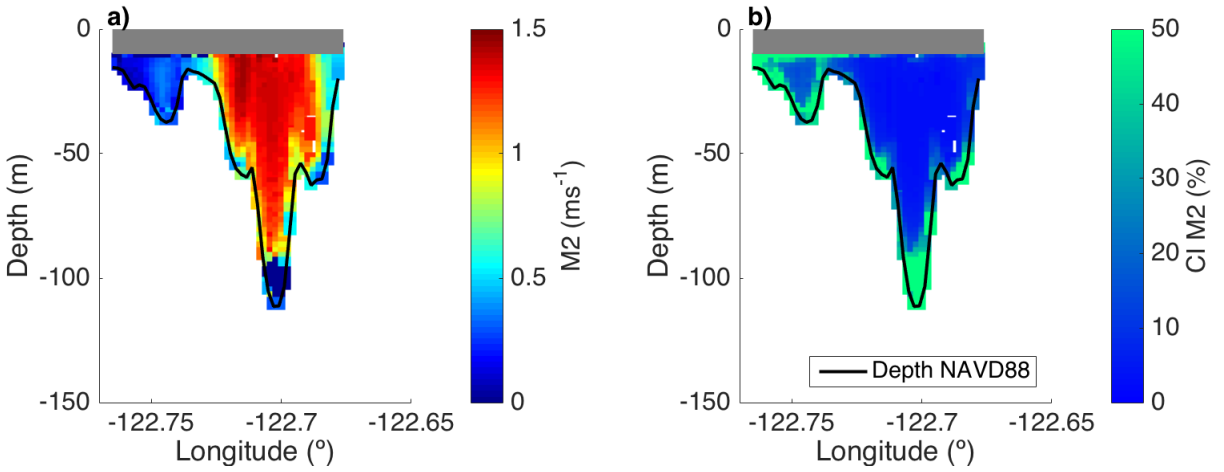


Figure 4.7: Harmonic analysis results across Admiralty Inlet: a) $M_2$ tidal current semi-major amplitude in $ms^{-1}$, and b) confidence intervals expressed as a percentage of amplitude. Gray area represents water column depth not covered by the ferry measurements (down to $z = -10$ m).

applied to depth-averaged currents from the ferry-based measurements and from the fixed ADCPs.

Not all deployments covered the same portion of the water column, and the ferry-based measurements do not cover the top 10 m of the water column (they were removed in the quality control process). Following a sensitivity analysis of the portion of the water column used in depth-averaging the currents, using the middle 55% of the water column (from 15% to 70%) results in the same depth-average values as if the whole water column is used (at Admiralty Inlet). Hence, a 55% column is used to define the depth-average currents for comparison of all fixed deployments and for the ferry-based measurements.

Figure 4.8 shows $M_2$ depth-averaged tidal current ellipses from the different data sets. In general, results from ferry measurements align with those from the bottom-fixed ADCPs and with those form the Tidal Energy Atlas in the deeper mid-section of the channel. Results from the ferries show slower currents than those from the fixed ADCPs, but higher than those from the Atlas. Note that tidal current amplitudes from the Tidal Energy Atlas

are always smaller than those from bottom-mounted ADCPs (Thyng et al., 2013). At the mid-channel section, grid cells contain above 15,000 valid measurements, and the smaller confidence intervals are observed in the harmonic analysis results for the $M_2$ component.

A large difference is observed in both semi-major amplitude and ellipse orientation near Admiralty Head (see Figure 4.9). Large variations on tidal currents, occurring within $\mathcal{O}(100)$ m, have been observed here, likely related to flow separation caused by the headland (Polagye and Thomson, 2013; Palodichuk et al., 2013). These gradients are illustrated by the Tidal Energy Atlas ellipses, which rapidly increase in magnitude near the PMEC ADCPs locations. South of the headland, the currents reduce as they turn, as shown by the PMEC ellipse towards the north-east. In this area, the ferry ellipses follow the same trend, but are significantly smaller. This discrepancy can be explained by spatial variability occurring within the grid cells, which are 3 km long in the along channel direction, and thus do not capture small spatial gradients. Perhaps, a higher-resolution grid can be applied in the along-channel direction at this area of the inlet that can capture the currents spatial gradients, however these new grid cells would be less populated, which might affect harmonic analysis convergence.

### *4.4.2 Exchange Flow*

The estimation of the total exchange flow between Puget Sound and the ocean requires long-term characterization (for several seasons) of the currents across Admiralty Inlet. Here, gridded ferry-based measurements are tested to capture sub-tidal residual currents and are compared to co-temporal measurements from a fixed bottom-mounted ADCP.

The overall mean velocity through the water column, a proxy for average residual flow, is explored. Estimations of mean flow velocities across the inlet (using the entire duration of the data set) and its corresponding standard error are shown in Figure 4.10. Interesting spatial circulation patterns are observed. Mid-channel is flood dominated while the area near Admiralty Head is ebb dominated, as previously observed by Polagye and Thomson (2013). Stronger inflow is observed in the deeper portion of the channel, as expected for

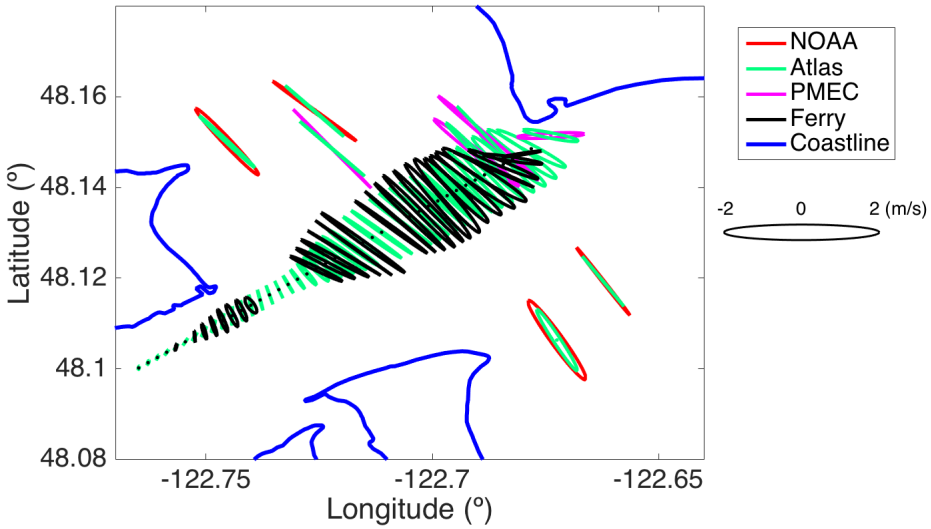


Figure 4.8: $M_2$ depth-average tidal current ellipses from different data sets. In black from ferry-mounted ADCPs, in red from NOAA-COOPS ADCPs, and in pink from PMEC ADCPs. Green ellipses are from NREL Tidal Energy Atlas at the ferry data grid, NOAA-COOPS, and PMEC locations.

denser ocean water. No outflow is observed in the upper water column, since that portion is not well captured by the ferry-based measurements. However, the mean flow magnitudes are greater than those observed during fixed bottom-mounted deployments, as shown in the next section.

Results from a single grid location are compared with co-temporal data from one of NOAA's ADCPs. Mean velocity profiles are estimated at one of the mid-channel grid cells (centered at 48.1359° N -122.7009° W) and at NOAA station PUG1624 (48.1569° N -122.7260° W). Both locations are aligned, but are located 3 km apart in the along-channel direction. Ferry-based velocities from June 21 to August 21 2016 are used for time-averaging to match collection dates from station PUG1624.

Figure 4.11 shows the obtained vertical profiles of mean velocities. The profile from the ferry-based measurements shows mean flows an order of magnitude stronger, and no outflow

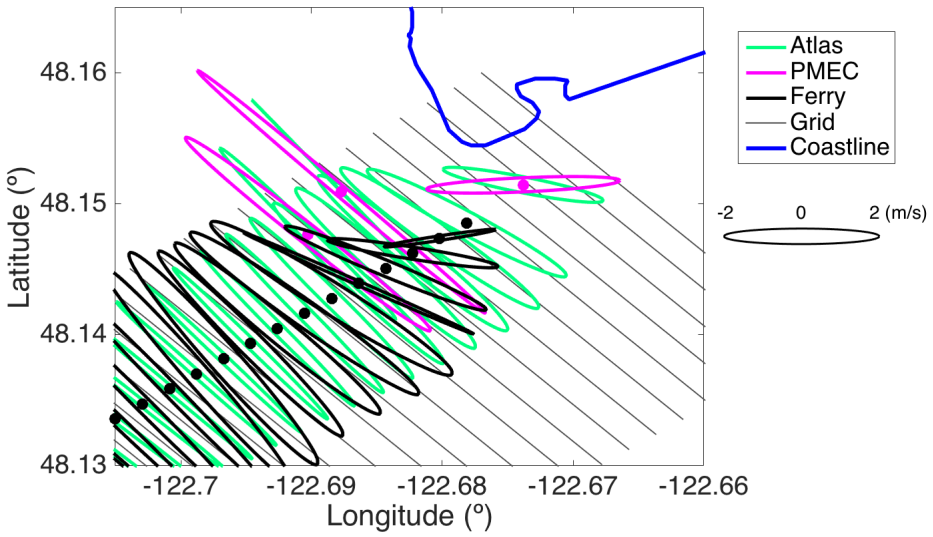


Figure 4.9: Zoom in version of $M_2$ depth-average tidal current ellipses from different data sets. In black from ferry-mounted ADCPs, and in pink from PMEC ADCPs. Green ellipses are from NREL Tidal Energy Atlas at the ferry data grid and PMEC locations. Dots represent the ellipses center location, and gray lines represent the grid edges.

(negative, towards the ocean) is observed in the upper water column since no data is available there. However, the expected trend is observed in the lower portion of the water column, where stronger average flows are observed towards the bottom. The large differences between both mean flow estimates might be explained by the spareness of the ferry-based time series. To test this hypothesis, the bottom-fixed data is subsampled down to the spareness of the valid ferry-based measurements (i.e., using on the valid collection times from the ferry data). The residual currents from the sub-sampled time series increase and are of the same order of magnitude of the ferry-based residual currents, consistent with the hypothesis.

For real time operational purposes, such as forecasting ocean water intrusions, time series of residual flows are needed (Deppe et al., 2018). Here, the capabilities of the ferry-based data set to capture the temporal residual currents is explored. A low-pass filter of 40 hour half-amplitude period is applied to along-channel velocity time series, at different depths,

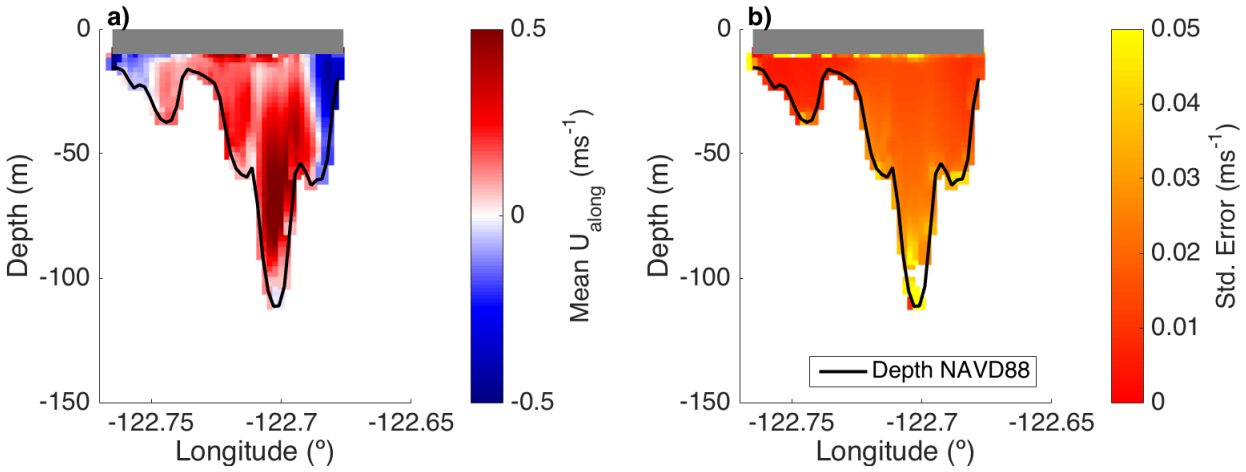


Figure 4.10: a) Map of time-averaged velocities using entire length of velocity time series within each grid cell, and b) corresponding standard error of the time-averaged quantities.

in order to remove the tidal currents and retain the residual currents (Alessi et al., 1985; Polagye and Thomson, 2013; Deppe et al., 2018). Residual flows are also estimated for the subsampled data from station PUG1624 to fairly compare the results from the ferry-based measurements. Figure 4.12 shows the obtained co-temporal time series of residual currents ($\sim$35 m below the free-surface). Large differences are observed in the residual flows estimated from the two different platforms. Large magnitude oscillations remain in the residual currents when applying the filter to a sparse time series, and this indicates that such a method is not suitable for the sparse ferry dataset. Other authors have applied harmonic analysis to obtain tidal currents predictions, and estimated residual currents time-series by removing the predictions from the measurements (Nauw et al., 2014). However, this approach requires to resolve most of the tidal harmonic components such that all tidal periods are removed from the measurements.

The results suggest that the ferry-based data are sufficient to determine the spatial patterns of residual flow through Admiralty Inlet, but that it will be difficult to use this data for quantitative estimates of residual currents. The data are still of great value, because the spatial patterns obtained could be used to guide the placement of more continuous monitoring

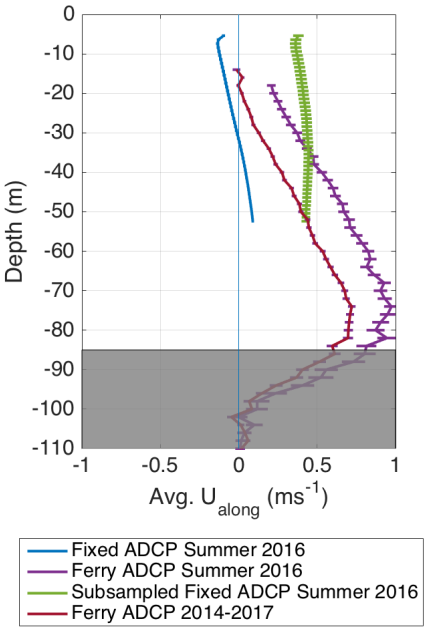


Figure 4.11: Time-averaged velocity profile from fixed bottom-mounted ADCP measurements in blue, from ferry-based measurements within a single grid cell in purple, from subsampled fixed bottom-mounted ADCP measurements in green, and from the entire ferry-based time series at the same grid cell in red. Horizontal lines represent standard error on estimating the time-average values. Gray covered area correspond to depth variations within the grid cell.

of residual flows.

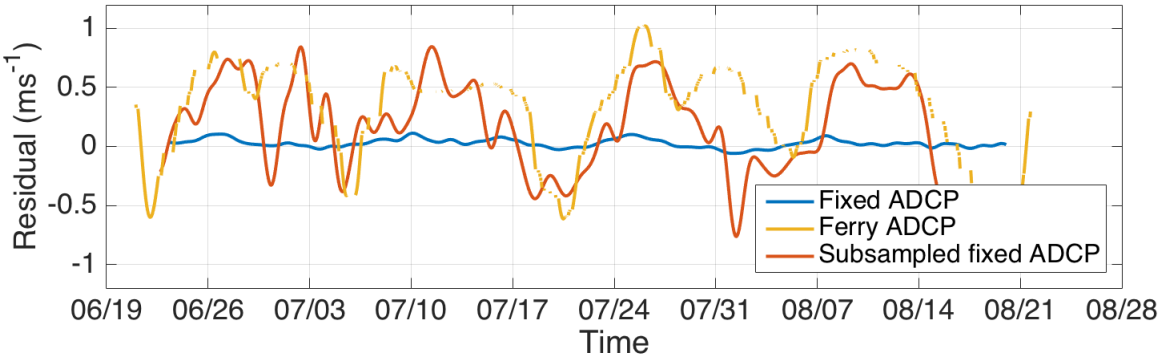


Figure 4.12: Time series of residual currents from fixed bottom-mounted ADCP at NOAA station PUG1624 (blue), from ferry-based ADCP measurements within single grid cell (yellow), and from a sub-sampled bottom-mounted ADCP at NOAA station PUG1624 (red).

## *4.5 Conclusions*

Long-term observations of currents across Admiralty Inlet from ferry-mounted acoustic Doppler current profilers (ADCPs) are quality controlled, organized, and tested to capture tidal current harmonics and residual flows through the inlet. Data are collected by two ADCPs mounted on board two ferries that cross Admiralty Inlet about twelve times a day. All measurements are organized into a horizontal and vertical grid, that results in non-uniform time series of velocities across the entire inlet.

Despite the dramatic reduction of data coverage during quality control, the remaining data successfully captures the main tidal current harmonics. New maps of tidal currents harmonics are now available across and through the depth of Admiralty Inlet. Harmonic analysis shows sharp gradients in tidal current amplitudes across the inlet, probably related to the bathymetric features of the inlet. Stronger currents are observed mid-channel and towards the north-east end of the inlet, while slower currents are observed in the enclosed shallow area south of Port Townsend.

Harmonic analysis results agree well with those from fixed bottom-mounted ADCPs towards mid-channel in terms of ellipses amplitude and orientation. Less agreement is found

towards the shallow areas of the inlet and closer to the shore, specially near Admiralty Head. These differences might be explained by large horizontal gradients in the currents observed there, which are obscured by the griding process. The latter suggest that another method, such as the station keeping method from Palodichuk et al. (2013), should be better suited to map those areas at higher resolution.

A new map of mean flow velocities is obtained from the ferry-based measurements. This map exhibits the spatial circulation pattern across Admiralty Inlet, where stronger inland mean flows occur in the deeper portion of the channel, while stronger outflow occurs near Admiralty Head. A first attempt to estimate time series of residual currents from ferry-based measurements by filtering out the tidal currents is presented, however the temporal method fails due to the sparseness of the gridded velocity time series. The ferry-based measurements are not suitable for real-time estimations of residual flows, and no improvement is found from the forecasting method of Deppe et al. (2018).

Ferry-based data provides new insights on the spatial distribution of currents through Admiralty Inlet. Results obtained so far could improve tidal currents maps through Admiralty Inlet, estimates of the tidal energy resource available, and numerical hydrodynamic models of the area. Measurements are ongoing, thus better estimates of tidal currents harmonic components will be available over time, which may reduce the need for large spatial bins to accumulate a sufficient number of data points. New methods for estimating residual flows from sparse datasets need to be explored in order to estimate the total exchange flow through Admiralty Inlet.

# Chapter 5

# WAKE MEASUREMENTS FROM A HYDROKINETIC RIVER TURBINE

## *5.1 Introduction*

Hydrokinetic energy is a predictable energy source available in streams, rivers, and tidal channels with sufficiently fast water velocities. The extraction of hydrokinetic energy for electricity generation requires the installation of hydrokinetic turbines facing the flow field. As the development of hydrokinetic turbines reaches a commercial stage, it is essential for hydrokinetic energy extraction projects to have detailed information about the hydrodynamics of these natural systems, for both turbine design and resource assessment. In addition to ambient conditions, it is indispensable to understand and quantify the environmental impacts caused by these underwater turbines (Cada et al., 2007; Boehlert and Gill, 2010; Polagye et al., 2011). Specifically, the study of the wake generated by the turbines is essential in the characterization of hydrodynamic effects. Wake analysis reveals changes to the mean flow and mixing around the turbine, as well as effects farther downstream. The wake extent and its features can have an impact in the distribution and efficiency of additional turbines (Adaramola and Krogstad, 2011; Myers and Bahaj, 2012; Neary et al., 2013), and the combined wake of turbine arrays can even affect the large-scale hydrodynamics of the environment (De Dominicis et al., 2017; Brown et al., 2017).

The wake of an hydrokinetic turbine is generally characterized by: i) a deficit in the mean flow due to the drag produced by the turbine structure and due to energy extraction; ii) a modification in turbulence due to eddies shed by the structure and the turbine blades; and iii) complex interactions between natural and turbine-induced turbulent structures (Chamorro et al., 2013a; Neary et al., 2013; Kang et al., 2014; Chamorro et al., 2015).

The idealized wake of a hydrokinetic turbine gradually expands into a cone shape region to conserve momentum (Myers and Bahaj, 2010). Turbulent mixing occurs in the boundary of the region between the wake and the undisturbed flow field, bringing energy into the wake region, which smooths the velocity deficit. After several turbine length scales downstream from the turbine, the wake is supposed to dissipate and the flow returns to its original conditions (Myers and Bahaj, 2010). Of course, the flow can never fully 'recover' to original conditions, because kinetic energy is being extracted from the system. In some cases, the natural system converts potential energy to kinetic energy such that a pseudo-recovery can occur, but there is still a net energy loss in the extraction and subsequent wake. The variables that are thought to impact the turbine's wake are the rotor thrust, ambient and device induced turbulence, proximity to boundaries (bed or free surface), and the vertical and horizontal velocity profiles (Myers and Bahaj, 2010).

Much of the research on hydrokinetic turbine wakes has been carried out numerically (Kang et al., 2012; Blackmore et al., 2014; Boudreau and Dumas, 2017; Chawdhary et al., 2017) and at the laboratory scale under simplified and controlled conditions (Myers and Bahaj, 2007, 2012; Chamorro et al., 2013b; Bachant and Wosnik, 2015; Chawdhary et al., 2017; Chen et al., 2017). These studies differ mainly in the type and number of turbines, and in how detailed the turbine and the energy extraction are represented (Day et al., 2015). At the field scale, towing experiments of a vertical cross-flow turbine have been conducted in an unconfined environment in Polagye et al. (2013).

At the laboratory scale, turbulent flow interactions with a three-bladed, 0.5 m diameter, horizontal axis hydrokinetic turbine and its turbulent wake are studied in Chamorro et al. (2013a). Chamorro et al. (2013a) observed that the velocity deficit persists beyond 15 turbine diameters at hub height (10% velocity deficit at 15 diameters downstream) (Chamorro et al., 2013a), and that wake recovery is enhanced by the higher shear in the top portion of the water column (Chamorro et al., 2013a). The authors also observed that the velocity deficit at hub height is related to the turbine's tip-speed ratio, since the extracted power is related

to this parameter [1]. In terms of turbulence intensity, this turbine wake showed variability along the water column (Chamorro et al., 2013a). The higher levels of turbulence intensity were observed about 5 turbine diameters downstream of the turbine at the top portion of the wake (where the higher mean flow shear occurred in the wake), and it is reported that the increased turbulence intensity expands and reaches the free-surface about 15 diameters downstream of the turbine (Chamorro et al., 2013a).

The wake structure and recovery processes differ between axial-flow turbines and cross-flow turbines, as previous investigations have shown that cross-flow turbines are more efficient in wake recovery than axial-flow turbines (Bachant and Wosnik, 2015). The near-wake of a vertical cross-flow turbine is assessed in Bachant and Wosnik (2015). The near-wake of Bachant and Wosnik (2015) turbine is characterized by an asymmetric velocity deficit, high magnitude Reynolds stresses in the boundaries of the wake, and asymmetric turbulent kinetic energy (enhanced in the side corresponding to blade vortex shedding, were the minimum velocity deficit was found) (Bachant and Wosnik, 2015). Bachant and Wosnik (2015) also identify the processes that contribute to faster wake recovery in cross-flow turbines by examining the terms in the stream-wise Reynolds-averaged Navier-Stokes (RANS) equation and in the kinetic energy balance. For their case, the authors found that wake recovery is dominated by the advection terms rather than by turbulence transport (Bachant and Wosnik, 2015), which makes cross-flow turbines more efficient in entraining momentum into the wake when compared with axial-flow turbines (Bachant and Wosnik, 2015).

The wake of a cross-flow turbine is investigated numerically in Boudreau and Dumas (2017) by solving the Unsteady-RANS equations around a single rotating cross-flow blade in an unconfined channel. Strong deficit in all three velocity components was observed (60%), together with distinct direction patterns in vertical and cross-stream velocities. In the stream-wise direction, the wake expands both laterally and vertically, while the mean stream-wise velocity continuously increases downstream of the turbine, reaching an 85% recovery

[1] For general turbine characteristics and performance parameters refer to Burton et al. (2001) and Batten et al. (2008).

after 12 turbine diameters. Stream-wise velocity evolution downstream of the turbine is found to be dominated by cross-stream and vertical advection together with the stream-wise pressure gradient.

Despite the large amount of research regarding the turbine wake at the numerical and laboratory scales, there is a lack of field observations in real environments, probably due to the low number of full-scale turbines deployed around the world. However, field measurements are critical for validating numerical results and for scaling laboratory experiments results, as well as for estimating the true environmental effects of hydrokinetic energy extraction at each location.

This paper presents the first field observations of the wake from a full-scale hydrokinetic turbine under natural flow conditions. Specifically, a detailed characterization of Ocean Renewable Power Company (ORPC) RivGen turbine wake in the Kvichak river (Alaska) is reported. The site and turbine details together with the measurements methodology are presented in section 5.2. Section 5.3 presents a description of the wake in terms of mean flow and turbulence parameters. A discussion on the wake evolution, on the wake of a not-operational turbine, and on the wake energy loss is presented in section 5.4, followed by Conclusions in section 5.5.

## *5.2 Methods*

### *5.2.1 Site and Turbine Description*

The Kvichak river, located in southwest Alaska, drains the Iliamna Lake flowing southwest towards Bristol Bay. The turbine deployment site is about 2 km downstream from the Iliamna Lake, next to the village of Igiugig, where the river is approximately 5 m deep and 150 m wide. The flow is at is maximum, $\sim$ 2.5 m/s, in the center of the river. Figure 5.1a shows a map of the Kvichak river bathymetry on top of a Google Earth image of the area, together with the location of the turbine deployment site: N 59° 19.495′; W 155° 54.890′.

The Ocean Renewable Power Company (ORPC) RivGen turbine is an horizontal cross-

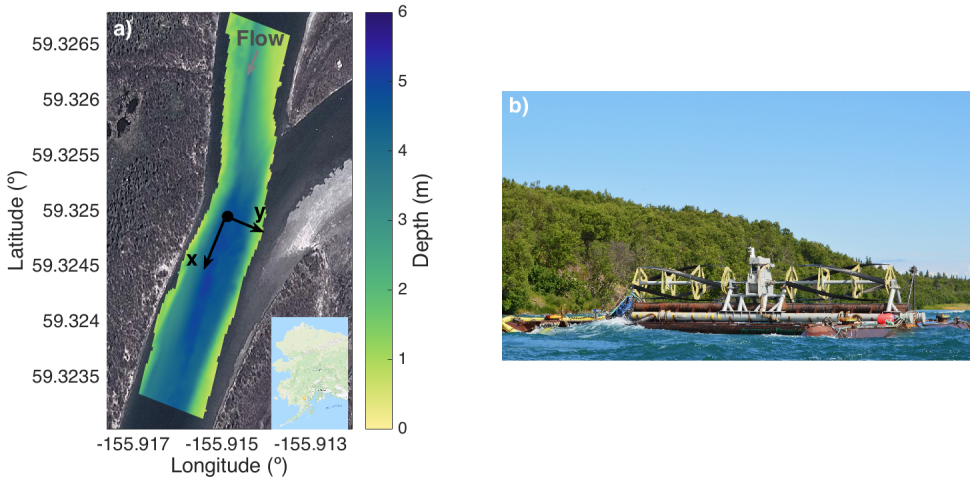


Figure 5.1: a) Google Earth image of the Kvichak river and river bathymetry in colors. Black dot shows turbine location, and black arrows identify the local coordinate system used through the wake analysis. Grey arrow represents the flow main direction. b) Downstream view of ORPC RivGen sitting on top of the Kvichak's river free surface prior to its submergence in July 2015.

flow hydrokinetic turbine rated at 35 kW (Forbush et al., 2016). The turbine consists in two rotors plus a generator located in between the rotors. The entire turbine is 11.5 m wide, and each rotor is 1.5 m in diameter. Turbine hub-height at this location is approximately 2.5 m below the river free surface when the turbine is submerged and resting on the riverbed. Turbine blockage in the Kvichak river was estimated to be 10% when considering the turbine swept area plus the turbine's support structure area over the area of the river cross-section at the turbine location. Details of turbine performance in the Kvichak river can be found in the work of Forbush et al. (2016). A picture of ORPC RivGen sitting on top of the river free surface prior to its deployment is shown in Figure 5.1b.

### *5.2.2 Data Collection*

Hydrodynamic data was collected in the area surrounding RivGen prior to and after its the deployment on July 2015. A new version of the SWIFT v4$\beta$ drifter buoy (Thomson,

2012) was used to measure surface velocity and velocity fluctuations along the water column (Figure 5.3). A summary of all instrument deployments and settings is presented in Table 5.1.

A Nortek Signature1000 five-beam acoustic Doppler current profiler (AD2CP) was mounted down-looking on a disk buoy, which was equipped with two Qstarz GPS data receivers. The Signature1000 measured along-beam velocities trough the water column as it was drifting using its five beams at 8 Hz in broadband mode. There were 14 depth bins separated by 0.5 m, and a 0.5 m blanking distance. Single ping error, $\sigma_b$, reported by the instrument manufacturer is 0.05 $\text{ms}^{-1}$ for the along-beam velocities. The GPS measured geographic position, drifting velocity, and heading at 10 Hz, with a 5 m accuracy in position and 0.05 $\text{ms}^{-1}$ in drifting velocity (using a phase-resolving GPS antenna).

Drifts began $\sim$ 200 m upstream of the turbine location by releasing the drifter from a small vessel. The drifter was released at different positions across the river in order to follow different surface streamlines across the river. After each drift, the SWIFT was recovered $\sim$ 200 m downstream of the turbine.

Two sets of drifts were conducted: before and after turbine deployment. The first set aimed to characterize the river in its undisturbed state. This data set consisted of 150 drifts between July $8^{th}$ and July $13^{th}$, 2015. A portion of the drifts (15) were set-up to measure altimetry (bathymetry) with additional pings, and this restricted along beam velocity sampling to 4 Hz (instead of 8 Hz).

The second set of drifts was conducted after turbine deployment, from July $19^{th}$ to July $21^{st}$, 2015. On July $19^{th}$ 2015, the turbine was underwater but not-operational (braked), while on July $20^{th}$ and $21^{st}$, the turbine was operational and delivering electricity to the grid. There were 40 drifts while the turbine was not-operational, and 150 while it was operational. These data sets covered the same longitudinal river span as for the no turbine conditions, but concentrated drifts over and next to the turbine to evaluate the turbine wake. As for the first set, 25 drifts were taken in altimeter mode, measuring along-beam velocities at 4 Hz.

Data from the Signature1000 was quality controlled by removing measurements with low beam correlations (less than 30) and low echo amplitude (less than 80 dB). This process allowed to remove all data recorded while the SWIFT was outside of the water, and to recognize the riverbed.

An additional data set was obtained prior to turbine deployment using a Nortek Vector acoustic Doppler velocimeter (ADV) in order to provide ORPC with upstream turbine flow conditions and to test the accuracy of the drifting method measurements. The ADV was mounted on a turbulence torpedo (TT), a sounding weight that hangs from a davit on the aft of a small vessel while the vessel is holding station (Harding et al., 2017; Kilcher et al., 2017). The ADV targeted the turbine hub-height (2.5 m below river free surface) at several locations around the turbine site. Vessel location and drifting velocity were recorded using two Qstarz GPS located on top of the davit. The ADV sampled turbulent velocities at 16 Hz, for about 20 minutes at each targeted location. ADV data was quality-controlled to remove data with low correlation and low echo amplitude, and despiked using the 3D phase space method of Goring and Nikora (2002). The ADV data was organized in 1 minute ensembles and screened by vessel drifting velocity, where data with an ensemble-averaged vessel drifting velocity higher than 0.5 $ms^{-1}$ were removed (not holding station). Additional motion contamination from the deployment platform was removed by applying the methods presented in (Kilcher et al., 2017).

In order to make the data sets comparable to each other for the analysis to follow, it is essential to assume steady state conditions (in the mean flow sense) in the Kvichak river during the measurements period. During the measurements period atmospheric conditions were mild and no large rain or flood events were observed. Since there are no stream flow gauges available in the Kvichak river, the steady state assumption is tested using velocity measurements taken upstream of the turbine location through the entire measurement period, and depth variations taken just upstream of the turbine while the turbine was underwater.

True Eulerian velocities taken mid-river between 20 and 30 m upstream of the turbine (within four highly populated grid cells) are used to test the steady state assumption through

the measurements period. There were 1054 instantaneous velocity measurements within this location among 9 days of measurements. Turbulent velocities together with daily averages measured at hub-height at this location are shown in Figure 5.2. Error bars correspond to one standard deviation from the daily averages. No trend is observed in the daily averaged velocities, and the total averaged velocity from those measurements lies within the error bars through the measurement period.

Data from a HOBO pressure gauge installed on RivGen's frame, just upstream the turbine, are converted to water depth after removing the atmospheric pressure data. Atmospheric pressure measured at the Igiugig Airport weather station (USAF-703061) during the measurements period is shown in Figure 5.2a. During the first period of measurements (no turbine in the river), atmospheric pressure remained fairly constant at around 100 kPa. Increased atmospheric pressure was observed during the not-operational turbine measurements and for the first day of the operational turbine measurements. The effective accuracy from the HOBO pressure gages is 3 cm in depth. The water depth data presented in Figure 5.2c shows no significant trend. However, high-frequency depth variations between $\pm 5$ cm, over a 3.66 m mean depth were observed on July 19-21 2015.

Although there is variability in the flow conditions during the measurements, the steady-state assumption is statistically valid (i.e., none of the variations in the mean values exceed the uncertainties) during the entire measurement period. Furthermore, the upstream variations of order 0.1 $\text{ms}^{-1}$ and much smaller than the wake signal, which is order 0.5 $\text{ms}^{-1}$.

### *5.2.3 Coordinate Systems*

A local coordinate system is defined (shown in Figure 5.1a) for data organization purposes, with $x$ along the stream-wise direction, $y$ in the cross-stream direction, and $z$ in the vertical direction (positive upwards). The local coordinate system origin is at the free surface at the nominal center of the turbine (N 59° 19.495′; W 155° 54.890′), and the local axis rotation from an east-north-up (true) coordinate system is 107° clockwise from north. The same coordinate system is used to define river velocities, with $x$ corresponding to the stream-wise

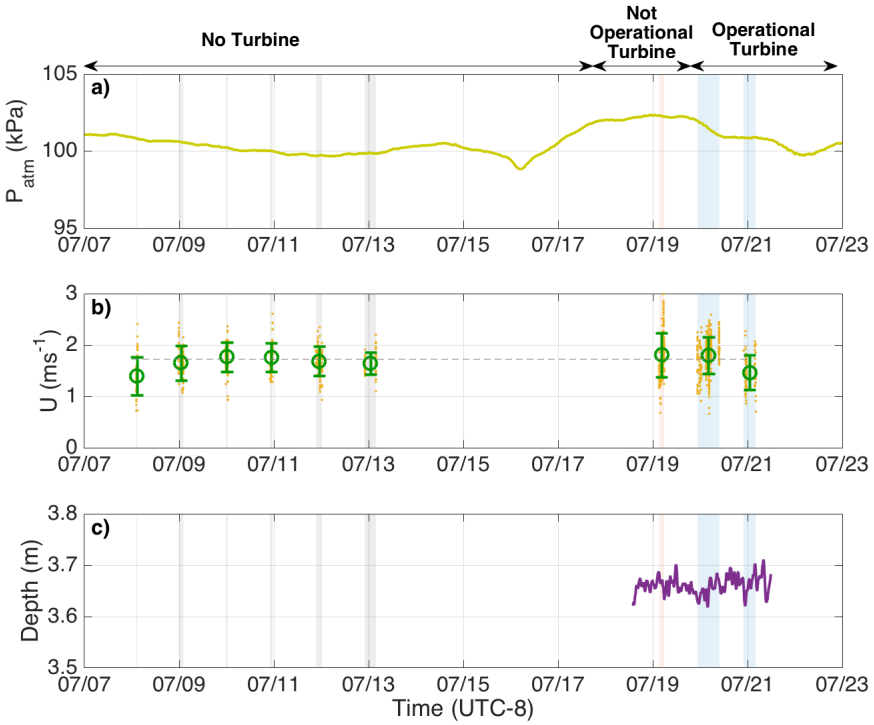


Figure 5.2: a) Atmospheric pressure from Igiugig Airport weather station, b) Hub-height velocity upstream of the turbine: instantaneous velocity in orange, and daily averages in dark green, and c) water depth measurements upstream of the turbine. In all figures shaded areas correspond with the times of the three data sets from the SWIFT buoy: no turbine (gray), not operational turbine (red), and operational turbine (blue).

Table 5.1: Summary of deployments and sampling parameters at the Kvichak river

| Turbine State | No Turbine | No Turbine | Not Operational | Operational |
|---|---|---|---|---|
| Instrument | Nortek Vector | Nortek Signature 1000 | Nortek Signature 1000 | Nortek Signature 1000 |
| Dates | 8-13 July 2015 | 8-13 July 2015 | 19 July 2015 | 20-21 July 2015 |
| Hold Stations/Drifts | 35 | 150 | 40 | 150 |
| Sampling Frequency (Hz) | 16 | 8 | 8 | 8 |
| z target (m) | -2.5 | - | - | - |
| $\Delta z$ (m) | - | 0.5 | 0.5 | 0.5 |
| Distance to first cell (m) | - | 0.25 | 0.25 | 0.25 |
| Range (m) | - | 7 | 7 | 7 |
| Single ping error ($ms^{-1}$) | 0.02 | 0.05 | 0.05 | 0.05 |

velocity $u$, $y$ corresponding to the cross-stream velocity $v$, and $z$ corresponding with the vertical velocity $w$. The location of each measurement, originally in latitude and longitude coordinates, is mapped to the local coordinate system.

Following the coordinate change, all data sets (including the data from the turbulence torpedo ADV) are organized by location in a three-dimensional structured uniform grid defined in the local coordinate system. The grid is of 2 m horizontal resolution, and 0.5 m vertical resolution (coincident with the Signature1000 velocity bins). The grid covered from -200 m to 200 m in $x$, from -60 m to 60 m in $y$, and from 0 m to -7 m in $z$. The ADV data set grid contained data only at $z = -2.5$m, corresponding to turbine hub-height.

Within each grid cell two data products are constructed: true Eulerian velocities and pseudo-beam velocities, which will be used in the coming sections to define river mean-flow and turbulence parameters, respectively.

*True Eulerian Velocities*

Velocities captured by the drifting Signature1000 correspond to fluctuations from the surface drifting velocity. All recorded velocities (from the GPS and from the Signature1000) are converted to east-north-up (ENU) velocities, and subsequently converted to velocities in the local coordinate system ($u$, $v$, and $w$). True Eulerian velocity profiles in the local coordinate system are constructed as:

$$u(x, y, z, t) = u_{GPS}(x, y, t) + u_{Sig}(x, y, z, t) \tag{5.1}$$

$$v(x, y, z, t) = v_{GPS}(x, y, t) + v_{Sig}(x, y, z, t) \tag{5.2}$$

where $u$ and $v$ correspond to the horizontal components of velocity in the local coordinate system, the $GPS$ subscript represents drifting velocity components recorded by the GPS, and the $Sig$ subscript represents velocity components recorded by the Signature1000. Vertical profiles of vertical velocities $w$ do not need to be reconstructed as they are directly recorded by vertical beam of the Signature1000.

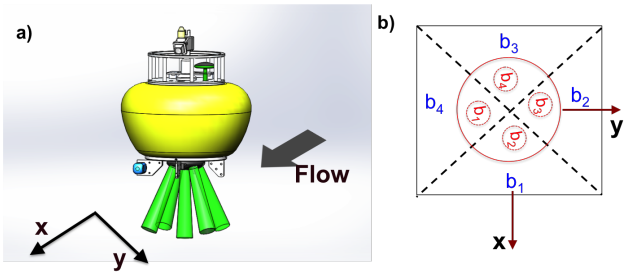


Figure 5.3: a) SWIFT v4 prototype schematic, rendered by Alex de Klerk (APL-UW). Green cone-shape areas illustrate the Nortek Signature1000 along-beam velocity directions. b) Plan-view of a single horizontal grid cell illustrating the pseudo-along beam velocities local system. In red is an example of miss-aligned along-beam velocities from the Signature1000.

*Pseudo-beam velocities*

During these measurements, instrument horizontal rotation could not be controlled, thus the heading of the Signature1000 changed within each drift. Then, within each grid cell, the raw along-beam velocities recorded by the Signature1000 might not coincide with each other in direction, hence no time-series of along-beam velocities can be directly obtained. A fixed local system of four pseudo-beam velocities directions is defined within each grid cell to overcome this difficulty. In the new system, the horizontal component direction of each pseudo-beam velocity corresponds with the direction of the local coordinate system axis: the horizontal component of $b_1$ corresponds with the positive x-axis, the one from $b_2$ corresponds with the positive y-axis, the one from $b_3$ corresponds with the negative x-axis, and the one from $b_4$ corresponds with the negative y-axis direction. The pseudo-beam velocity coordinate system is shown in Figure 5.3b together with an example of the miss-alignment between the local-coordinate system and the Signature1000 along-beam velocities.

For every single measurement, the pseudo-beam velocities are constructed based on the heading recorded by the Signature1000, as the heading indicates the direction of the recorded along-beam velocities with respect to the local coordinate system. First, a heading with respect to the local x-axis is estimated as $H_x = H - 17°$, where $H$ is the instrument heading

Table 5.2: Pseudo-beam velocities based on instrument heading with respect to local coordinate system x-axis.

| Pseudo-beam velocities | $135° < H_x < 225°$ | $225° < H_x < 315°$ | $315° < H_x < 45°$ | $45° < H_x < 135°$ |
|---|---|---|---|---|
| $b_1$ | $b_{1Sig}$ | $b_{2Sig}$ | $b_{3Sig}$ | $b_{4Sig}$ |
| $b_2$ | $b_{2Sig}$ | $b_{3Sig}$ | $b_{4Sig}$ | $b_{1Sig}$ |
| $b_3$ | $b_{3Sig}$ | $b_{4Sig}$ | $b_{1Sig}$ | $b_{2Sig}$ |
| $b_4$ | $b_{4Sig}$ | $b_{1Sig}$ | $b_{2Sig}$ | $b_{3Sig}$ |

and $H_x$ is the local heading. When $H_x = 180°$, the instrument x-axis is aligned with the local x-axis. Four 90° angular cells, each centered in the directions of the local coordinate system axis, are defined within each grid cell and are used to classify four heading scenarios. Based on $H_x$, pseudo-beam velocities are defined as shown in Table 5.2.

### *5.2.4 Mean flow parameters*

Mean flow parameters are obtained from the true Eulerian velocities estimated within each grid cell. These parameters are used to characterize and quantify the hydrodynamic effects of RivGen in the Kvichak river in the following sections.

At each grid cell, a non-uniform time-series of true Eulerian velocity components is available. Assuming steady state conditions in the Kvichak river during the field measurements, these time-series are averaged in order to have a single velocity vector at each grid-cell. All velocity measurements are affected by the intrinsic noise of the instruments that measures them. For this case, the velocity measurements are affected by the GPS velocity uncertainty and by the inherent Doppler noise of the Signature1000. After time-averaging the velocities, the horizontal velocity components uncertainty within each grid cell, $\sigma_u$, is defined as:

$$\sigma_u = \sqrt{\frac{\sigma^2_{u_{Sig}}}{N} + \frac{\sigma^2_{u_{GPS}}}{N}} \tag{5.3}$$

where $\sigma_{u_{Sig}}$ is the horizontal velocity uncertainty from the Signature1000, $\sigma_{u_{GPS}}$ is the

uncertainty of the velocity recorded by the GPS on board the SWIFT buoy, and $N$ is the number of velocity measurements available within each grid cell.

Using the time-averaged velocity vector at each grid cell, velocity shear is estimated by a centered finite difference scheme. A coarse vorticity is then estimated using the estimated discrete shear in all three Cartesian directions. The shear of the along-channel velocity component $u$ in the $x$ direction, and its uncertainty are defined as:

$$\frac{du}{dx} = \frac{u_{i+1,j,k} - u_{i-1,j,k}}{2\Delta x} \tag{5.4}$$

$$\sigma_{Shear} = \frac{1}{2\Delta x}\sqrt{\sigma^2_{u_{i+1,j,k}} + \sigma^2_{u_{i-1,j,k}}} \tag{5.5}$$

Where $i$, $j$, and $k$ represent each grid cell, $u$ is the x-axis velocity component, and $\sigma_u$ is the velocity component uncertainty previously defined in Eq. 5.3. The velocity shear in the other directions, and for the rest of the velocity components ($v$ and $w$), follows the same definition.

Additional mean flow parameters uncertainties arise from the error in the GPS measurements location and from natural variability within a grid-cell. These are assumed to be uncorrelated, and thus averaging within the grid-cells significantly reduce them.

### *5.2.5 Turbulence Parameters*

Turbulence parameters are obtained following the same methods presented in (Guerra and Thomson, 2017) for a 5-beam acoustic Doppler profiler, which are based on the variance of along-beam turbulence fluctuations. For this investigation, the pseudo-beam velocity fluctuations are used instead.

A pseudo-turbulence intensity (TI) is estimated using the pseudo-beam velocity variances, $b_i'^2$, relative to the mean flow velocity at each depth. The noise-corrected pseudo-TI, $pTI$, is defined as:

$$pTI(x,y,z) = \frac{\sqrt{\frac{1}{5}\sum_{i=1}^{5} b_i'^2(x,y,z,t) - \sigma_b^2}}{U(x,y,z)} \tag{5.6}$$

where $b_i$ represents each pseudo-beam velocity, $\sigma_b^2$ is the along-beam velocity noise variance removed following (Thomson et al., 2012), and $U$ is the horizontal velocity magnitude. The pseudo-beam measurements have independent noise errors, $\sigma_b$, and thus the use of all five pseudo-beam velocities is preferred to estimate the velocity variations at each grid cell. By only using the pseudo-beam velocities, pseudo-TI only captures the turbulent length scales similar to the beam separations. This spatial definition is uniformly biased low compared to the usual temporal definition of turbulent intensity $\sigma_U/\bar{U}$, where $\sigma_U$ is the standard deviation of the flow velocity and $\bar{U}$ corresponds to the mean flow velocity.

The five-beam configuration of the Signature1000 allows for the estimation of five out of six Reynolds stresses (Guerra and Thomson, 2017). Assuming zero-mean pitch and roll within each grid cell, the noise corrected Reynolds stresses are defined using the variance of the pseudo-beam velocity fluctuations as:

$$\overline{u'^2} = \frac{\overline{b_1'^2} + \overline{b_3'^2} - 2\overline{b_5'^2}\cos^2\theta}{2\sin^2\theta} - \sigma_b^2 \tag{5.7}$$

$$\overline{v'^2} = \frac{\overline{b_2'^2} + \overline{b_4'^2} - 2\overline{b_5'^2}\cos^2\theta}{2\sin^2\theta} - \sigma_b^2 \tag{5.8}$$

$$\overline{w'^2} = \overline{b_5'^2} - \sigma_b^2 \tag{5.9}$$

$$\overline{u'w'} = \frac{\overline{b_3'^2} - \overline{b_1'^2}}{4\sin\theta\cos\theta} \tag{5.10}$$

$$\overline{v'w'} = \frac{\overline{b_4'^2} - \overline{b_2'^2}}{4\sin\theta\cos\theta} \tag{5.11}$$

where $\overline{b_i'^2}$ corresponds to the pseudo-beam velocity variances, and $\theta$ is the beam inclination angle (25° for the Signature1000), and $\sigma_b^2$ corresponds to the noise variance from the Signature1000. The $\overline{u'^2}$ corresponds to the along-channel turbulent kinetic energy (TKE), which can be used to estimate an along-channel turbulence intensity as:

$$TI(x,y,z) = \frac{\sqrt{\overline{u'^2}}}{U(x,y,z)} \tag{5.12}$$

Both the along-channel turbulence intensity and the along-channel TKE will be used here as a measure of how the turbulence is increasing and how is it evolving downstream of the turbine.

The turbulent kinetic energy dissipation rate is estimated through the second-order spatial function of the along-beam velocity fluctuations $D(z,r)$, following the methodology described in (Wiles et al., 2006) and (Guerra and Thomson, 2017). This methodology requires the observation of the inertial sub-range of isotropic turbulence. Using the vertical beam velocity fluctuations, within each grid cell the structure function is defined as:

$$D(z,r) = \overline{\left(b_5'(z+r) - b_5'(z)\right)^2} \tag{5.13}$$

where $z$ is the along-beam measurement location, $b_5'$ corresponds to the velocity fluctuation along the vertical beam, and $r$ is the distance between two velocity bins; the overline denotes a time-average. In the inertial subrange of isotropic turbulence, the structure function is related to the distance $r$ and to the TKE dissipation rate $\varepsilon$ by:

$$D_i(z,r) = C_v^2 \varepsilon^{2/3} r^{2/3} \tag{5.14}$$

where $C_v^2$ is a constant equal to 2.1 (Wiles et al., 2006; Thomson et al., 2012).

The structure function is estimated using all instantaneous profiles within each grid cell (which correspond to a non-uniform time series). Then, the structure function is multiplied by $r^{-2/3}$ to obtain a compensated structure function in the inertial subrange (Rusello and Cowen, 2011). The dissipation rate is estimated by solving $\overline{D(z,r)r^{-2/3}\big|_{r_1}^{r_2}} = C_v^2\varepsilon^{2/3}$, where $r_1$ to $r_2$ is the range where the compensated structure function slope is closest to zero, and the overline denotes an average. Estimates are not calculated for depths with less than four points in the structure function, hence $r$ values ranged between 2 m and 7 m.

Uncertainties in TKE dissipation rates from the structure function fitting are calculated by propagating the uncertainty in the compensated structure function, such that:

$$\sigma_{\varepsilon_D} = \left(\frac{1}{Cv^2}\right)^{3/2} \frac{3}{2} \overline{D_{comp}}^{1/2} \sigma_{D_{comp}} \tag{5.15}$$

where $\sigma_{D_{comp}}$ corresponds to the standard deviation of the compensated structure function in the $r$ range used for the computations.

### *5.2.6 Data-products comparison*

Flow parameters obtained from the SWIFT data set are compared with those obtained from the ADV data set for the no-turbine river conditions in order to test the accuracy of the drifting method. Data are compared in terms of the velocity magnitude, pseudo turbulence intensity, turbulence intensity, and TKE dissipation rate. ADV-based flow parameters are obtained similarly to those from the SWIFT buoy, with the exception of TKE dissipation rate, which is estimated through the TKE spectra estimated from the ADV measurements following the method presented in (Guerra and Thomson, 2017). Figure 5.4 shows a comparison of the grid cell flow parameters (in blue), together with grid longitudinal averages (in grey) as longitudinal homogeneity was observed in the area covered by the ADV measurements.

Overall there is a good agreement between flow parameters obtained by the drifting method and the station-keeping method. An excellent agreement is observed for the gridded velocity magnitude between both measurement methods, with an $RSME = 0.16$ ms$^1$ between the values from the SWIFT and the values from the TT-ADV platform. Good linear agreement is found between the pseudo-turbulence intensity from both data sets, however the pseudo-turbulence intensity from the SWIFT data set is biased low. This bias is expected, since the pTI only considers a portion of the turbulence length-scales, while the turbulence intensity from TT-ADV is estimated by its usual definition and considers all turbulence length-scales in the along-channel direction. The plot in panel (c) shows turbulence

intensity estimated as in Eq. 5.12. Although significant scatter in the plot is observed, a linear trend and good agreement is found between the longitudinal averages. The dissipation rate estimates from the TT-ADV tends to be larger than those from the SWIFT. Despite the scatter in the comparison of these turbulence parameters, the average values obtained from the two methods lie in the same order of magnitude. This is notable, given the large dynamic range of this quantity in the natural environment.

Differences might be explained by uncertainties in the location of the measurements (from the GPS receivers), by remaining noise in the parameters estimates, and by differences in the calculation methods. Specifically, the station keeping provides highly populated time series of flow parameters within each grid cell, while the drifter methods provides spatial averages obtained through averages of non-uniformly sampled data.

## *5.3 Results: Wake Characterization*

The RivGen wake in the Kvichak river is characterized by the previously defined flow parameters obtained from the repeated SWIFT drifts. In general, the wake signal is strong and noticeable in all estimated flow parameters. In what follows the river original flow conditions and post-turbine deployment flow conditions are presented, always considering an operational RivGen. (The braked, non-operational RivGen will be considered in the Discussion.) Horizontal and longitudinal views of the river are presented, colored by the different mean flow and turbulence parameters. All horizontal view maps correspond to hub-height ($z = -2.5$m), while longitudinal views correspond to a streamline passing through the center of the turbine shown as a gray dotted-line in Figure 5.5b.

### *5.3.1 Mean flow parameters*

Figure 5.5a shows contours of grid-averaged velocity magnitude at hub-height for a undisturbed river conditions. The flow is stronger mid-river, reaching about 2.3 ms$^{-1}$ at the turbine location ($(x, y) = (0, 0)$), while slower flows are observed towards the river banks. When the river is undisturbed, strong lateral shear is observed at the cross-section corre-

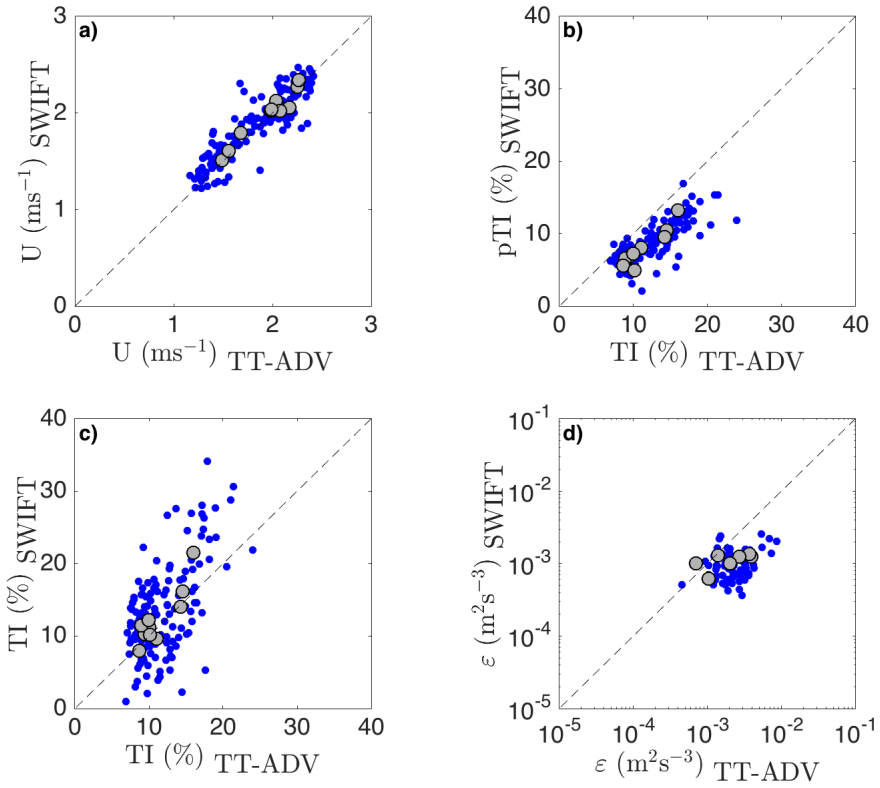


Figure 5.4: Comparison of flow parameters between ADV data (x-axis) and SWIFT data (y-axis) for the no turbine river condition: a) Velocity magnitude, b) pseudo-turbulence intensity, c) turbulence intensity, and d) TKE dissipation rape. Blue dots correspond to grid cell parameters, and gray larger dots correspond to longitudinal averages of grid cell values. Dotted line corresponds to the $y = x$ in all plots.

sponding with the turbine location, showing stronger flows towards the Igiugig side of the river (positive y-axis).

A plan view of velocity magnitude at hub-height while the turbine is operational is presented in Figure 5.5b. The turbine wake is observed immediately downstream of the turbine. Velocity magnitude is dramatically reduced, from $2.3\ \mathrm{ms}^{-1}$ to $1\ \mathrm{ms}^{-1}$ at the turbine location, and slower velocities are observed beyond 200 m downstream of the turbine. The wake remains mostly laterally constrained by the natural shape and direction of the river. Closer to the free-surface (above hub-height), the wake from the two turbine rotors can be distinguished, together with a reduced wake from the generator (located between the two rotors). These features are mixed about 40 m downstream of the turbine.

Figure 5.6 shows a longitudinal profile of the river colored by velocity magnitude. In its undisturbed state, classical boundary layer flow is observed in the river, with velocities increasing from the bottom towards the free-surface. The turbine wake has a rich longitudinal structure. The velocity decrease is observed to begin upstream of the turbine, as the river flow encounters an obstacle (the turbine) and slows down. On top of the turbine, faster flow is observed, consistent with acceleration on top of an obstacle. At this centerline longitudinal view, flow also accelerated below the turbine rotor, suggesting important vertical blockage effects. During the field measurements, a small free-surface decrease was observed at the turbine location, but is not captured by the vertical motion of the drifter.

Downstream of the turbine the wake expands vertically, reaching the free-surface about 35 m away from the turbine, where the wake is also observed in the surface velocities recorded by the GPS on board the SWIFT buoy.

Average uncertainty in the velocity estimates previous to turbine deployment is 1.3 $cms^{-1}$, and 1.2 $cms^{-1}$ when the turbine is operational.

In its natural state, the Kvichak river shows a vertical vorticity ($\omega_z$) of opposite direction along the Igiugig side of the river (positive y-axis), probably due to a lateral sharp change in bathymetry (Figure 5.7a. The underwater presence of the turbine has a strong impact on vertical vorticity, generating enough vertical vorticity to reverse its original sign right at the

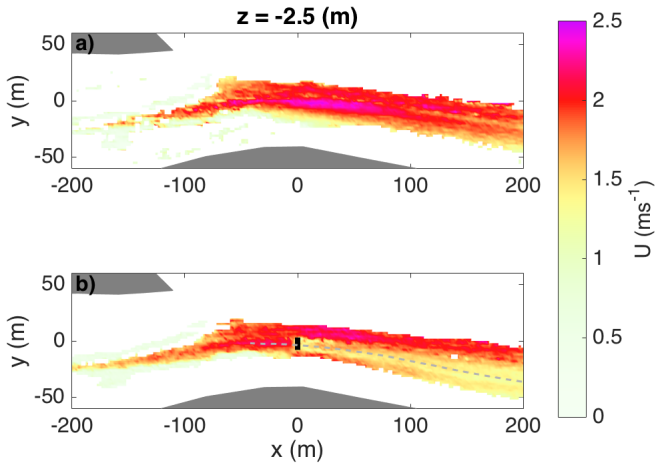


Figure 5.5: Plan view of horizontal velocity magnitude at hub-height (2.5 m below river free surface). a) Before turbine deployment, and b) when turbine is underwater and operational. Flow is from left to right in both plots. Grey dashed line in a) shows location of center streamline used for the longitudinal plots.

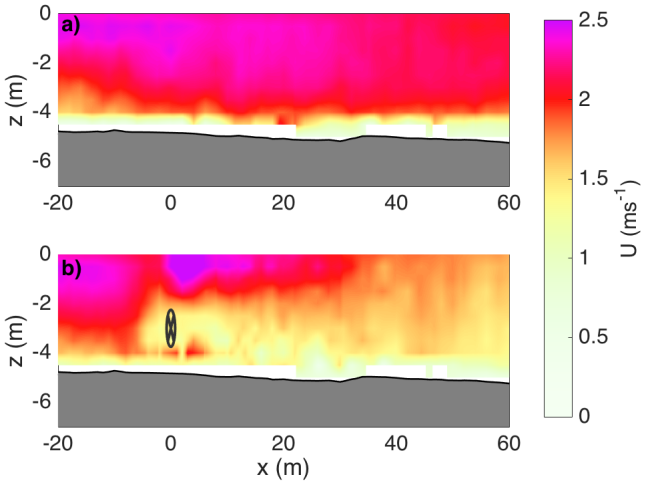


Figure 5.6: Longitudinal view of horizontal velocity magnitude along a center streamline (shown in Figure 5.5a). a) Before turbine deployment, and b) when turbine is underwater and operational. Flow is from left to right in both plots.

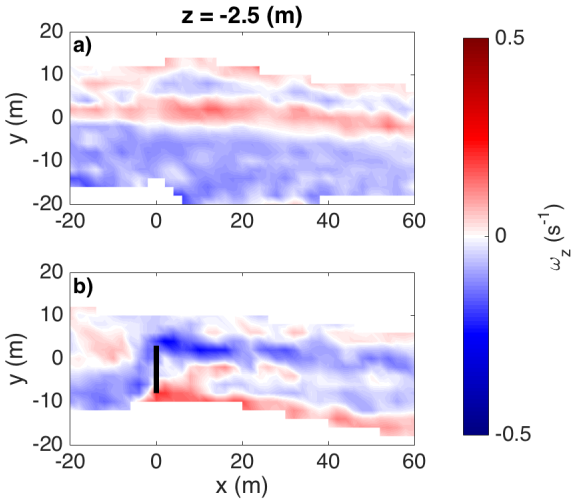


Figure 5.7: Plan view of vertical vorticity $\omega_z$ at hub-height (2.5 m below river free surface). a) Before turbine deployment, and b) when turbine is underwater and operational. Flow is from left to right in both plots.

lateral edges of the turbine, showing the expected behavior for an obstacle present in the flow (Figure 5.7b. Cross-stream vorticity, $\omega_y$, is shown in Figure 5.8. Baseline cross-stream vorticity shows a maximum near the bottom, consistent with bottom-induced vorticity. Similarly, when the turbine is underwater, cross-stream vorticity is enhanced on top and below the turbine, and vorticity direction is coincident with increased vorticity observed in flow passing around a cylinder. However, the wake vorticity magnitude is asymmetric, similar to what was observed in laboratory experiments by (Bachant and Wosnik, 2015). This asymmetry might be explained by blade rotation, which induces cross-stream vorticity of opposite direction. For the not-operational condition, cross-stream vorticity below the turbine, is of similar magnitude than cross-stream vorticity observed on top of the turbine. Average uncertainty is 0.04 $s^{-1}$ for the vertical vorticity and 0.1 $s^{-1}$ for the cross-stream vorticity.

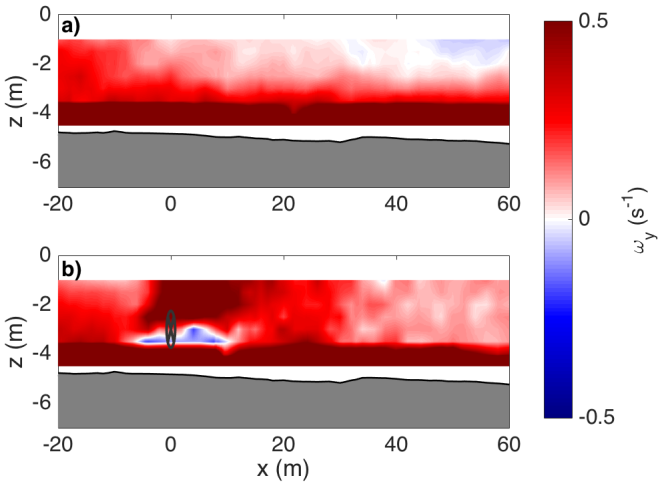


Figure 5.8: Longitudinal view of cross-channel vorticity $\omega_y$ along a center streamline (shown in Figure 5.5a). a) Before turbine deployment, and b) when turbine is underwater and operational. Flow is from left to right in both plots.

### *5.3.2 Turbulence Parameters*

Maps of turbulence intensity (TI) estimated as the ratio between the standard deviation of the along-channel turbulence fluctuations and the along-channel velocity are shown in Figures 5.9 and 5.10. Previous to turbine deployment, river TI is about 10% through the water column. Larger values of TI are observed near the bottom and in the shallower areas of the river, consistent with bottom-generated turbulence and slower flows. When the turbine is deployed, a region of elevated TI is observed in the area surrounding RivGen. TI increases more than 5 times from its original level due to both an increase in velocity fluctuations (up to 5 times) and a decrease in mean velocity. Unlike the mean velocity, the turbulence intensity, and the TKE, decrease rapidly downstream of the turbine, reaching a level similar to the natural river conditions. As shown in the plan-view plot of Figure 5.9b, the wake in terms of turbulence intensity decreases its width, concentrating the elevated TI towards mid-river.

The turbine effects are also observed in the Reynolds stresses, which are representative of

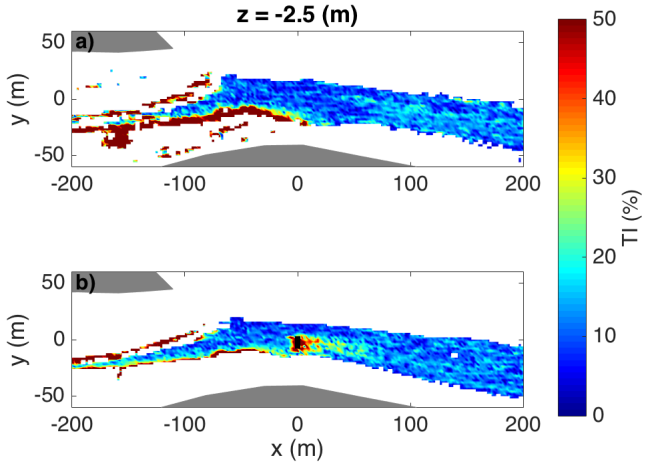


Figure 5.9: Plan view of total turbulence intensity at hub-height (2.5 m below river free surface). a) Before turbine deployment, and b) when turbine is underwater and operational. Flow is from left to right in both plots.

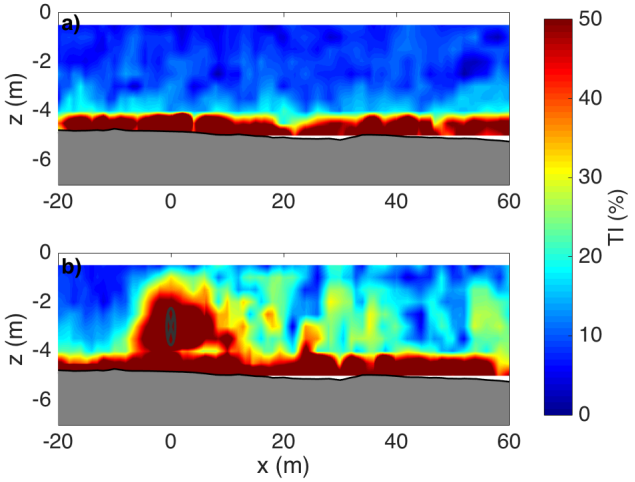


Figure 5.10: Longitudinal view of turbulence intensity along a center streamline (shown in Figure 5.5a). a) Before turbine deployment, and b) when turbine is underwater and operational. Flow is from left to right in both plots.

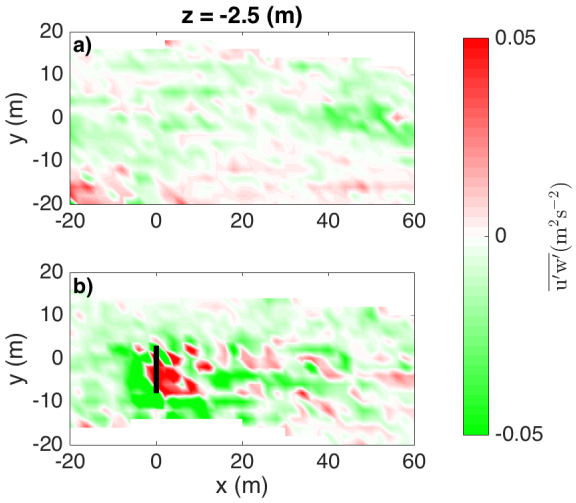


Figure 5.11: Plan view of $\overline{u'w'}$ Reynolds stress at hub-height (2.5 m below river free surface). a) Before turbine deployment, and b) when turbine is underwater and operational. Flow is from left to right in both plots.

turbulent momentum transport in the wake. Although estimates are noisy, elevated Reynolds stresses are observed up to 20 m downstream of the turbine, suggesting that turbulent transport is of importance in this region. Figures 5.11 and 5.12 show contour maps of the $\overline{u'w'}$ Reynolds stress. The regions of strong $\overline{u'w'}$ correspond with regions of velocity shear, which are caused by the decrease in velocity, and the net effect is consistent with higher TKE production.

TKE dissipation rate maps are shown in Figure 5.13 and 5.14. Right downstream of the turbine, TKE dissipation rate increases by at least a decade, consistent with the increase in turbulent kinetic energy. Along the center streamline, TKE dissipation rate is elevated through the entire water column. Although TKE dissipation rate decreases downstream of the turbine, it remains above baseline values at least for 60 m downstream of the turbine. Average uncertainty in the TKE dissipation rate estimates is 4.4 $\times 10^{-4}$ m$^2$s$^{-3}$ prior to turbine deployment, and it is 7.6 $\times 10^{-4}$ m$^2$s$^{-3}$ when the turbine is operational.

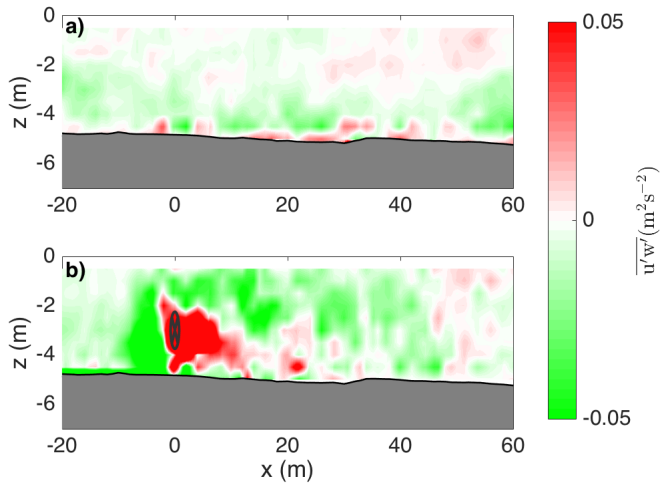


Figure 5.12: Longitudinal view of $\overline{u'w'}$ Reynolds stress along a center streamline (shown in Figure 5.5a). a) Before turbine deployment, and b) when turbine is underwater and operational. Flow is from left to right in both plots.

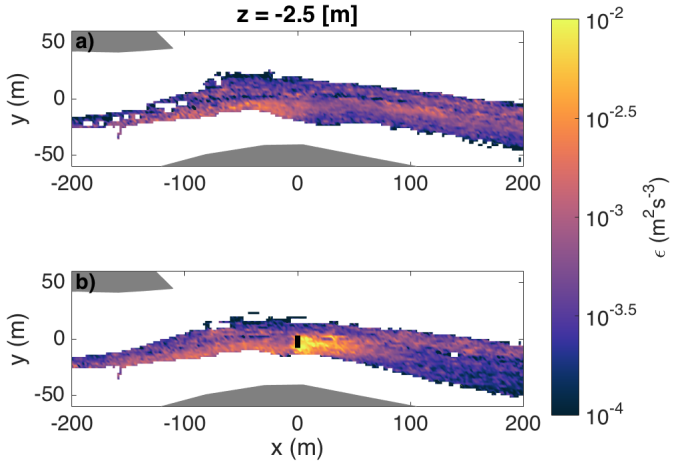


Figure 5.13: Plan view of TKE dissipation rate $\varepsilon$ at hub-height (2.5 m below river free surface). a) Before turbine deployment, and b) when turbine is underwater and operational. Flow is from left to right in both plots.

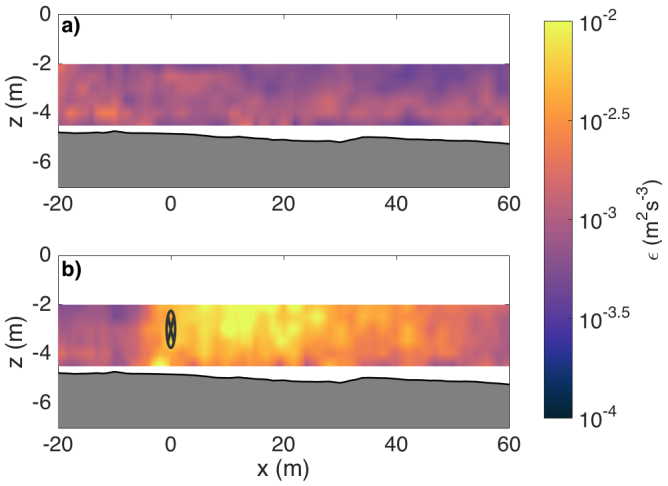


Figure 5.14: Longitudinal view of TKE dissipation rate $\varepsilon$ along a center streamline (shown in Figure 5.5a). a) Before turbine deployment, and b) when turbine is underwater and operational. Flow is from left to right in both plots.

## *5.4 Discussion*

### *5.4.1 Wake Evolution*

Figure 5.15 compares horizontal and vertical profiles of velocity at different distances from the turbine for the river in its natural conditions and while the turbine is operational. Horizontal profiles, taken at hub-height, show the strong wake signal from the two rotors and the generator. The profiles slowly mix horizontally, however the wake signal is still clearly observed about 50 m downstream of the turbine. Vertical profiles, taken along the center streamline shown in Figure 5.5b, show the sharp decrease in velocity at hub-height. Closer to the turbine, at $x = 2$ m, the velocity vertical profile shows the accelerated flow on top of the turbine. Vertically, the velocity profiles mix around 50 m downstream of the turbine, where typical boundary-layer profiles are observed. However, velocity remains slower when compared with the original vertical profiles due to energy extraction. These differences suggest that in this shallow river the velocity profiles homogenize faster vertically than horizontally, probably due to bottom-induced shear stress.

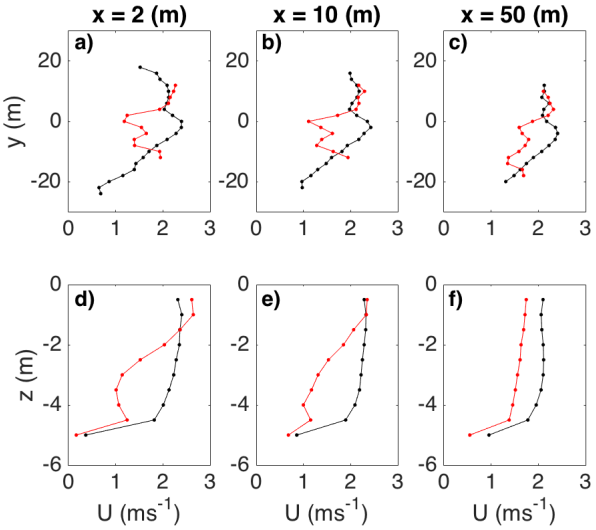


Figure 5.15: Horizontal and vertical profiles of velocity magnitude at three different locations downstream of the turbine. In black when there is no turbine in the water, and in red when the turbine is underwater and operational.

In what follows, the along-channel TKE ($\overline{u'^2}$) is used to study the wake evolution instead of turbulence intensity, since it provides information about the turbulence evolution rather than a ratio to the mean flow.

Longitudinal profiles of hub-height velocity ($U$), along-channel TKE ($\overline{u'^2}$), and TKE dissipation rate ($\varepsilon$), are presented in Figure 5.16. In these plots, the lines in dark colors represent an average between three streamlines: along the turbine port side, along the turbine center (shown in Figure 5.5), and along the turbine starboard side. Shadows represent the standard deviation from the averages between the three streamlines (a wider shadow indicates a large variation between streamlines).

Prior to turbine deployment, strong lateral shear was observed at hub-height at the turbine location, with stronger flow towards the turbine's starboard side and slower flow towards the turbine's port side. When the turbine is underwater and operational no significant lateral shear is observed just upstream of the turbine location. In the first 10 m of the wake, flow velocity is similar along the three streamlines. After 10 m downstream of the turbine, flow

at the center and starboard streamlines increases slightly more than at the port side, which might be explained by the stronger flows observed in the starboard side outside of the wake. However, the flow velocities do not recover to their baseline conditions along any of the three streamlines, and any increase in velocity is very small.

Along-channel TKE is observed to have a similar behavior along the three streamlines. Along-channel TKE begins to increase about 10 m upstream of the turbine, reaching a peak around turbine location. In the first 20 m downstream of the turbine a rapid along-channel TKE decrease is observed. TKE increases again along the starboard streamline around $x = 15$m, which might be explained by additional TKE being produced in the edges of the wake. TKE fluctuations further downstream might be explained by river bathymetric features.

TKE dissipation rate shows a behavior that consistent with the increase in TKE. It begins to increase at the same time as the turbulent kinetic energy, and it peaks about 5 m downstream of the turbine, however it slowly decreases towards its original level about 60 m downstream of the turbine.

From Figure 5.16, three dynamic regions can be distinguished through the turbine influence. From $x = -10$ m to the turbine location at $x = 0$ m, a bow wake is observed, where velocity is decreasing while TKE is rapidly increasing. This region is followed by a near wake up to about $x = 10$ m, where velocity continues to decrease followed by a small amount of recovery, while TKE decreases constantly, and TKE dissipation rate reaches its peak. A far wake is observed beyond $x = 10$ m, where both velocity and TKE do not change significantly; the velocity deficit persists, TKE remains slightly elevated with respect to its original level, and TKE dissipation rate continuously decreases. The far wake is an important demonstration that there is no true 'recovery' of the flow after this or any turbine, because kinetic energy has been extracted from the system. Of course, in some systems potential energy may be converted to kinetic energy, but the total energy is still reduced by extraction.

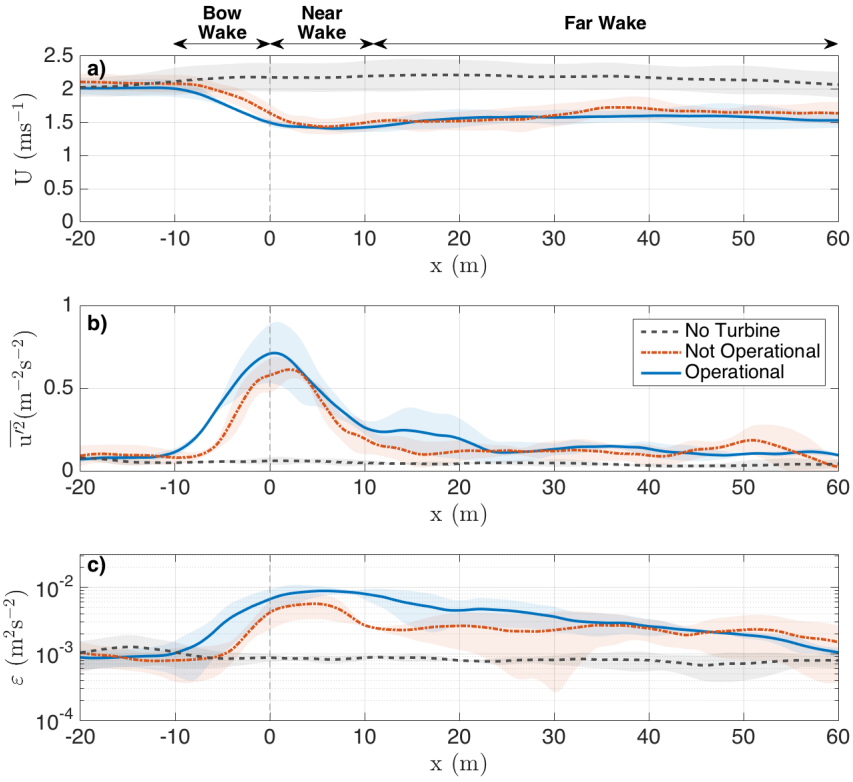


Figure 5.16: Hub-height longitudinal profiles of a) Velocity, b) Along-channel TKE, and c) TKE dissipation rate, for different river conditions. No turbine in gray, not-operational turbine in red, and operational turbine in blue. Darker lines correspond to a cross-stream average between three streamlines along the turbine wake (turbine port, center, and starboard sides). Lighter color shadows represent one standard deviation from the averages along the three streamlines.

### *5.4.2 Not operational turbine*

The wake observations shown in Section 5.3 correspond to the operational turbine conditions. During the life span of any hydrokinetic turbine it is expected that turbines will not be operational for periods of time, due to flow conditions not suitable for energy extraction, due to the presence of fauna, or due to maintenance, among other reasons. Here, the differences between the wake between the operational and not-operational turbine conditions are examined. Figure 5.16 presents longitudinal hub-height profiles for the three studied river conditions: no turbine, not-operational turbine, and operational turbine. When the turbine is not-operational the bow-wake shifts towards the turbine, and velocity reaches its minimum later in the profile, at $x = 8$ m instead of at $x = 2$ m for when the turbine is operational. Downstream, no significant differences are observed between both velocity profiles. A similar trend is observed in the TKE profiles, for the not-operational condition the TKE increases later in the profile, the TKE maximum is shifted downstream and it is of less magnitude than for the operational turbine condition. These differences are explained by both, turbine rotation and turbine energy extraction. Turbine rotation introduces additional turbulence and modifies the flow turbulence length-scales, resulting in a higher TKE level.

For the not-operational condition, the TKE dissipation rate also increases at the turbine location, after a small decrease about 10 m downstream of the turbine. On average, the dissipation rate remains elevated through the longitudinal extent of the wake, although large cross-wise variations are observed.

The small differences observed in the flow parameters between operational and not-operational conditions suggest that the turbine presence as a bluff body in the flow (as opposed to an extractor) is responsible for most of the hydrodynamic impacts in the Kvichak river.

### *5.4.3 Wake energy loss*

The Kvichak river naturally looses energy through the dissipation of turbulent kinetic energy into heat and sound. When the turbine is underwater and operational, it extracts energy from the mean flow and delivers it to the local Igiugig grid. At the same time more turbulence is generated in the river due to the presence of the turbine and blade rotation. As more turbulence is generated, an increase in TKE dissipation rate is observed in the wake of RivGen. Thus, the river is loosing additional energy through the turbine wake. Here, a volumetric TKE dissipation rate is calculated by multiplying the TKE dissipation rate, $\varepsilon$, by the water density, $\rho$, and then integrated over the river volume ($V$) to obtain the rate at which energy is being loss to turbulence as:

$$\text{Rate of Energy Loss} = \int_V \rho \varepsilon dV \tag{5.16}$$

Wake energy loss rate for the three studied conditions is presented in Table 5.3. Total energy loss rate is calculated in a volume that covers most of the turbine wake: between $x = 0$ m and $x = 60$ m, $y = -14$ m and $y = 14$ m, and from the bottom to the free-surface. Energy loss in the wake area doubles when the turbine is underwater, but not operational, and triplicates when the turbine is operational. Wake energy loss is comparable to what the turbine is delivering to the grid, which means that the river is loosing as much as two times the energy that is actually being delivered to the community. This amount of energy loss must be considered in the assessment of large hydrokinetic energy farms, as it indicates that a much larger effect on the hydrodynamics of a system exists in addition to what is being extracted by the turbine for electricity production alone.

## *5.5 Conclusions*

Detailed field measurements are used to analyze and understand the evolution of the wake of ORPC RivGen hydrokinetic turbine in the Kvichak river. A drifting Nortek Signature1000 5-beam acoustic Doppler current profiler is used to measure along-beam velocities at high

Table 5.3: River energy loss rates from turbine extraction and through dissipation of turbulent kinetic energy. Uncertainties are included for the turbulent dissipation values.

| Condition | No turbine | Not operational turbine | Operational turbine |
|---|---|---|---|
| Turbulent Dissipation (kW) | 3.43 ± 0.04 | 6.14 ± 0.16 | 10.93 ± 0.15 |
| Turbine Extraction (kW) | - | - | 9.9 |
| Total (kW) | 3.43 | 6.14 | 20.8 |

resolution following river streamlines. These observations are then used to construct a set of 3D flow conditions in the area surrounding the RivGen turbine for both before turbine deployment and while the turbine is underwater extracting energy.

In general, results show the expected wake characteristics of decreased velocities and increased turbulence downstream of the turbine, however unique wake features are observed.

A persistent velocity decrease is observed from 10 m upstream of the turbine extending more than 200 m downstream of the turbine (beyond the area covered measurements). Vertical blockage by the turbine is of importance, as the flow shows acceleration below and on top of the turbine. In terms of velocity, the wake slowly expands laterally, but rapidly expands vertically, reaching the free-surface about 35 m downstream of the turbine. The two-rotor wake signal is observed through the measurements in horizontal profiles of along-channel velocities, while vertically the velocity profiles homogenize about 50 m downstream of the turbine, while still experiencing lower velocities.

In terms of turbulence parameters, a rapid increase in turbulence intensity, and in turbulent kinetic energy, is observed, which peaks at the turbine location and then decreases downstream of the turbine. The increase in turbulence is consistent with an increase in TKE dissipation rate, which peaks later in the longitudinal profile and remains elevated through the extent of the measurements. Stronger Reynolds stresses near the turbine in areas of strong shear are also observed suggesting additional TKE production. In addition to velocity and turbulence, the turbine also affects river vorticity, inverting its natural direction to

be in accordance with vorticity generated by a bluff body in a rapid flow for both lateral and vertical vorticity.

Similar patterns of velocity and turbulence are observed in the wake of a non-operational RivGen, with no large differences between the decrease in velocity and increase in turbulence parameters. This comparison suggest that the main hydrodynamic effects in the Kvichak river are due to the presence of the turbine and not due to blade rotation.

The TKE dissipation rate parameter allows for the estimation of total energy being loss by turbulence in the wake region. For the operational condition, the river looses about 11 kW in the wake area, which is comparable to what the turbine is delivering to the grid ( 10 kW in average during the field measurements period).

This study provides the first comprehensive data set of a full-scale cross-flow turbine wake. The methods used in the field are proved to be efficient in characterizing the spatial extent of the wake, at least in system that is in steady state for long periods of time. The observations and analysis presented here serve as validation for numerical models and for future turbine array designs. But most importantly these results inform turbine designers, project developers, and decision makers about the environmental impacts of hydrokinetic energy extraction under real flow conditions.

All data sets produced for this paper are available in the US Department of Energy Marine and Hydrokinetic Energy data repository website [2].

[2]https://mhkdr.openei.org/home

# Chapter 6

# CONCLUSIONS

Through this thesis, new instruments and measurement techniques are applied to characterize in-stream energy resources, providing information about turbulent flows in both time and space at promising in-stream energy sites. The results and data collected contribute to the development of the in-stream energy industry. Measurements are useful for calibrating, improving, and validating numerical models that are used for resource assessment. Detailed turbulence observations provide important information for the design of hydrokinetic turbines and their performance evaluation. Wake analysis informs policy makers and stakeholders about the hydrodynamic impacts of in-stream energy extraction under real conditions, and its results are useful for designing arrays of turbines. In addition, the methods developed here are applicable to other research topics, such as mixing processes, sediment transport, contaminant dispersion, and the analysis of residual flows.

## *6.1 Main findings*

Chapter 2 presents the first detailed tidal energy resource characterization of Chacao Channel, Chile. Field measurements together with a numerical model of the area provide new knowledge about tidal currents, available power, and turbulence. Currents are strong and most of the time are above $1\text{ms}^{-1}$ at the measurements sites within the channel. However, significant spatial variability was observed using the station keeping technique at the Young site, where a $1\text{ms}^{-1}$ change occurs within 500 m offshore Carelmapu. These large gradients emphasize the need of detailed spatial observations for optimizing turbine array distribution and power extraction. At Chacao Channel, turbulence observations at a single location in the water column indicate that turbulence intensities range between 5 to 20%. A local sim-

plified TKE budget suggests a balance between TKE dissipation and production rates, and both quantities follow the theoretical scaling with $\overline{u}^3$. The FVCOM model of the channel correctly captures the local tidal dynamics and is useful for estimating power. However, the FVCOM results must be carefully used for turbine design (i.e. turbulence), as the model does not capture the anisotropic portion of the turbulent kinetic energy (Thyng et al., 2013).

Chapter 3 presents methods and validation tests for two new 5-beam ADCPs. The low Doppler noise of the Nortek Signature1000, even when sampling at low frequency (2 Hz), is comparable to the noise variance levels from an ADV ($\mathcal{O}(10^{-4})$ $\mathrm{m^2 s^{-2}}$). The instrument's low noise and high sampling frequency capability allow for the observation of the inertial subrange for several decades in both the frequency TKE spectrum and the second-order structure function of turbulence at these energetic sites. This portion of the energy cascade is usually obscured in measurements from regular ADCPs. Using the new inertial subrange observations, improved TKE dissipation rate estimates are now available in time through the water column. The inclusion of the vertical $5^{\mathrm{th}}$ beam gives a direct vertical velocity measurement, and admits the estimation of five, out of six, Reynolds stresses. Hence, improved TKE production rates estimates are now available from these instruments (as more terms can be included). The results demonstrate the applicability of these profilers for measuring turbulence, even at sites with low turbulence levels. All the methods applied to these turbulence measurements are implemented in Matlab and are available for future use and collaboration in GitHub at `https://github.com/mguerrap/5Beam-Turbulence-Methods`.

Chapter 4 presents Long-term observations of tidal currents from ferry-mounted ADCPs. Strong quality control was key for this data set, as ferry speed and biofouling significantly reduce the quality of the data. However, tidal currents are still well captured by these measurements. New maps of main tidal harmonics are now available across and through the depth of Admiralty Inlet, which are useful for tidal energy resource estimations, navigation safety, and even for residual flow estimations. Mid channel, away from the inlet boundaries, tidal current harmonics agree well with those obtained from fixed measurements. Closer to shore, especially in areas with large spatial variability in the tidal currents, results do not

agree well. This is explained by the grid applied to the measurements, which obscures sharp gradients in the tidal currents in the along-channel direction. Ferry-based data is also used for preliminary estimations of residual flows across the inlet. These results suggest that this data set is suitable for estimating the spatial distribution of residual currents, but not their temporal variations, which are related to water quality variations within Puget Sound.

Chapter 5 presents the wake of a full-scale cross-flow hydrokinetic turbine and is the culmination of the methods developed in the preceding chapters. Repeated drifts using a Nortek Signature1000 5-beam acoustic Doppler current profiler successfully capture the spatial distribution of the mean flow velocities and turbulence statistics in a steady-state river. The method efficiently maps the extent and evolution of the turbine wake. The wake shows expected behavior, with lower velocities and increased turbulent kinetic energy downstream of the turbine. However, the velocity decrease observed in the wake was persistent beyond the extent of the measurements downstream of the turbine. This finding suggests that there is no wake recovery. Kinetic energy has been removed from the river, and momentum entrainment from the undisturbed flow is not enough to elevate the mean flow velocity downstream of the turbine. In contrast, TKE and TKE dissipation rates do show recovery. The turbulence rapidly increases at the turbine location and then continuously decreases downstream of the turbine, almost returning to original values. Finally, the wake energy loss is found to be comparable to what is being extracted by the turbine.

## *6.2 Implications and Future Directions*

For energy resource characterization, the conventional paradigm has been to make measurements at a single point for long periods of time. ADCPs are used for obtaining mean flow velocities and some turbulence parameters, which are based on the variance of the along-beam velocities. ADVs have been the preferred instrument for turbulence measurements, and compliant moorings have been designed to position ADVs at the desired water depth. Such ADV deployments have required additional motion corrections based on data from inertial motion units (IMU). This new work has demonstrated that the new fast-sampling, low-noise Nortek Signature1000 profiler can be used to measure turbulence through the water column with high quality, similar to that from an ADV. Like a regular ADCP, the instrument can be deployed up-looking or down-looking, and the integration of an IMU makes it suitable for mooring or buoy deployment. Perhaps, these new generation profilers will replace ADVs for turbulence measurements of relevance to in-stream energy, as their measurements are practically equivalent as having several ADVs distributed through the water column, allowing for an additional characterization of turbulence in space. However, if detailed turbulence measurements are needed at an specific point or very close to a boundary (e.g. near the bottom for estimating bed stresses), an ADV might still be the instrument of choice. At sites where sharp horizontal gradients occur at scales smaller than the beam divergence, the homogeneity assumption used in ADCP velocity and turbulence estimates might not hold. In such cases, the additional vertical beam becomes useful for turbulence measurements, as it provides high-frequency measurements of the vertical velocities from which at least TKE spectra and TKE dissipation rates can be obtained.

The repeated drifting method, used for wake characterization, has been proven successful to map the flow in space and to obtain robust turbulence statistics. Here, the drifting measurements were organized into a uniform horizontal grid assuming steady state conditions. However, many hydrokinetic turbines (or arrays) are expected to be deployed in tidal channels, and field measurements will be needed to map both the ambient flow and the wake

of these turbines under *unsteady* flow conditions. The drifting method might be suitable for these environments as well, but the short windows (5-10 minutes) of stationarity will be a challenge. Tidal cycles are periodic, hence drifts occurring at the same tidal stage are expected to be comparable, although many more drifts will be needed to map each tidal cycle, and many more to map seasonal variations. (Note that this method is not intended for mapping long-term variability in the tidal currents). For applying this particular method, previous knowledge about the currents, streamlines, and wake extent would be useful (e.g. from numerical models). How the currents change in time and how long do stationary conditions hold will be important for planning the drifts. Knowledge about surface streamlines and about the wake extent for different mean flows would help plan drifting trajectories, release location, and drift concentration. Releasing multiple drifters at the same time would be advantageous for getting robust statistics in less time.

Stationary fixed instruments and a controlled spatial survey would compliment such a mapping of unsteady currents. Similarly to the large scale ferry mapping or to the station keeping technique, repeated transects using acoustic instruments mounted on a vessel or autonomous vehicle could be used to rapidly map the flow across the wake for different mean flow conditions. Again, some a priori knowledge of the wake's tridimensional extent would be necessary for planning the location of instruments and transects.

All data collected and codes developed through this thesis are publicly available on different online platforms [1] [2] [3]. These data sets can be used for calibrating and validating hydrodynamic numerical models used for in-stream resource characterization, turbine wakes, and other oceanographic applications. Specifically, obtained turbulence parameters, such as total TKE, TKE dissipation rates, Reynolds stresses, and TKE spectra, are useful for the development and improvement of turbulence closure models (Thyng et al., 2013). Spatially

---

[1] 5-Beam ADCP turbulence methods: `https://github.com/mguerrap/5Beam-Turbulence-Methods`

[2] Turbine wake dataset: `https://mhkdr.openei.org/submissions/248`

[3] Ferry-based ADCP dataset: `http://www.apl.washington.edu/project/project.php?id=ferries_for_science`

distributed turbulence parameters can improve turbulence models used in turbine design. For example, turbulence parameters from the 5-beam Nortek Signature1000 data sets can be used to characterize the spatial distribution of turbulence over the swept area of a turbine. Baseline and wake data collected in the Kvichak river is tremendously helpful for defining the location, estimating the performance, and anticipating the environmental effects, of multiple turbines to be deployed at this site in 2019.

### *6.2.1 Wake losses and the total power removed from a hydrokinetic resource*

The large amount of energy lost through turbulence in the wake of an hydrokinetic turbulence that wake losses should not be neglected. However, wake energy losses are not typically considered in large-scale resource assessment models. For example, maximum power extraction estimations presented in the U.S. Tidal Energy Atlas are based on the model from Garrett and Cummins (2005), which does not consider energy losses through wake mixing. If the wake energy dissipation is as significant as the one found in the wake analysis presented here, these maximum extractable power estimates could be reduced by half (specifically at sites with similar blockage ratio). Similarly, oceanographic numerical models used for the analysis of hydrodynamic effects of large-scale energy extraction typically incorporate the turbines as an additional bed friction term (Neill et al., 2012). Again, this term represents the bulk-effects of energy extraction by turbines, but does not account for any wake effects downstream of turbines (Garrett and Cummins, 2007; Neill et al., 2012). The estimated environmental impacts of in-stream energy extraction will increase with this additional energy loss, in particular those impacts related to transport and mixing mechanisms.

The bulk representation of energy extraction used in models could be improved by incorporating the wake effects. Typically, the local power extracted by a turbine, $P_t$, is related to a reference inflow energy flux by a mechanical efficiency known as coefficient of performance, $C_p$. Perhaps the wake energy loss, $P_w$, can also be related to the inflow energy flux by a coefficient $C_\varepsilon$, such that a simple representation of the total energy removal, $P_{removed}$ would be written as follows:

$$P_{removed} = P_t + P_w \tag{6.1}$$

$$P_{removed} = C_p \frac{1}{2}\rho U^3 + \iiint \rho\varepsilon \, dx \, dy \, dz \tag{6.2}$$

$$P_{removed} \stackrel{?}{=} (C_p + C_\varepsilon)\frac{1}{2}\rho U^3 \tag{6.3}$$

where $U$ is a reference inflow velocity and $\rho$ is the water density. This idea cannot be tested using the wake data collected in this thesis, as only one inflow condition was studied (i.e., the river at steady state only had one value of the upstream $U$). However, this could be investigated using energy loss estimates from the wake of a turbine operating in a tidal channel (with a range of upstream speeds $U$ throughout a tidal cycle).

### *6.2.2 Wake measurements under unsteady flow conditions*

The work of this thesis will be followed by a post-doctoral fellowship where the drifting method will be applied to mapping the wake of a hydrokinetic turbine in a tidal channel. Here, a measurement plan for characterizing this wake is proposed.

The objectives of this measurement plan are to determine the region of turbine influence in terms of mean-flow velocity and turbulence for different tidal stages, and to estimate the velocity deficit and turbulence increase within the wake. Other questions to be addressed are related to the effects of a reversing tidal flow over the turbine wake, and if this reversed wake has an effect on turbine performance. A schematic of the measurement plan is presented in Figure 6.1.

The field measurements will consider the use of mobile platforms for spatial flow mapping, and the use of fixed instruments for obtaining time-series of velocities and robust turbulence statistics upstream and downstream of the turbine. Instruments needed include: i) At least one drifting platform equipped with a down-looking fast-sampling acoustic Doppler current profiler, such as the Nortek Signature, plus GPS for location and drifting velocity estimations; ii) One controlled vessel equipped with a down-looking fast-sampling acoustic

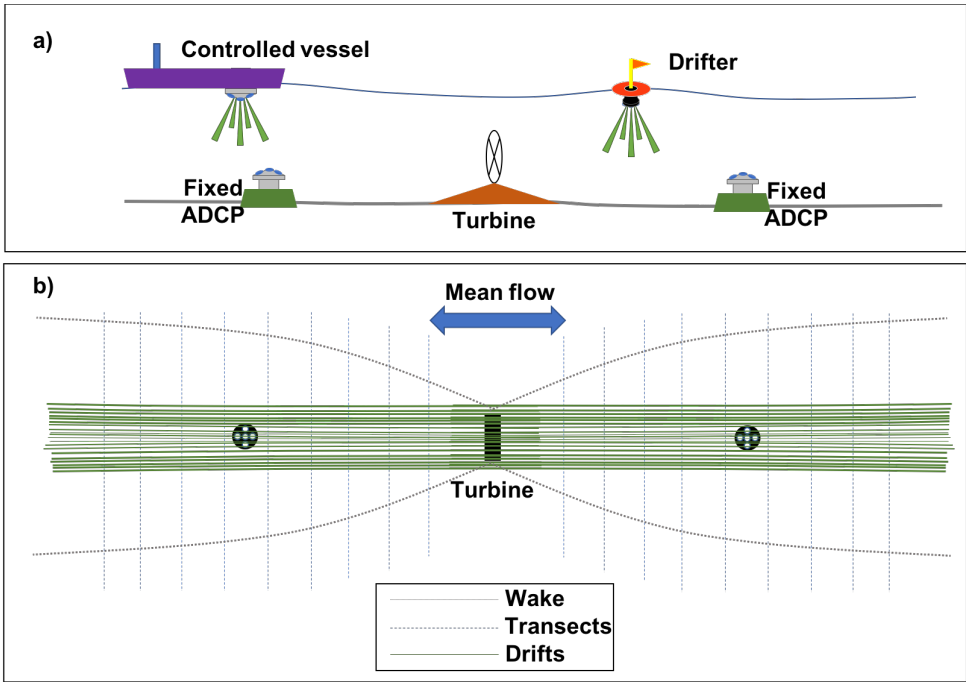


Figure 6.1: Measurement plan schematic for the wake of a bottom-mounted hydrokinetic turbine under *unsteady* flow conditions: a) side view through the water column, and b) plan view of drifting and transect coverage (not to scale).

Doppler current profiler; and iii) Two acoustic Doppler current profilers to be mounted up-looking in fixed locations. The range of the acoustic profilers should be defined considering the water depth and turbine hub-height depth. For reference, the Nortek Signature1000 has a 30 m depth range and can sample at 8Hz when using all 5-beams, while the Nortek Signature500 has a 70 m range, but can only sample at 4 Hz when using all five beams.

The wake will be characterized in space for different mean velocities during ebb and flood tides. Normally, stationary conditions at tidal channels hold for 5 to 10 minutes (McCaffrey et al., 2015). Drifts and controlled transects will be conducted at different tidal current conditions ranging from the minimum cut-in speed for the turbine to be operational (e.g. 0.5 $ms^{-1}$) up to the maximum spring tide velocity (e.g. 3 $ms^{-1}$). All data from mobile platforms will be organized in a three dimensional grid in space (both horizontally and vertically to account for tidal elevation changes). The grid definition must consider the beam-spread of

the profiling instruments, which gives beams spreads that are similar to water depths for typical 50 degree spread between opposing slanted beams. Thus, the horizontal grid cannot have resolution greater than the water depth. Within each spatial grid, data will also be organized by tidal stage in 0.5 $ms^{-1}$ tidal current bins. Bottom-fixed instruments will provide concurrent time-series of inflow and wake conditions through the water column at a single location. These data will be used as tidal stage reference for the drifting and transect data organization and to validate the spatial mapping.

Drifts should aim to cover the extent of the wake in the along-channel direction, while transects should aim at assessing the cross-channel extent of the wake. Both approaches will provide data through the water column. Wake estimations from numerical models will be considered to pre-define the distances to be covered by these mobile platforms. To determine the number of drifts and transects to be conducted, a compromise on time and space resolution will be needed to define a feasible plan. If the same time resolution as in the steady state wake study presented in this thesis is desired ($\sim$ 200 drifts per one mean flow condition), thousands of drifts would be needed. Here an idealized drifting plan is proposed.

If drifts need to cover at least 5 diameters upstream of the turbine and at least 15 turbine diameters downstream of the turbine, and if the turbine is 16 m in diameter (similar to an OpenHydro turbine recently deployed in Minas Passage, Nova Scotia), drifts would need to cover about 400 m (80 m upstream and 320 m downstream of the turbine). Considering the time to drift 400 m at each tidal current stage, and estimating 5 minutes per drift recovery and redeployment, approximately 70 drifts could be conducted in a 12 hour undisturbed tidal cycle (using only one drifter, non-stop). An schematic of this idealized drift schedule and a corresponding histogram of number of drifts per 0.5 $ms^{-1}$ velocity bin is shown in Figure 6.2. Under this hypothetic schedule, about 12 drifts could be conducted during the stronger currents, while only 2 drifts covering the same distance could be conducted during weaker currents. However, slower drifts will provide better spatial resolution if the same sampling rate is used, which will also be the case under wake conditions. If under real conditions, only half of the drifts can be conducted, in a 14 day field campaign, about 60 drifts would be

conducted for the stronger flows, and about 20 would be conducted for the slower flows. A similar analysis for defining transect extension, concentration, and timing can be performed when specifics about the vessel to be used are available. Of course, as drifts and transects are performed, knowledge about the drift trajectories and true wake extension is improved, which will contribute to the optimization of drifts extent, duration, and concentration. Other challenges include the tidal currents asymmetry and how the turbine rotates to face the flow.

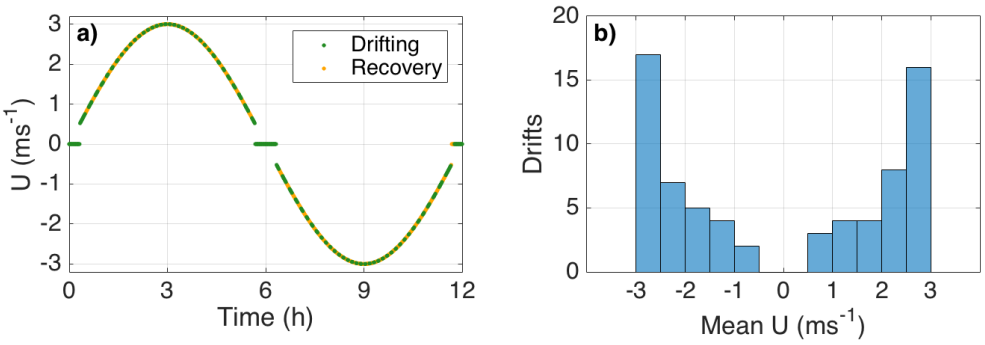


Figure 6.2: Idealized drift schedule for a 12 hour tidal current cycle: a) Drifting (in green) and recovery (in yellow) intervals during a 12 hour tidal cycle, and b) Histogram of number of drifts during a 12 hour tidal cycle

For the case of a turbine mounted on a floating structure (e.g. Sustainable Marine Energy PLAT-I[4]), the same measurement plan could be used. However, drifting release location and trajectories should also consider interference and collision risk with the turbine's surface expression.

These measurements could also be complemented by applying the station keeping technique with either a down-looking current profiler and/or an ADV mounted on a torpedo. If wake surface features are distinguished from the sea-surface, drone based images can assist in the estimation of the region of turbine influence and even provide information about surface turbulent velocities. This would be particularly applicable to floating platform turbine cases.

The multiple methods developed and tested in this thesis expand the traditional mea-

[4]https://sustainablemarine.com/

surements used for in-stream energy resource characterization and to study turbine wakes. The results of this investigation suggest that a variety of instruments, platforms, and data analysis techniques, that complement each other, are required to accurately map ambient and wake turbulent flows in time and in space.

# BIBLIOGRAPHY

B. Polagye and J. Thomson. Tidal energy resource characterization: methodolgy and field study in Admiralty Inlet, Puget Sound, USA. *Proceedings of the Institution of Mechanical Engineers, Part A: Journal of Power and Energy*, 227(3):352–367, 2013.

R. Dewey and S. Stringer. Reynolds stresses and turbulent kinetic energy estimates from various adcp beam configurations: Theory. *Journal of Physical Oceanography*, pages 1–35, 2007.

M. Stacey, S. Monismith, and J. Burau. Measurements of reynolds stress profiles in unstratified tidal flow. *Journal of Geophysical Research*, 104:10935–10949, 1999.

M. Lewis, S. Neill, P. Robins, and M. Hashemi. Resource assessment for future generations of tidal-stream energy arrays. *Energy*, 83:403–415, 2015.

T. Blackmore, L. Myers, and A. Bahaj. Effects of turbulence on tidal turbines: Implications to performance, blade loads, and condition monitoring. *International Journal of Marine Energy*, 14:1–26, 2016.

L. Chamorro, C. Hill, S. Morton, C. Ellis, R. Arndt, and F. Sotiropoulos. On the interaction between a turbulent open channel flow and an axial-flow turbine. *Journal of Fluid Mechanics*, 716:658–670, 2013a.

C. Hill, M. Musa, L. Chamorro, C. Ellis, and M. Guala. Local scour around a model hydrokinetic turbine in an erodible channel. *Journal of Hydraulic Engineering*, 140(8): 04014037, 2014.

R. Cavagnaro. Impact of turbulence on the control of a hydrokinetic turbine. In *International Conference on Ocean Energy, Halifax, Canada*, 2014.

G. Cada, J. Ahlgrimm, M. Bahleda, T. Bigford, S. Stavrakas, D. Hall, R. Moursund, and M. Sale. Potential impacts of hydrokinetic and wave energy conversion technologies on aquatic environments. *Fisheries*, 32(4):174–181, 2007.

G. Boehlert and A. Gill. Environmental and ecological effects of ocean renewable energy development: a current synthesis. *Oceanography*, 23(2):68–81, 2010.

B. Polagye, B. Van Cleve, A. Copping, and K. Kirkendall. Environmental effects of tidal energy development: Proceedings of a scientific workshop march 22-25, 2010. Technical report, US National Oceanographic and Atmospheric Administration, 2011.

Ministerio de Energía de Chile. Energy 2050 - Chile Energy Policy. Technical report, Ministerio de Energía de Chile, 2015.

P. Fraenkel. Power from marine currents. *Proceedings of the Institution of Mechanical Engineers, Part A: Journal of Power and Energy*, 216(1):1–14, 2002.

M Ishak Yuce and Abdullah Muratoglu. Hydrokinetic energy conversion systems: A technology status review. *Renewable and Sustainable Energy Reviews*, 43:72–82, 2015.

E. Segura, R. Morales, and J. Somolinos. A strategic analysis of tidal current energy conversion systems in the european union. *Applied Energy*, 212:527–551, 2018.

C. Garrett and P. Cummins. The power potential of tidal currents in channels. *Proceedings of the Royal Society of London A: Mathematical, Physical and Engineering Sciences*, 461 (2060):2563–2572, 2005.

EPRI. Assessment and mapping of the riverine hydrokinetic resource in the continental united states. Technical report, Electric Power Research Institute (EPRI), Palo Alto, CA (United States), 2012.

K. Haas, H. Fritz, S. French, B. Smith, and V. Neary. Assessment of energy production potential from tidal streams in the united states. *Final Project Report, DE-FG36-08GO18174, Georgia Tech Research Corporation*, 2011.

T. Burton, D. Sharpe, N. Jenkins, and E. Bossanyi. *Wind energy handbook*. John Wiley & Sons, 2001.

C. Garrett and P. Cummins. The efficiency of a turbine in a tidal channel. *Journal of fluid mechanics*, 588:243–251, 2007.

Pacific Northwest National Laboratory Tethys. Strangford Lough - MCT. `https://tethys.pnnl.gov/annex-iv-sites/strangford-lough-mct-seagen`, 2016.

SIMEC Atlantis Energy. MEYGEN Tidal Stream Project. `https://simecatlantis.com/projects/meygen/`, 2018.

Scotrenewables. SR200. `http://www.scotrenewables.com/technology-development/sr2000`, 2018.

Naval Energies OpenHydro. OpenHydro Projects. `http://www.openhydro.com/Projects`, 2018.

Ocean Renewable Power Company. ORPC RivGen power system delivers power to remote Alaskan village grid. `http://www.orpc.co/media/press-release/orpc\%E2\%80\%99s-rivgen\%C2\%AE-power-system-delivers-power-to-remote-alaskan-village-grid?Date=30-Jul-2015`, 2015.

Verdant Power. The RITE Project. `https://www.verdantpower.com/rite`, 2012.

J. Thomson, B. Polagye, V. Durgesh, and M. Richmond. Measurements of turbulence at two tidal energy sites in Puget Sound, WA. *IEEE Journal of Oceanic Engineering*, 37(3): 363–374, 2012.

M. Cáceres, A. Valle-Levinson, and L. Atkinson. Observations of cross-channel structure of flow in an energetic tidal channel. *Journal of Geophysical Research: Oceans (1978–2012)*, 108(C4), 2003.

C. Aiken. Barotropic tides of the Chilean Inland Sea and their sensitivity to basin geometry. *Journal of Geophysical Research: Oceans (1978–2012)*, 113(C8), 2008.

J. Cruz, M. Thomson, E. Stavroulia, and R. Rawlinson-Smith. Preliminary site selection-chilean marine energy resources. report for the inter-american development bank. Technical report, Garrad Hassan and Partners, 2009.

K. McCaffrey, B. Fox-Kemper, P. Hamlington, and J. Thomson. Characterization of turbulence anisotropy, coherence, and intermittency at a prospective tidal energy site: Observational data analysis. *Renewable Energy*, 76:441–453, 2015.

W. Deppe, J. Thomson, B. Polagye, and C. Krembs. Predicting deep water intrusions to puget sound, WA (USA), and the seasonal modulation of dissolved oxygen. *Estuaries and Coasts*, 41(1):114–127, 2018.

M. Palodichuk, B. Polagye, and J. Thomson. Resource mapping at tidal energy sites. *Journal of Oceanic Engineering*, 38(3):433–446, July 2013.

S. Pope. *Turbulent flows*. IOP Publishing, 2001.

P. Kundu, I. Cohen, and R. Dowling. *Fluid Mechanics, 5th Edition*. Elsevier, Oxford, UK, 2008.

L. Richardson. Weather prediction by numerical methods, 1922.

A. Kolmogorov. Dissipation of energy in the locally isotropic turbulence. *Dokl. Akad. Nauk SSR*, 30:301–305, 1941.

Z. Yang and A. Copping. *Marine Renewable Energy: Resource Characterization and Physical Effects*. Springer, 2017.

H. Burchard, P. Craig, J. Gemmrich, H. van Haren, P Mathieu, M. Meier, W. Smith, H. Prandke, T. Rippeth, E. Skyllingstad, et al. Observational and numerical modeling methods for quantifying coastal ocean turbulence and mixing. *Progress in Oceanography*, 76(4):399–442, 2008.

J. Richard, J. Thomson, B. Polagye, and J. Bard. Method for identification of doppler noise levels in turbulent flow measurements dedicated to tidal energy. *International Journal of Marine Energy*, 3:52–64, 2013.

Y. Lu and R. Lueck. Using a broadband adcp in a tidal channel. part ii: Turbulence. *Journal of Atmospheric and Oceanic Technology*, 16(11):1568–1579, 1999.

P. Wiles, T. Rippeth, J. Simpson, and P. Hendricks. A novel technique for measuring the rate of turbulent dissipation in the marine environment. *Geophysical Research Letters*, 33 (21), 2006.

S. Harding, L. Kilcher, and J. Thomson. Turbulence measurements from compliant moorings - part I: motion characterization. *Journal of Atmospheric and Oceanic Technology*, 2017.

L. Kilcher, S. Harding, J. Thomson, and S. Nylund. Turbulence measurements from compliant moorings - part II: motion correction. *Journal of Atmospheric and Oceanic Technology*, 2017.

R. Raineri. Chile: where it all started. *Electricity Market Reform: An International Perspective*, pages 77–108, 2006.

C. Legrand. *Assessment of tidal energy resource: Marine renewable energy guides*. European Marine Energy Centre, 2009.

J. Goundar and R. Ahmed. Marine current energy resource assessment and design of a marine current turbine for fiji. *Renewable Energy*, 65:14–22, 2014.

N. Carpman and K. Thomas. Tidal resource characterization in the folda fjord, norway. *International Journal of Marine Energy*, 13:27–44, 2016.

M. Thiébaut and A. Sentchev. Tidal stream resource assessment in the dover strait (eastern english channel). *International Journal of Marine Energy*, 16:262–278, 2016.

Z. Yang, T. Wang, and A. Copping. Modeling tidal stream energy extraction and its effects on transport processes in a tidal channel and bay system using a three-dimensional coastal ocean model. *Renewable Energy*, 50:605 – 613, 2013.

H. Tang, S. Kraatz, K. Qu, G. Chen, N. Aboobaker, and C. Jiang. High-resolution survey of tidal energy towards power generation and influence of sea-level-rise: A case study at coast of new jersey, {USA}. *Renewable and Sustainable Energy Reviews*, 32:960 – 982, 2014.

C. Garrett and P. Cummins. Limits to tidal current power. *Renewable Energy*, 33(11): 2485–2490, 2008.

P. Pyakurel, J. VanZwieten, M., and N. Xiros. Numerical modeling of turbulence and its effect on ocean current turbines. *International Journal of Marine Energy*, 17:84 – 97, 2017.

T. Blackmore, W. Batten, and A. Bahaj. Influence of turbulence on the wake of a marine current turbine simulator. In *Proceedings of the Royal Society of London A: Mathematical, Physical and Engineering Sciences*, volume 470, page 20140331. The Royal Society, 2014.

E. Osalusi, J. Side, and R. Harris. Structure of turbulent flow in emec's tidal energy test site. *International Communications in Heat and Mass Transfer*, 36(5):422–431, 2009.

S. Pantoja, J. Iriarte, and G. Daneri. Oceanography of the chilean patagonia. *Continental shelf research*, 31(3):149–153, 2011.

R. Hucke-Gaete, L. Osman, C. Moreno, K. Findlay, and D. Ljungblad. Discovery of a blue

whale feeding and nursing ground in southern chile. *Proceedings of the Royal Society of London B: Biological Sciences*, 271(Suppl 4):S170–S173, 2004.

B. Vernazzani, C. Carlson, E. Cabrera, and R. Brownell Jr. Chilean blue whales off isla grande de Chiloe, 2004-2010: distribution, site-fidelity and behaviour. *J. Cetacean Res. Manage*, 12(3):353–360, 2012.

J.C. Castilla, P. Manríquez, E. Fica, and V. Ortiz. Proyecto fondef d09i1052: Uso del espacio marítimo: situaciń pesquero-acuícola en la zona de estudio en el canal de chacao. *Unpublished*, pages 1–75, 2012.

J. Thomson et al. Tidal turbulence spectra from a compliant mooring. In *Proceedings of the 1st Marine Energy Technical Symposium (METS), Washington D.C.*, April 2013.

Ch. Chen, H. Liu, and R. Beardsley. An unstructured, finite-volume, three-dimensional, primitive equation ocean model: application to coastal ocean and estuaries. *Journal of Atmospheric and Oceanic Technology*, 20:159–186, 2003.

C. Chen, R. Beardsley, G. Cowles, J. Qi, Z. Lai., G. Gao, D. Stuebe, Q. Xu, P. Xue, J. Ge, et al. *An Unstructured-grid, Finite-volume Community Ocean Model: FVCOM User Manual*. SMAST/UMASSD Tech., 3rd edition, 2013.

G. Egbert and S. Erofeeva. Efficient inverse modeling of barotropic ocean tides. *Journal of Atmospheric and Oceanic Technology*, 19(2):183–204, 2002.

G. Mellor and T. Yamada. Development of a turbulence closure model for geophysical fluid problems. *Reviews of geophysics and space physics*, 20(4):851–875, 1982.

J. Smagorinsky. General circulation experiments with the primitive equations: I. The basic experiment. *Monthly weather review*, 91(3):99–164, 1963.

R. Pawlowicz, B. Beardsley, and S. Lentz. Classical tidal harmonic analysis including error estimates in matlab using t_tide. *Computers & Geosciences*, 28(8):929–937, 2002.

D. Goring and V. Nikora. Despiking acoustic doppler velocimeter data. *Journal of Hydraulic Engineering*, 128(1):117–126, 2002.

B. Brumley, R. Cabrera, K. Deines, and E. Terray. Performance of a broad-band acoustics Doppler current profiler. *Journal of Oceanic Engineering*, 16(4), 1991.

K. Thyng, J. Riley, and J. Thomson. Inference of turbulence parameters from a roms simulation using the k-$\varepsilon$ closure scheme. *Ocean Modelling*, 72:104–118, 2013.

C. Bassett, J. Thomson, and B. Polagye. Sediment generated noise and bed stress in a tidal channel. *Journal of Geophysical Research: Oceans*, 118:1–17, 2013.

V. Durgesh, J. Thomson, M. Richmond, and B. Polagye. Noise correction of turbulent spectra obtained from acoustic doppler velocimeters. *Flow Meas. Instrum.*, 37:29–41, 2014.

J. McMillan, A. Hay, R. Lueck, and F. Wolk. Rates of dissipation of turbulent kinetic energy in a high reynolds number tidal channel. *Journal of Atmospheric and Oceanic Technology*, 33(4):817–837, 2016.

J. McMillan and A. Hay. Spectral and structure function estimates of turbulence dissipation rates in a high-flow tidal channel using broadband adcps. *J. Atmos. Oceanic Technol*, 34 (1):5–20, 2017.

P. Rusello and E. Cowen. Turbulent dissipation estimates from pulse coherent doppler instruments. In *Proceedings. IEEE/OES 10th Current, Waves and Turbulence Measurements (CWTM), Monterey, CA.*, pages 167–172. IEEE, 2011.

T. Rippeth, J. Simpson, E. Williams, and M. Inall. Measurement of the rates of production and dissipation of turbulent kinetic energy in an energetic tidal flow: Red wharf bay revisited. *Journal of Physical Oceanography*, 33(9):1889–1901, 2003.

J. L. Lumley and E. A. Terray. Kinematics of turbulence convected by a random wave field. *Journal of Physical Oceanography*, 13:2000–2007, 1983.

K. Sreenivasan. On the universality of the kolmogorov constant. *Phys. Fluids*, 7(11):2778–2784, 1995.

J. Thomson. Wave breaking dissipation observed with SWIFT drifters. *Journal of Atmospheric and Oceanic Technology*, 29(12):1866–1882, 2012.

E. Williams and J. Simpson. Uncertainties in estimates of reynolds stress and tke production rate using the adcp variance method. *J. Atmos. Ocean. Technol.*, 21(2):347–357, 2004.

J. Kaimal, J. Wyngaard, Y. Izumi, and O. Coté. Spectral characteristics of surface-layer turbulence. *Q. J. R. Meteorol. Soc.*, 98(417):563–589, 1972.

R. Walter, N. Nidzieko, and S. Monismith. Similarity scaling of turbulence spectra and cospectra in a shallow tidal flow. *J. Geophys. Res. Oceans*, 116(C10), 2011.

A. Brand, D. McGinnis, B. Wehrli, and A. West. Intermittent oxygen flux from the interior into the bottom boundary of lakes as observed by eddy correlation. *Limnol. Oceanogr.*, 53(5):1997–2006, 2008.

D. Vachon, Y. Prairie, and J. Cole. The relationship between near-surface turbulence and gas transfer velocity in freshwater systems and its implications for floating chamber measurements of gas exchange. *Limnol. Oceanogr.*, 55(4):1723–1732, 2010.

L. Merckelbach. A model for high-frequency acoustic doppler current profiler backscatter from suspended sediment in strong currents. *Continental Shelf Research*, 26(11):1316–1335, 2006.

D. Codiga and A. Nehra. Foster-lis gridded data products: Updated methods and appended 2010-2011 observations. Technical Report 2012-01, Graduate School of Oceanography, University of Rhode Island, Narragansett, RI, 2012.

C. Balfour, M. Howarth, D. Jones, and T. Doyle. The design and development of an Irise

Sea Passenger-Ferry-Based oceanographic measurement system. *Journal of Atmospheric and Ocean Technology*, 30:1226 – 1239, 2012.

W. Petersen. Ferrybox systems: State-of-the-art in europe and future development. *Journal of Marine Systems*, 140, Part A(0):4 – 12, 2014.

J. Nauw, L. Merckelbach, H. Ridderinkhof, and H. Van Aken. Long-term ferry-based observations of the suspended sediment fluxes through the marsdiep inlet using acoustic doppler current profilers. *Journal of Sea Research*, 87:17–29, 2014.

Xiao-Hua Zhu, Hirohiko Nakamura, Menghong Dong, Ayako Nishina, and Toru Yamashiro. Tidal currents and kuroshio transport variations in the tokara strait estimated from ferryboat adcp data. *Journal of Geophysical Research: Oceans*, 122(3):2120–2142, 2017.

Z. Liu, H. Nakamura, X. Zhu, A. Nishina, and M. Dong. Tidal and residual currents across the northern ryukyu island chain observed by ferryboat adcp. *Journal of Geophysical Research: Oceans*, 122(9):7198–7217, 2017.

D. Codiga. Foster-lis gridded data products: Observed current profiles and near-surface water properties from ferry-based oceanographic sampling in eastern long island sound. Technical Report 2007-01, Graduate School of Oceanography, University of Rhode Island, Narragansett, RI, 2007.

D. Sutherland, P. MacCready, N. Banas, and L. Smedstad. A Model Study of the Salish Sea Estuarine Circulation. *Journal of Physical Oceanography*, 41(6):1125–1143, 2011.

D. Codiga. Unified tidal analysis and prediction using the utide matlab functions. Technical Report 2011-01, Graduate School of Oceanography, University of Rhode Island, Narragansett, RI, 2011.

C. Alessi, R. Beardsley, R. Limeburner, L. Rosenfeld, S. Lentz, U. Send, C. Winant, J. Allen, G. Halliwell, W. Brown, et al. Code-2: moored array and large-scale data report. Technical report, Woods Hole Oceanographic Institution, 1985.

M. Adaramola and P. Krogstad. Experimental investigation of wake effects on wind turbine performance. *Renewable Energy*, 36(8):2078–2086, 2011.

L. Myers and S. Bahaj. An experimental investigation simulating flow effects in first generation marine current energy converter arrays. *Renewable Energy*, 37(1):28 – 36, 2012.

V. Neary, B. Gunawan, C. Hill, and L. Chamorro. Near and far field flow disturbances induced by model hydrokinetic turbine: ADV and ADP comparison. *Renewable Energy*, 60:1–6, 2013.

M. De Dominicis, R. Murray, and J. Wolf. Multi-scale ocean response to a large tidal stream turbine array. *Renewable Energy*, 114:1160–1179, 2017.

A. Brown, S. Neill, and M. Lewis. Tidal energy extraction in three-dimensional ocean models. *Renewable Energy*, 114:244–257, 2017.

S. Kang, X. Yang, and F. Sotiropoulos. On the onset of wake meandering for an axial flow turbine in a turbulent open channel flow. *Journal of Fluid Mechanics*, 744:376–403, 2014.

L. Chamorro, C. Hill, V. Neary, B. Gunawan, R. Arndt, and F. Sotiropoulos. Effects of energetic coherent motions on the power and wake of an axial-flow turbine. *Physics of Fluids (1994-present)*, 27(5):055104, 2015.

L. Myers and A. Bahaj. Experimental analysis of the flow field around horizontal axis tidal turbines by use of scale mesh disk rotor simulators. *Ocean Engineering*, 37(2):218–227, 2010.

S. Kang, I. Borazjani, J. Colby, and F. Sotiropoulos. Numerical simulation of 3d flow past a real-life marine hydrokinetic turbine. *Advances in Water Resources*, 39:33–43, 2012.

M. Boudreau and G. Dumas. Comparison of the wake recovery of the axial-flow and cross-flow turbine concepts. *Journal of Wind Engineering and Industrial Aerodynamics*, 165: 137–152, 2017.

S. Chawdhary, C. Hill, X. Yang, M. Guala, D. Corren, J. Colby, and F. Sotiropoulos. Wake characteristics of a triframe of axial-flow hydrokinetic turbines. *Renewable Energy*, 109: 332–345, 2017.

L. Myers and A. Bahaj. Wake studies of a 1/30th scale horizontal axis marine current turbine. *Ocean Engineering*, 34(5):758–762, 2007.

L. Chamorro, D. Troolin, S. Lee, R. Arndt, and F. Sotiropoulos. Three-dimensional flow visualization in the wake of a miniature axial-flow hydrokinetic turbine. *Experiments in Fluids*, 54(2):1–12, 2013b.

P. Bachant and M. Wosnik. Characterising the near-wake of a cross-flow turbine. *Journal of Turbulence*, 16(4):392–410, 2015.

Y. Chen, B. Lin, J. Lin, and S. Wang. Experimental study of wake structure behind a horizontal axis tidal stream turbine. *Applied Energy*, 196:82–96, 2017.

A.H. Day, A. Babarit, A. Fontaine, Y.-P. He, M. Kraskowski, M. Murai, I. Penesis, F. Salvatore, and H.-K. Shin. Hydrodynamic modelling of marine renewable energy devices: A state of the art review. *Ocean Engineering*, 108:46 – 69, 2015.

B. Polagye, R. Cavagnaro, A. Niblick, T. Hall, J. Thomson, and A. Aliseda. Cross-flow turbine performance and wake characterization. In *Proceedings of the 1st Marine Energy Technology Symposium (METS13), Washington, DC*, 2013.

W. Batten, A. Bahaj, A. Molland, and J. Chaplin. The prediction of the hydrodynamic performance of marine current turbines. *Renewable Energy*, 33(5):1085–1096, 2008.

D. Forbush, B. Polagye, J. Thomson, L. Kilcher, J. Donegan, and J. McEntee. Performance characterization of a cross-flow hydrokinetic turbine in sheared inflow. *International Journal of Marine Energy*, 16:150–161, 2016.

M. Guerra and J. Thomson. Turbulence measurements from 5-beam acoustic doppler current profilers. *Journal of Atmospheric and Oceanic Technology*, 2017.

S. Neill, J. Jordan, and S. Couch. Impact of tidal energy converter (tec) arrays on the dynamics of headland sand banks. *Renewable Energy*, 37(1):387–397, 2012.